THE BUILD-UP

OF

MASSIVE GALAXIES

THE BUILD-UP

OF

MASSIVE GALAXIES

PROEFSCHRIFT

door

Maria Catharina Damen
geboren te Delft
in 1980

Promotiecommissie

Promotores:	Prof. dr. M. Franx
	Prof. dr. P.G. van Dokkum (Yale University, USA)
Co-Promotor:	Dr. I. Labbé (Carnegie Observatories, USA)
Overige leden:	Prof. dr. P. Barthel (Rijksuniversiteit Groningen)
	Prof. dr. H.J.A. Röttgering
	Dr. J. Brinchmann
	Dr. P.P. van der Werf

Voor Bas.

TABLE OF CONTENTS

1

INTRODUCTION

1.1 Extragalactic Astronomy

THE Milky Way is one of the most impressive features of the night sky. The band of stars that we observe is in fact a projection of a galaxy that contains hundreds of billions of stars, including the sun. The stars are mostly confined to a thin disk, in which they form a multitude of spiral arms that are entwined with dust lanes. Such stellar systems are wide-spread in the universe, but this has only been known since the beginning of the last century. In the 1920's, Edwin Hubble discovered that some of the nebular structures he observed, were actually galaxies containing billions of stars. He discerned two classes: the spiral galaxies, which resembled the Milky Way and a second class of objects, less conspicuous in appearance, the elliptical galaxies (Fig. 1.1).

Based on his observations, Hubble constructed a galaxy classification scheme that is still in use today (Hubble, 1936). The basis for the classification is morphology, but this is not the only difference between the two main classes. Spiral and elliptical galaxies also differ in physical properties such as color (indicating a different stellar content), internal reddening (depending on the dust content), amount of interstellar gas, and star formation rate. Spiral galaxies are actively forming new stars, which results in a blue color. Elliptical galaxies consist mainly of old stars and are red. The stars in elliptical galaxies seem to be isotropically distributed. However, a closer look reveals a complicated sub-structure that can contain boxy forms and counter-rotating cores, indicating that eliptical galaxies are the product of complex evolutionary trajectories.

This dichotomy of the local galaxy population manifests itself also in mass. Star formation occurs primarily in blue spiral galaxies with low stellar mass ($M_* < 3 \cdot 10^{10} M_\odot$), whereas the more massive galaxies typically are red elliptical galaxies with old stellar populations. Both types of galaxy fill a
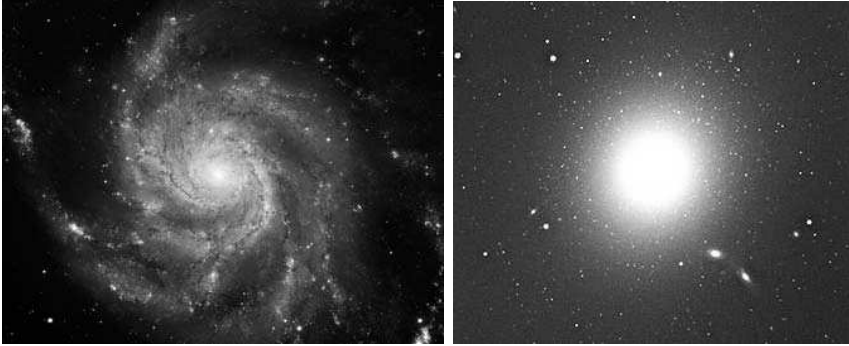
Figure 1.1 – The majority of the local galaxy population belongs to two classes: spiral and elliptical galaxies. *Left* - M101, an example of a spiral galaxy. The detailed spiral structure and blue color are the main characteristics of this class. Our Milky Way has a similar shape. *Right* - M87, a typical elliptical galaxy. The characteristic red color of elliptical galaxies indicates an old stellar population. *Images by the Anglo-Australian Observatory and Hubble Space Telescope.*

specific locus in a color-mass diagram (Fig. 1.2). The old massive ellipticals are concentrated along a red sequence, whereas the blue star forming galaxies form a blue cloud (Kauffmann et al. 2003; Blanton et al. 2005). These striking features of the nearby universe prompt some big questions. What is the origin of this color bimodality? What created the morphologies of local galaxies? And more general: How and when did galaxies form? When did they assemble their mass? To be able to answer such questions, one needs a picture of the galaxies at each stage of their evolution. Such pictures can be taken thanks to one particular characteristic of our universe: the finite speed of light.

1.2   The Distant Universe

To discover the conditions for galaxy formation and learn how galaxies evolved, we have to observe the distant universe. Due to the finite speed of light, an observation of a distant object is inevitably also a view into the past. In recent years our ability to find such distant (and thus dim) objects have improved immensely thanks to technological progress. Large telescopes and sensitive instruments have opened up a window to the distant universe, which means that today we can observe galaxies which emitted their light 13 billion years ago. In this way, we can study the evolution of galaxies throughout the past history of the universe, by simply registering and analyzing the galaxies found at different distance intervals.

Such look-back studies would not be possible if the universe were not expanding[1]. Practically all information on the distant universe is based on

---

[1]One of the great discoveries of the 20th century is that the universe is expanding;

the analysis of electromagnetic radiation reaching us from faraway objects. As the light travels from its source to us, it feels the effect of the expanding universe and its wavelength is stretched (redshifted). This stretching is larger the longer the photon needs to travel and the amount of stretching is therefore an accurate measurement of the distance (redshift) to the light-emitting source. Helped by the finite speed of light and the expansion of the universe, astronomers can carry out look-back studies to assess empirically when and how galaxies formed.

The distant universe became a prominent field of astronomical research during the final decade of the twentieth century. At that time the Lyman break technique in combination with the new generation of 8- to 10-m telescopes made it possible to identify significant samples of high-redshift objects. Lyman Break Galaxies (LBGs) are color-selected, luminous, star forming galaxies that emitted their light more than 10 billion years ago, e.g., at a redshift $z > 2$. Since then, the bright ultraviolet (UV) radiation that is characteristic for young stars has been redshifted into the optical regime, making it available to large optical telescopes on earth. The galaxies are observed through carefully chosen filters in the UV, blue, and red spectral regions. The signature of an LBG is that its image should be bright in the two longer wavebands, but should not be present in the UV waveband (Steidel et al. 1996; 1998). The Lyman break technique has proven to be very successful and has identified hundreds of high-redshift galaxies. However, since it only targets the starforming galaxies, it does not give a complete census of the galaxy population at those redshifts.

When a star forming galaxy has exhausted its gas reservoir, it fades and becomes redder. The subsequent evolution is simply an aging of the existing stars, called passive evolution. Because young hot stars are absent in such systems, passively evolving galaxies show only little rest-frame UV radiation and are more prominent at longer wavelengths. As a result, these galaxies are not present in LBG-surveys. However, with the arrival of powerful (near-) infrared (NIR) detectors and ensuing NIR surveys, they were readily found. Samples of distant galaxies with red colors generally include both passively evolving objects and dust-reddened star-forming systems (Franx et al. 2003; van Dokkum et al. 2004; Förster-Schreiber et al. 2004; Labbé et al. 2005). In the case of the latter, the young and hot stars heat the surrounding dust, which re-processes the light at IR wavelengths. NIR surveys uncovered a significant population of massive high-redshift galaxies that were no longer forming stars. These galaxies were already old at z $\sim$ 2, which means they must have formed the bulk of their stellar populations at even higher redshifts (Cimatti et al. 2002; Moustakas et al. 2004; Papovich et al. 2005; Treu et al. 2005).

With the wealth of NIR data currently available, it has become clear that

---

the galaxies recede from each other, and from us. This is Hubble's second fundamental contribution to cosmology)
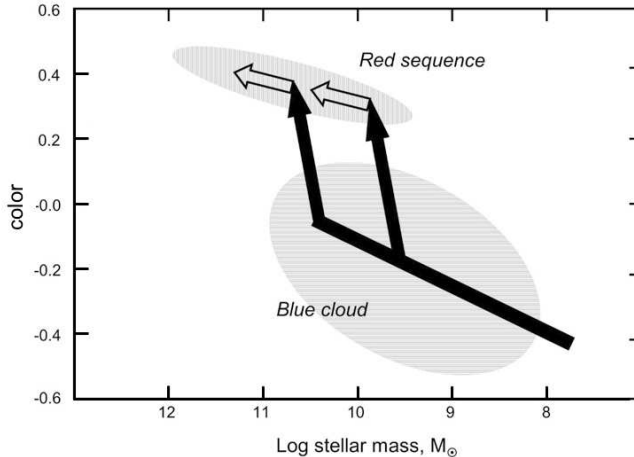
Figure 1.2 – The bimodality in the local galaxy population. Red galaxies form a tight sequence at the top of the diagram. They are typically more massive than blue galaxies, which loosely shape a blue cloud below. The blue galaxies can migrate to the red sequence through mergers in a way that is indicated by the arrows. Blue galaxies first acquire mass through star formation. The nearly vertical lines represent a merger event, during which star formation is quenched and the galaxy becomes red. Once a galaxy arrives on the red sequence it may still gain mass through a series of gas-poor "dry mergers" (*white arrows*). *Figure adapted from Faber et al. 2007.*

the red sequence we observe in the local universe was already in place at $z = 1$ (Bell et al. 2004; De Lucia et al. 2007) and probably even earlier than that (Kriek et al. 2008; Williams et al. 2009; Brammer et al. 2009). We know that since $z = 1$, the amount of stellar mass in the red sequence has approximately doubled (Bell et al. 2004; Faber et al. 2007), which cannot be explained by their low star formation rates (SFR). On the other hand, the amount of mass in the blue cloud stays constant over the same time interval, although these systems are actively forming stars. Somehow, blue galaxies seem to have traveled up to the red sequence, quenching their star formation on the way. The details of this mechanism are still unclear. Mergers of galaxies offer a possible explanation (see Fig. 1.2). The coalescence of two galaxies can result in remnants that are reddened through the loss of gas in the process and the subsequent slowing down of the star formation. Other processes can be repsonsible too, as long as they manage to shut down the star formation.

The SFR as a function of time and mass is clearly one of the key statistics that describes the evolution of the galaxy population. It is important to know when galaxies started to form stars and at what time and under what circumstances star formation was quenched again. In the last decade,
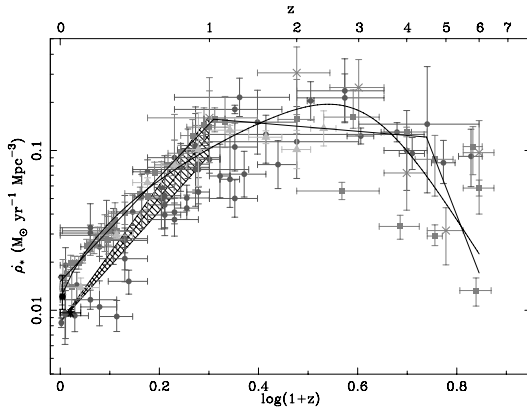
Figure 1.3 − Evolution of the star formation rate density with redshift. This diagram is a compilation of different star formation rate measurements indicated by different symbols. Solid lines represent parametric fits to the data. The cosmic star formation rate reaches a peak between redshifts $2 < z < 4$. It steeply declines at $z < 1$. *Figure taken from Hopkins et al. (2004).*

the advent of deep and/or wide galaxy surveys carried out at many different wavelengths has revolutionized our understanding in this aspect. One example of the achievements is the so-called Madau-diagram, which shows the evolution of the SFR density of the universe as a function of look-back time (Lilly 1996; Madau 1998). From inventories of the stellar content of the local universe (Cole et al. 2001; Bell et al. 2003) and surveys of star formation over its entire comic universe (e.g., Hopkins et al. 2004), it has become clear that the universe experienced a significant decrease (factor $\sim$10) in the rate at which new stars were created. Star formation was much more rapid in the past, reaching a gentle peak at $z \sim 2 - 4$ and falling off towards higher redshifts. Again, a number of physical processes may contribute to this decline, e.g., a declining rate of major galaxy mergers, a drop in the rate of minor tidal interactions, or the progressive consumption of gas. Yet, many empirical aspects of this declining cosmic SFR are still unclear.

The extensive results from observations of galaxies at high redshift might suggest that the formation and evolution of galaxies is quite well understood today. We are able to observe galaxies out to $z \sim 7$ (Bouwens et al. 2010) and therefore possess data of nearly all epochs of cosmic evolution. This seems to imply that we can study the evolution of galaxies directly. However, this is true only to a certain degree. Although we now have found a large number of galaxies at nearly every redshift, the relation between galaxies at different redshifts is not easily understood. We cannot suppose that galaxies seen at different redshifts represent various subsequent stages of evolution of the same kind of galaxy. The main reason for this difficulty is that different selection criteria need to be applied to find galaxies at different redshifts. Thus, it is

difficult to trace the individual galaxy populations as they evolve into each other at different redshifts. This is the reason why our understanding of galaxy evolution is only possible within the framework of models, with the help of which the different observational results can be interpreted.

1.3   Galaxy Design

One of the most important developments in recent years is the establishment of a standard model of cosmology. In this model, the universe has evolved from an extremely dense and hot state, the Big Bang, 13.7 Gyr ago, expanding and cooling ever since. In the beginning, it consisted of an almost homogeneous plasma without heavy chemical elements and with only very tiny fluctuations in the density profile. It was very different from today's structured universe, which contains galaxies, stars, planets, and a multitude of chemical elements, including heavy elements which are the main constituents of our planet and of ourselves.

Even today, echoes of the Big Bang can be observed, in the form of cosmic microwave background (CMB) radiation. Accurate observations of this background radiation, emitted some 380,000 years after the Big Bang, have made an important contribution to what we know today about the composition of the Universe. All structure in the universe has evolved out of primordial density fluctuations. The seeds for structure formation must have already been present in the early phases of cosmic evolution and are in fact detected in the CMB. The technical progress of the last two decades has made it possible to directly observe this interesting cosmic transition period and to build a model that couples the homogeneous soup of the young universe to the rich structure we observe today.

1.3.1   A Standard Model

The observational results which have been accumulated during the past years provide important details and valuable constraints on the formation of galaxies. This information has been combined into a standard model. Astronomers believe that galaxies are formed by the accumulation of baryonic matter in halos of dark matter. The nature of dark matter (DM) is one of the biggest riddles of the universe. It is an invisible but omnipresent form of matter that fills 23% of the universe (which is almost 5 times as much as the total amount of visible matter).

The formation and evolution of the DM halos can be predicted by means of numerical simulations (Springel et al. 2005). The DM simulations provide quantitative predictions for various parameters of the DM distribution as a function of time and redshift. More difficult is the prediction of the evolution of the baryonic matter, e.g., the stuff galaxies are made of. In the early evolutionary stages, the gas density simply follows the dark matter

distribution. Eventually, the gas becomes heated by compression and by the radiation of the first stars. From this point the theoretical predictions of the behavior of the gas become less certain. Feedback effects from star formation can strongly modify the baryonic matter distribution by ejecting gas from the affected halos, or even from neighboring low-mass halos. Moreover, the radiation field of the first stars modifies the conditions for star formation in the surrounding gas.

During the past years progress has been made in the theoretical understanding of these processes, and there are major ongoing efforts to further improve the theory. However, the present hydro-dynamical models do not yet include the full physics of the complex process of star-formation.

1.3.2   Semi-Analytic Models

Semi-analytic models (SAMs) were developed to introduce baryons in the DM simulations using prescriptive methods for star formation and feedback. The idea is to design simple parametrized models based either on observations or on more detailed simulations of individual systems and to implement these recipes in the structure formation framework provided by a dark matter simulation. This provides a powerful tool for studying the formation and evolution of the galaxy population. It is not resource-intensive and allows the treatment of large volumes and the exploration of a wide range of input parameters. In the most recent versions, elaborate physically-based models for feedback processes (Croton et al. 2006, Bower et al. 2006), galactic winds (Bertone et al. 2007), and gas stripping in clusters (Font et al. 2008) are being considered.

Simulations of the formation of stars and galaxies in dark halos using SAMs do give plausible results on the structure of the resulting stellar systems (Mo & White 1998). But, because of the approximations and the large number of free parameters, it is difficult to estimate the accuracy of the predictions based on the semi-analytic procedures. Comparing them to observational data can provide useful constraints.

1.4   Outlook

In the history of astronomy, scientific progress can in many cases be directly traced to new and powerful instrumentation. There is no doubt that future astronomical instruments will have a decisive impact on the field of galaxy formation and evolution. Most important for the progress in the field of high-redshift galaxies have been the observations of 8-10 m telescopes (GEMINI, Keck), combined with those from space (Hubble and Spitzer space telescopes). Many of the yet unsolved questions require the light collecting power and the angular resolution of even larger instruments. Coming up are some extraordinary observing facilities that will scan the universe when

galaxies where only just emerging: the Giant Magellan Telescope (GMT; 24.5 m), the Thirty Meter Telescope (TMT; 30m), and the European Extremely Large Telescope (E-ELT; 42 m). An ambitious project at radio wavelengths is the Square Kilometre Array (SKA). It will be an array telescope with a collecting area of 10^6 m^2 operating in the wavelength range from 3 cm to 40 m. However, among all new instrumentation projects, the most promising tool for making significant progress in this field is undoubtedly the James Webb Space Telescope (JWST), a 6.5 m IR telescope (wavelengths ranging from 0.6-28μm) that will be launched into space (currently scheduled in 2014).

The programs carried out at those and other near-future facilities will aim at extending the available data base of high-redshift objects by means of new large surveys. The objective of these projects is to improve our knowledge by generating statistically more significant samples of galaxies of different types. One example is the recently started NEWFIRM medium band survey. Using a set of six medium-band NIR filters, the NEWFIRM survey obtains information and redshifts of IR-bright galaxies in the redshift range $1.5 < z < 3.5$. This survey is expected to provide for the first time a large sample of red high-redshift galaxies with accurate photometric redshifts (van Dokkum et al. 2009).

We are very close to observing luminous galaxies up to the distance at which they were formed for the first time. These are exciting times for observational cosmologists, as the first galaxies are most definitely within reach.

1.5   Thesis Summary

In light of the uncertainties that still exist in current models, observational constraints are required to further develop our understanding of what regulates star formation in massive galaxies. In particular, look-back studies to assess empirically when and how the red sequence emerged are crucial, and require sizeable samples of galaxies of known redshift, stellar mass, SFR, and morphology at epochs when massive galaxies are forming. In this thesis a new survey is presented that uses a combination of UV, optical and IR data to construct a sample of galaxies out to $z \sim 2$. The star formation history and consequent mass build-up of this sample is studied and ultimately compared to model predictions. The main results are summarized below.

In **Chapter 2** we present Spitzer's IRAC and MUSYC Public Legacy of the E-CDFS (SIMPLE), which is mainly based on observations from the Spitzer Space Telescope of one of the most popular fields in observational cosmology: the Extended Chandra Deep Field South (E-CDFS). Our data complement the set of data accumulated by the Multiwavelength Survey by Yale and Chile (MUSYC) which ranges from the near-UV to the near-IR. We provide a detailed description of the data reduction and the resulting catalog.

The catalog of the SIMPLE survey is a flux-limited sample of galaxies. This has to be taken into account when analyzing the data, since it introduces a bias. Luminosity-selected samples do not sample the same absolute magnitudes at each redshift, as they contain brighter galaxies toward higher redshifts. Such selection effects can severely affect results and in **Chapter 3**, we investigate how. We compare the properties of a rest-frame UV-, a rest-frame optical, and a mass-selected sample. We show that the most passive, compact galaxies typically have the highest optical M/L values and the lowest rest-frame UV luminosities. Applying a selection by luminosity will therefore affect known relations between size, mass, and specific star formation rate (sSFR). Sizes and sSFRs in luminosity-selected samples will be on average higher than in mass-selected samples, although an optically selected sample does recover the size-mass- and sSFR-mass-relation of a mass-selected sample at the high-mass end.

Chapter 4 describes the redshift evolution of the stellar mass assembly for a subsample of the SIMPLE survey. We characterize the stellar mass assembly by the specific star formation rate (SFR per unit mass). This is a useful quantity since it allows us to make a distinction between passively evolving and actively starforming galaxies. We find that at all redshifts the galaxies with higher masses have substantially lower specific star formation rates than lower mass galaxies. The average specific star formation rates increase with redshift, and the rate of incline is similar for all galaxies; it does not seem to be a strong function of galaxy mass. Using a subsample of galaxies with masses $M_* > 10^{11} M_\odot$, we measured the fraction of galaxies whose star formation is quenched. The fraction of quiescent galaxies decreases with redshift out to $z \sim 1.8$. We find that, at that redshift, $\sim$30% of the massive galaxies are quiescent.

The evolution of the global SFR can be used as robust constraint on various simulations and SAMs of galaxy evolution. In **Chapter 5** we compare the build-up of massive galaxies as found through our own observations with SAM predictions. We also include deeper data from the FIREWORKS survey to extend the comparison to higher redshifts ($z \sim 3$). Both the model and the observations show a growth rate through star formation that increases with redshift. However, we find that for all masses, the inferred observed growth rates increase more rapidly with redshift than the model predictions. We discuss several possible observation-related causes for this discrepancy and find that none of them can solve it completely. The models need to be adapted to produce the steep increase in growth that is observed between $z = 0$ and $z = 1$.

References

Bell, E. F. 2003, ApJ, 586, 794

Bell, E. F., et al. 2004, ApJ, 600, 752

Bertone, S., De Lucia, G., Thomas, P. A. 2007, MNRAS, 379, 1143

Blanton, et al. 2005, ApJ, 629, 143

Brammer, G. B, et al. 2009, ApJ, 706, 173

Bower, R., 2006, MNRAS, 370, 645

Bouwens, R., et al. 2010, ApJ, 709, 133

Cimatti, A., et al. 2002, A&A, 392, 395

Cimatti, A., et al. 2004, Nature, 430, 184

Cole et al. 2001, MNRAS, 316, 255

Croton, D., et al. 2006, MNRAS, 365, 11

Daddi, E., Cimatti, A., Pozzetti, L., Hoekstra, H., Röttgering, H. J. A., Renzini, A., Zamorani, G., Mannucci, F. 2000, A&A, 361, 535

Daddi, E., et al. 2005, ApJ, 626, 680

De Lucia, G., et al. 2007, MNRAS, 374, 809

Faber, S. M., et al. 2007, ApJ, 655, 265

Font, J., et al. 2008, MNRAS, 389, 1619

Förster Schreiber, N. F. S., van Dokkum, P. G., Franx, M., Labbé, I., Rudnick, G. 2004, ApJ, 616, 14

Franx, M. et al. 2003, ApJ, 587, 79

Hopkins, A. M. 2004, ApJ, 615, 209

Hubble, E. P. 1936, The Realm of the Nebulae. New Haven: Yale University Press.

Kauffmann, et al. 2003, MNRAS, 341, 54

Kriek, M., et al. 2008, ApJ, 677, 219

Labbé, I. et al. 2005, ApJ, 624, 81

Labbé, I., Bouwens, R., Illingworth, G, D., Franx, M. 2006, ApJ, 649, 67

Lilly, S. J., Le Févre, O., Hammer, F., & Crampton, D. 1996, ApJ, 460, L1

Madau, P., Pozzetti, L., Dickinson, M. 1998, ApJ, 498, 106

Mo, H. J. & White., S. 1998, MNRAS, 295, 319

Moustakas, L., et al. 2004, 600, 131

Papovich, C., Dickinson, M., Giavalisco, M., Conselice, C. J., Ferguson, H. C. 2005, ApJ, 631, 101

Springel, V. 2005, Nature, 435, 629

Steidel, C. C., Giavalisco, M., Dickinson, M., Adelberger, K, L. 1996, AJ, 112, 352

Steidel, C. C., Adelberger, K. L., Giavalisco, M., Dickinson, M., Pettini, M. 1999, ApJ, 519, 1

Treu, T., et al. 2005, ApJ, 633, 174

van Dokkum, P. G., et al. 2004 ApJ, 611, 703

van Dokkum, P. G., et al. 2009, PASP, 121, 2

Williams, R. J., Quadri, R. F., Franx, M., van Dokkum, P. G., Labbé, I. 2009, ApJ, 691, 1879

2

THE SIMPLE SURVEY

We present the *Spitzer* IRAC/MUSYC Public Legacy Survey in the Extended CDF-South (SIMPLE), which consists of deep IRAC observations covering the $\sim$1,600 arcmin^2 area surrounding GOODS-S. The limiting magnitudes of the SIMPLE IRAC mosaics typically are 23.8, 23.6, 21.9, and 21.7, at 3.6 μm, 4.5 μm, 5.8 μm, and 8.0 μm, respectively (5σ total point source magnitudes in AB). The SIMPLE IRAC images are combined with the $10'$ $\times$ $15'$ GOODS IRAC mosaics in the center. We give detailed descriptions of the observations, data reduction and properties of the final images, as well as the detection and photometry methods used to build a catalog. Using published optical and near-infrared data from the Multiwavelength Survey by Yale-Chile (MUSYC), we construct an IRAC-selected catalog, containing photometry in $UBVRIz'JHK$, [3.6 μm], [4.5 μm], [5.8 μm], and [8.0 μm]. The catalog contains 43,782 sources with S/N > 5 at 3.6 μm, 19,993 of which have 13-band photometry. We compare this catalog to the publicly available MUSYC and FIREWORKS catalogs and discuss the differences.

Maaike Damen, Ivo Labbé, Pieter G. van Dokkum, Marijn Franx, Ned Taylor, Niel Brandt, Mark Dickinson, Eric Gawiser, Garth. D. Illingworth, Mariska Kriek, Danilo Marchesini, Adam Muzzin, Casey Papovich, Hans-Walter Rix

2.1   Introduction

OUR understanding of galaxy formation and evolution has dramatically increased through the rise of large and deep galaxy surveys that have opened up the high-redshift universe for research. The best studied high-redshift galaxies are arguably the Lyman Break Galaxies (LBGs) that can be identified by their rest-frame UV colors (Steidel et al. 1996; 1999). Although much has been learned from studying their properties, LBGs are not representative for all high-redshift galaxy populations.

Since they are based on selection in the rest-frame UV, optical surveys of high-redshift galaxies are heavily affected by dust obscuration and are not sensitive to old stellar populations. The rest-frame optical is less influenced by the contribution from young stars and dust and provides a more reliable means of tracing the bulk of the stellar mass at high redshift. For instance, near-infrared observations have uncovered a significant population of massive, red galaxies, particularly at high redshift (Elston, Rieke & Rieke 1988; Spinrad et al. 1997; Barger et al. 1999; Daddi et al. 2000; Franx et al. 2003; Labbé et al. 2003; Cimatti et al. 2004; van Dokkum et al. 2006).

With the arrival of the *Spitzer Space Telescope* and its Infrared Array Camera (IRAC; Fazio et al. 2004), constructing large surveys to study high-redshift galaxies has become even more attainable, since the IRAC wavelengths provide coverage of the rest-frame optical bands out to higher redshifts. Using deep IRAC observations at 4.5 μm it is possible to trace the rest-frame I-band out to a redshift $z \sim 4$.

The massive, red galaxies found at high redshift are important test-beds for models of galaxy formation and evolution. To be able to place constraints on the models we need a clear picture of the evolution and star formation history of these massive galaxies. This requires large, statistically powerful samples, or in other words, surveys that extend over a great area and depth.

It is also critical to do these observations in areas that already have been observed at many wavelengths and ideally in areas that are accessible to future telescopes such as ALMA. The $30' \times 30'$ Extended Chandra Deep Field South (E-CDFS) is perfect in this sense as it is one of the most extensively observed fields available. There is a large set of ground-based data providing $UBVRIz'JHK$ imaging (MUSYC (Gawiser et al. 2006, Quadri et al. 2007, Taylor et al. 2009), COMBO-17 (Wolf et al. 2004), LCIRS, (McCarthy et al. 2001)), radio coverage (Miller et al. 2008), and spectroscopy (e.g., GOODS (VIMOS: Popesso et al. 2009, FORS2: Szokoly et al. 2004, Vanzella et al. 2008), MUSYC (Treister et al. 2009), K20 (Cimatti et al. 2002), VVDS (le Fèvre et al. 2004)). The area has been targeted intensely from space too. There is HST ACS imaging from GEMS (Rix et al. 2004), observations from CHANDRA (Lehmer et al. 2005, Luo et al. 2008), XMM (PI: J. Bergeron), GALEX (Martin et al. 2005), and ultra deep multiwavelength coverage from the Great Observatories Origins Deep Survey (GOODS, Dick-

inson et al. 2001, 2003) in the central $10' \times 15'$. The rich multiwavelength coverage includes also deep 24 μm observations from the Far-Infrared Deep Extragalactic Survey (FIDEL).

In this context we initiated *Spitzer*'s IRAC + MUSYC Public Legacy of the E-CDFS (SIMPLE), which aims to provide deep, public IRAC imaging of a 1,600 arcmin^2 area on the sky. In this chapter we present the full IRAC data set, with an IRAC-selected multicolor catalog of sources with 13-band optical-to-infrared photometry (covering 0.3-8.0 μm). The optical to near-infrared (NIR) data come from the Multiwavelength Survey by Yale-Chile (MUSYC; Taylor et al. 2009), which are publicly available[1]. We also included the 24 μm data from FIDEL, which reaches a depth of $\sim$40 μJy.

In addition to the study of massive galaxies, the SIMPLE survey can be used to analyze AGN properties. Luminous optically unobscured AGN can be selected based on their IRAC colors (Lacy et al. 2004, Stern et al. 2005). In the case of dust-obscured AGNs, the energy absorbed at optical to X-ray wavelengths is later re-emitted in the mid-IR. AGN should therefore by very bright mid-IR sources. The SIMPLE survey has proved valuable in this context (Cardamone et al. 2008, Treister et al. 2009a, 2009b) and the full photometric dataset in the E-CDFS can provide strong constraints on the redshifts, masses, and stellar populations of the host galaxies. Furthermore, IRAC observations have been useful in investigating the stellar populations of Lyα-emitting galaxies (Lai et al. 2008). Here we focus on the observations, data reduction processes and the construction of the catalog.

This chapter is structured as follows. In Section 2.2 we describe the observations with IRAC. Section 2.3 explains the reduction processes and the combined IRAC mosaics. The ancillary data from the MUSYC and FIDEL surveys that we use are described in Section 2.4. Source detection and photometry are discussed in Section 2.5. In Section 2.6 we examine our photometric redshifts by comparing them to a compilation of spectroscopic redshifts. The catalog parameters are listed and explained in Section 2.7 and Section 2.8 describes the comparison of the SIMPLE catalog with two other catalogs of the (E-)CDFS. Finally, Section 2.9 provides a summary of this chapter.

Throughout this chapter we assume a ΛCDM cosmology with $\Omega_{\mathrm{m}} = 0.3$, $\Omega_{\Lambda} = 0.7$, and $H_0 = 70$ km s^{-1} Mpc^{-1}. All magnitudes are given in the AB photometric system. We denote magnitudes from the four *Spitzer* IRAC channels as [3.6 μm], [4.5 μm], [5.8 μm], and [8.0 μm], respectively. Stellar masses are determined assuming a Kroupa (2001) initial mass function (IMF).

---

[1]http://www.astro.yale.edu/MUSYC

Table 2.1 − limiting depths (total AB magnitude)

program	area	channel	depth (AB mag)	S/N	integration time
GOODS-S	138 arcmin^2	3.6 μm	26.15	3	23 hrs
		4.5 μm	25.66		
		5.8 μm	23.79		
		8.0 μm	23.70		
SIMPLE	1,600 arcmin^2	3.6 μm	23.86	5	0.9-2.5 hrs
		4.5 μm	23.69		
		5.8 μm	21.95		
		8.0 μm	21.84		
S-COSMOS	2 deg^2	3.6 μm	24.0	5	1200 s
		4.5 μm	23.3		
		5.8 μm	21.3		
		8.0 μm	21.0		
SWIRE	60 deg^2	3.6 μm	21.4	10	120-480 s
		4.5 μm	21.4	5	
		5.8 μm	19.8		
		8.0 μm	19.9		

2.2   Observations

The SIMPLE IRAC Legacy survey consists of deep observations with the Infrared Array Camera (IRAC; Fazio et al. 2004) covering the $\sim$1,600 $'^2$ area centered on the GOODS IRAC imaging (Dickinson et al. 2003) of the Chandra Deep Field South (CDFS; Giacconi et al. 2002). The survey is complementary in area and depth to other legacy programs, such as GOODS-IRAC (138 armin^2, 23 hrs (Dickinson et al. 2003)), S-COSMOS (2 deg^2, 1200 s (Sanders et al. 2007)) SWIRE (60 deg^2, 120-480s (Lonsdale et al. 2003)) (see Table 2.1 for more details). The goal of the SIMPLE survey was to map a large area around the CDFS, with an optimum overlap with existing surveys such as GEMS, COMBO-17, and MUSYC. The area of the CDFS appears as a hole in the center of the mosaic. The central coordinates of the field are: $\alpha = 3^h32^m29.^s460, \delta = -27°48'18''.32$, J2000). Figure 2.1 illustrates the field of the main surveys of the E-CDFS: GOODS (IRAC and ACS), GEMS, COMBO-17, MUSYC, and SIMPLE.

The SIMPLE IRAC Legacy program was observed under program number GO 20708 (PI van Dokkum). The complete set of observations consists of 36 series of 6 pointings on a grid of $10' \times 15'$. Each pointing was observed for 30 minutes, which results in a total exposure time of 105 hours. Since the series of observations overlap, the average exposure time per pointing is $\sim$1.5 hours.

The observations were split in two epochs, approximately 6 months apart. The telescope orientation was rotated $\sim$170° between the two epochs and this ensured that the area of the E-CDFS was fully covered in all four IRAC bands. This is illustrated in Fig. 2.2, which shows the exposure coverage of
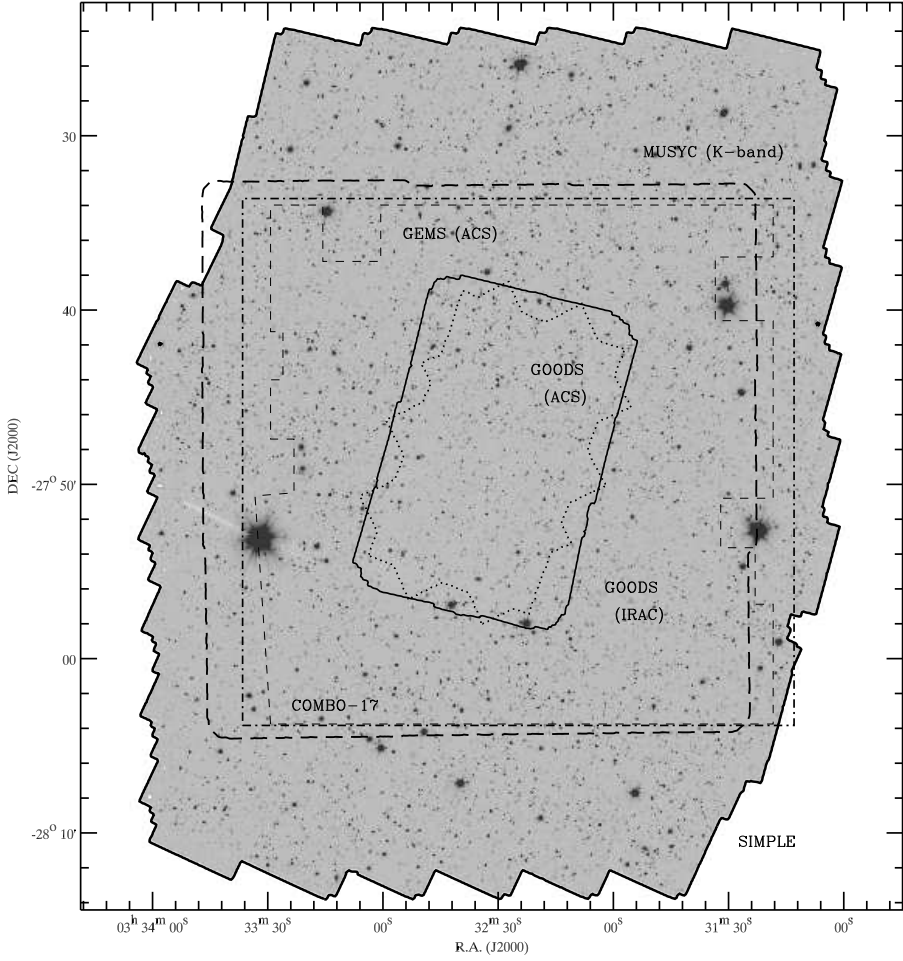
Figure 2.1 − E-CDFS in the combined 3.6 μm + 4.5 μm detection image. The image is normalized by the square root of the weight map, producing a noise-equalized detection image (see Section 2.5.1). The thin dashed lines delineate the GEMS field, COMBO-17 is represented by the dash-dotted lines, the dotted and solid lines indicate the field of view of the GOODS ACS and IRAC observations, respectively, and the long dashed lines indicate the MUSYC field.
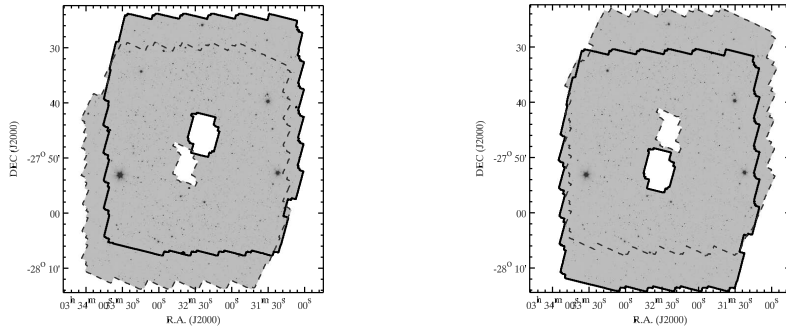
Figure 2.2 – E-CDFS in channel 1 (*left*) and channel 2 (*right*). In both panels the data of the first epoch are indicated by the solid lines and those of the second epoch with dashed lines. Due to the special setup of IRAC, the full area is covered after the two epochs for all channels. Since channels 1 and 3 are observed simultaneously, the lines in the left panel also delineate the field of view of channel 3. The same is true for channel 2 and 4 in the right panel.

<div align="center">

Table 2.2 – Observations

Spitzer program ID	20708
Target name	E-CDFS
RA (J2000)	$3^h32^m29.^s46$
Dec (J2000)	$-27°48'18''.32$
start date ep1	2005-08-19 (week 91)
end date ep1	2005-08-23 (week 91)
start date ep2	2006-02-06 (week 115)
end date ep2	2006-02-11 (week 116)

</div>

channel 1 (3.6 μm; left) and channel 2 (4.5 μm; right). Solid lines indicate the outline of all observations from the first epoch, dashed lines those of the second. IRAC observes in pairs: 3.6 and 5.8 μm simultaneously on one field and 4.5 and 8.0 μm on an adjacent field. Due to this construction and the telescope rotation between the two epochs, the full area was covered by all bands after completion of the observations. A summary of the observations is given in Table 2.2. The raw data and the observational details can be obtained from the *Spitzer* Archive with the Leopard software package[2].

2.3   Data Reduction

The reduction of the IRAC data was carried out using the Basic Calibrated Data (BCD) generated by the *Spitzer* Science Center (SSC) pipeline and a custom-made pipeline that post-processes and mosaicks the BCD frames.

---

[2]http://ssc.spitzer.caltech.edu/propkit/spot/

The reduction includes the following steps:

- SSC pipeline processing

- Artifact correction

- Cosmic ray rejection

- Astrometry

- Image combination and mosaicking

- Flux calibration

- Exposure time and RMS maps

- Flag maps

The starting point for the reduction are the BCD frames produced by SSC pipeline. The epoch 1 observations were processed by BCD pipeline version S12.4.0. The epoch 2 data were processed using pipeline version S13.2.0. The main differences between these two versions are related to pointing refinement, muxstriping and flux conversion. These issues are all addressed separately in our own reduction pipeline, and hence these updates have no effect on the end product. An additional enhancement of S13.2.0 is the introduction of a super sky flat image, based on the first two years of IRAC of flat-field data. This has only a small effect on the data of at most 0.5%. The most significant steps of the SSC IRAC reduction pipeline are dark subtraction, detector linearization, flat-fielding and cosmic ray detection. The data are calibrated in units of MJy/sr. The pipeline also identifies bad pixels, which it flags and writes to a mask image, and constructs initial masks for cosmic rays (called "brmsk").

2.3.1   Post-Processing of the BCD Frames

We post-process the BCD frames to correct for several artifacts caused by highly exposed pixels (primarily bright stars and cosmic rays) and calibrate the astrometry. In this section we briefly describe some of the artifacts and how we try to remove them. More detailed information can be found in the IRAC Data Handbook, Section 4[3]. The subsequent reduction steps are similar, but not identical, to those applied by the GOODS team[4].

We start with discarding the two leading short exposures of each series of observations, which can suffer from the so-called first-frame effect and can

---

[3]http://ssc.spitzer.caltech.edu/irac/dh
[4]http://ssc.spitzer.caltech.edu/legacy/goodshistory.html

not be calibrated correctly[5].

Prior to correction for the artifacts, a median sky image is constructed based on the data taken in each series of observations. This sky image is subtracted from each individual frame to remove both residual structure or gradients in the background caused by bias or flat fielding, and long-term persistence effects.

2.3.1.1   Detector Artifacts

One of the principal artifacts in IRAC data is column-pulldown. When a bright star or cosmic ray reaches a level of $> \sim 35{,}000$ DN in the channel 1 and 2 arrays (3.6 and 4.5 μm), the intensity of the column in which the bright object lies is affected. Since the intensity decreases throughout the column, this effect is called "column pull-down". While column pull-down is slightly different below and above the bright object and has a small slope, the effect is nearly constant in practice. We therefore correct for the effect by 1) locating the columns of $> \sim 35{,}000$ DN pixels 2) masking all bright sources in the frame, 3) calculating the median of the affected columns excluding any sources, and 4) subtracting the median. We favor this simple correction because its implementation is more robust than fitting e.g., a general two-segment slope.

Besides column-pulldown, channels 1 and 2 suffer from an effect known as muxbleed, which appears as a trail of pixels with an enhanced and additive output level. When a bright source is read out, the readout multiplexers do not return to their cold state for some time, resulting in a pattern that trails bright sources on the row. Since columns are read simultaneously in groups of four, the effect repeats every fourth column. The amplitude of the effect decreases with increasing distance to the bright object, but it does not scale with its flux. It is therefore not possible to fit muxbleed by a simple function, and we choose for a very straightforward cosmetic correction. For each offending pixel (> 30 MJy/sr), we generate a list of pixels selecting every fourth pixel next in the row and previous in the row. Then we median filter the pixel list with a filter width of 20 pixels and subtract the result. The data products (see Section 2.3.5) include a map that shows which pixels were muxbleed corrected.

This procedure removes the bulk of the muxbleed signal, but not all of it. However, the effect of a residual muxbleed signal in the final mosaic is reduced because of the rotation of the field between the two epochs. At different times the muxbleed trail affects different pixels relative to the source position.

---

[5]Due to the first frame effect the first frame of a series of observations will have a different bias offset than the rest of the observations in the sequence. Since the first image of each series is observed in "HDR-mode" (a very short exposure time of 0.4 seconds for identification of saturated sources), the second exposure might still suffer from this effect. It is recommended not to include these frames when building a mosaic.

Bright stars, hot pixels, and particle or radiation hits can also generate a muxstripe pattern. Where muxbleed only affects pixels on the same row, the muxstripe pattern may extend over a significant part of the image, albeit to lower levels. Muxstriping appears as an extended jailbar pattern preceding and/or following the bright pixel. It is a fairly subtle effect, usually only slightly visible in individual frames around very bright stars, but it becomes easily visible in deeper combined frames. Muxstriping is caused by the increase of relaxation time of the multiplexer after a bright pixel is read out. It takes ∼10 μsec to clock the next pixel onto an output, whereas the recovery time after the imprint of a bright pixel is of the order of tens of seconds. The muxstripe effect also repeats every fourth column and extends below each source. Each horizontal band of the image between two bright sources, contains the pattern induced by all sources above it and needs to be corrected accordingly.

We remove this effect by applying an offset in the zones surrounding the offending pixels using a program kindly provided by Leonidas Moustakas of the GOODS-team. In brief, this algorithm identifies the bright sources in each frame and produces a model of the corresponding muxstripe pattern, which can then be subtracted.

Figures 2.3 and 2.4 show the treatment of the artifacts just described. In the upper left panel a BCD frame affected by column pull-down, muxbleed, and muxstriping. The right panel shows the corrections, this frame is subtracted from the affected one, which results in the image below, a clean frame.

Finally, bright sources leave positive residuals on subsequent readouts of the array (persistence), although much of the signal subsides after 6-10 frames. We correct for persistence by creating a mask of all highly exposed pixels in a frame and then masking those pixels in the 6 subsequent frames. Any residual contamination through persistence will be diminished by the final combination of all exposures.

After correction for artifacts, the pipeline subtracts a constant background by 1) iteratively thresholding and masking pixels associated with sources and calculating the mode and RMS of the remaining background pixels, 2) subtracting the mode of the image.

2.3.1.2 Cosmic Ray Rejection

For each series of observations, a first pass registered mosaic is created from the post-processed BCD frames. For the construction of this mosaic, the BCD "brmsk"-frames are used as a first guess to mask candidate cosmic rays. The image is median combined, so it should be free of any deviant pixels.

Next, the first pass image is aligned and subtracted from each exposure. To create a cosmic ray detection image, the result is divided by the associated BCD "bunc" image, which contains estimates of the uncertainties in each
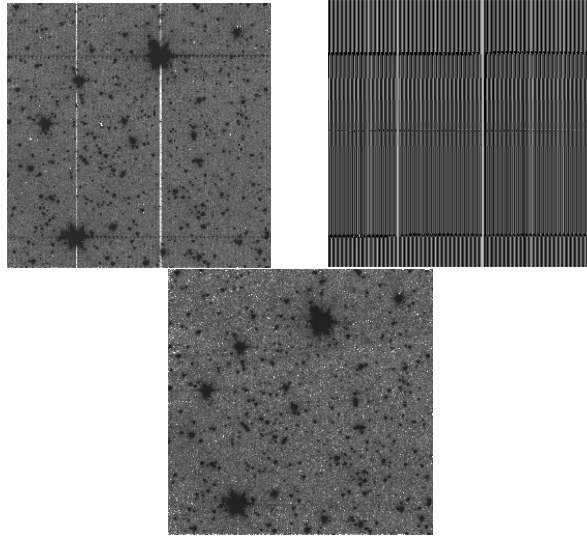
Figure 2.3 − *Upper Left* - Typical BCD frame, suffering from muxbleed (the horizontal black pattern of both sides of the bright sources), column pulldown (vertical white lines), and muxstriping (jailbar pattern that extends below each bright sources over the full width of the frame). *Upper Right* - Correction image that is subtracted from the affected frame. *Below* - Cleaned image, after subtraction of the center frame and removal of cosmic rays. Image from Astronomical Observation Request (AOR) r15564288, channel 1, 96.4 seconds exposure time.

Figure 2.4 − Same as Fig. 2.3, with more pronounced muxstriping pattern. Image from AOR r15564032, channel 1, 96.4 seconds exposure time.

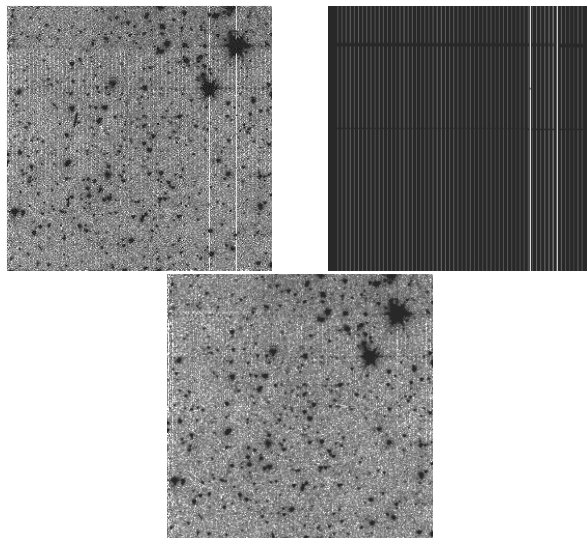pixel based on a noise model[6]. Pixels in this detection image are flagged as cosmic rays if they deviate more than 6 times the median value. Pixels adjacent to deviant pixels are also flagged using a lower threshold (factor 3.5). These flagged pixels are ignored in the analysis of the data.

2.3.1.3 Astrometry

The SIMPLE astrometry is calibrated to a compact source catalog detected in a combined deep BVR-image from MUSYC[7] (Gawiser et al. 2006). The calibration is done on combined frames that were taken sequentially around the same positions. The combined images are cross-matched to the BVR source catalog and the positions of the reference sources are measured.

The astrometric differences between the reference catalog and the SIMPLE pointings are small (up to $\sim 1''$) and can be corrected by applying a simple shift. There is no evidence for rotation, or higher order geometric distortion. We therefore apply a simple offset to the WCS CRVAL1 and CRVAL2 of the BCD frames to refine the pointing. The pointing refinement solutions determined for the 3.6 and 4.5 μm BCDs are applied to the 5.8 and 8.0 μm images, respectively, as there are generally few bright sources at 5.8 and 8.0 μm to derive them independently.

The resulting astrometry accuracy relative to the MUSYC E-CDFS BVR catalog is typically $\sim 0.09''$ (averaged per IRAC channel), with source-to-source 2 σ-clipped RMS of $\sim 0.12''$ in channel 1/2 and $\sim 0.14''$ in channel 3/4. Large scale shears, systematic variations on scales of a few arcminutes, are $0.2''$ or less. Figure 2.5 shows the residual shifts of the [3.6 μm] mosaic with respect to the MUSYC BVR image. The quoted astrometric uncertainties are relative to the MUSYC BVR catalog, but we also verified that the astrometry agrees very well ($\sim 0.1''$ level) with the "wfiRdeep" image (Giavalisco et al. 2004), which is used as a basis for the ACS GOODS astrometry.

2.3.2 Image Combination and Mosaicking

After individual processing, the individual BCD frames are mosaicked onto an astrometric reference grid using the refined astrometric solution in the frame headers.

2.3.2.1 Reference Grid

For the reference grid we adopt the tangent point, pixel size, and orientation of the GOODS IRAC images ($\alpha = 3^h 32^m 29.^s 460, \delta = -27°48'18''.32$,

---

[6]The BCD uncertainty images are the sum of estimates of the read noise, the shot-noise due to the sky and uncertainties in the dark and flat calibration files

[7]The astrometry of the MUSYC BVR detection image is tied to the stellar positions of the USNO-B catalog (Monet et al. 2003)
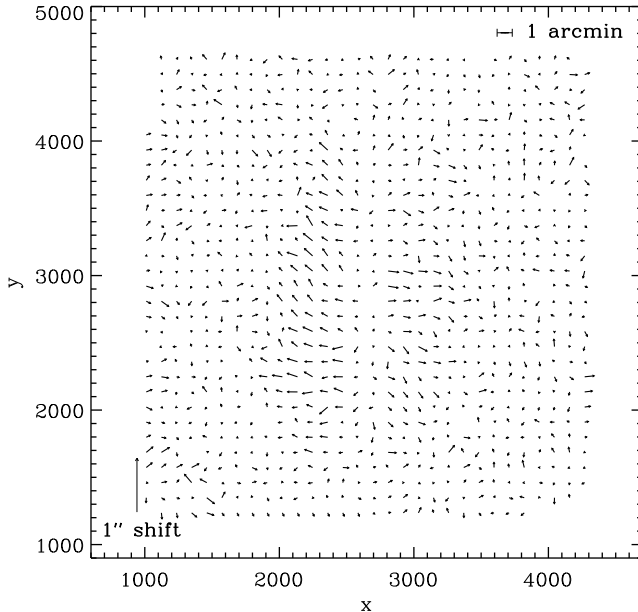
Figure 2.5 − Map of residual shifts of compact sources in the 3.6 μm image with respect to a compact-source catalog detected in the deep BVR-image. Large scale shears, systematic variations on scales of a few arcminutes, are 0.2″ or less.

0.6″/pixel. The pixel axes are aligned with the J2000 celestial axes [8]

Also following GOODS, we put the tangent point (CRVAL1,2) at a half-integer pixel position (CRPIX1,2). This ensures that images with integer pixel scale ratios (e.g., 0.3″, 0.6″, 1.2″) can (in principle) be directly re-binned (block summed or replicated) into pixel alignment with one another. This puts GOODS, SIMPLE, and the Far-Infrared Deep Extragalactic Legacy survey (FIDEL, a deep 24/70 μm survey in the E-CDFS) on the same astrometric grid. The final SIMPLE mosaic extends 38′ × 48′ (3876 × 4868 pixels).

2.3.2.2   Image Combination

For each epoch, the individual post-processed BCD frames are transformed to the reference grid using bicubic interpolation, taking into account geometric distortion of the BCD frame. Cosmic rays and bad pixels are masked and the frames are average combined without additional rejection.

Finally, the separate epoch 1 and epoch 2 mosaics are combined, weighted

---

[8]http://data.spitzer.caltech.edu/popular/goods/20051229_enhanced

channel	λ	flux conversion[a]	zeropoint	FWHM	gaussian convolution
	(μm)	(μJy/(DN/s))	(AB)	($''$)	($''$)
ch1	3.6	3.922	22.416	1.97	0.84
ch2	4.5	4.808	22.195	1.93	0.93
ch3	5.8	20.833	20.603	2.06	0.80
ch4	8.0	7.042	21.781	2.23	–

Table 2.3 – The FWHM of the U-K images is $1.5''$. To convolve those to the PSF of ch4, we use $\sigma = 1.34$

[a]listed as FLUXCONV in the image headers

by their exposure times. By design, the SIMPLE E-CDFS observational strategy maps around the GOODS-S field, which leaves a hole in the combined mosaic. To facilitate the analysis, we add the GOODS-S IRAC data (DR3, mosaic version 0.3 [8], to the center of the SIMPLE mosaic. We shift the GOODS-S IRAC mosaics by $\sim 0.2''$ to bring its astrometry in better agreement with SIMPLE. To ensure a seamless combination between the epoch 1, epoch 2 and GOODS-S images, we subtract an additional background from the images before combination. The background algorithm masks sources and measures the mode of the background in tiles of $1' \times 1'$. The "mode-map" is then smoothed on scales of $3' \times 3'$ and subtracted from the image, resulting in extremely flat images and a zero background level on scales $> 1'$.

2.3.3 Flux Calibration

The SSC data are calibrated using aperture photometry in $12''$ apertures. Since ground-based IR calibrators are too bright to use for IRAC, the actual flux for each channel needs to be predicted using models (Cohen et al. 2003). The resulting calibration factors were determined by Reach et al. (2005) and are listed in the image headers and Table 2.3.

The epoch 1 and epoch 2 science images were scaled to a common zeropoint so that their data units agree. For convenience, we calibrate our images to the GOODS-S IRAC data (in DN s^{-1}). This is done using the original calibration factors from Table 2.3. The relative accuracy of the zeropoint can be estimated by minimizing the count rate differences of bright, non-saturated stars in circular apertures in regions where the images overlap. This indicates that the fluxes agree within $\sim 3\%$.

2.3.4 Additional Data Products

2.3.4.1 Exposure Time and RMS Maps

The exposure time maps are created by multiplying, at each position, the number of BCD frames that were used to form the final image by the in-

tegration time of each frame. The exposure map thus reflects the exposure time in seconds on that position of the sky, not the average exposure time per final output pixel.

The 25%, 50% and 75% percentiles of the final exposure maps (excluding GOODS-S are ~3,100, 5,500 and 9,100 s (0.9, 1.5 and 2.5 hours) for all channels. The corresponding area with at least that exposure time are ~1,200, 800 and 400 arcmin², respectively. In addition, the central GOODS-S mosaic has ~23 hours per pointing over ~138 arcmin².

This release also provides RMS maps. The RMS maps were created by 1) multiplying the final mosaic by the $\sqrt{(t_{exp}/median(t_{exp}))}$ (where t_{exp} is the exposure time map), to create an exposure normalized image; 2) iteratively rejecting pixels deviating $> 4.5\,\sigma$ and their directly neighboring pixels; 3) binning the image by a factor 4×4, and 4) calculating the RMS statistic of the binned pixels in a moving window of 15×15 bins. The result is approximately the local RMS background variation at scales of $2.4''$ at the median exposure time, which does not suffer from correlations due to resampling. We multiply this value by $\sqrt{4}/\sqrt{(t_{exp}/median(t_{exp}))}$ to get the approximate per-pixel RMS variation at the mosaic pixel scale for other exposure times (see e.g., Labbé et al. 2003). This RMS map does not directly reflect the contribution to the uncertainty of source confusion. The variations in the RMS due to instrumental effects are mitigated by the addition of the observed epochs under $180°$ different roll angles.

2.3.4.2   Flags

We provide a flag map, which identifies pixels corrected for muxbleed in channel 1 and channel 2. These corrections are not optimal, and when analyzing the images or constructing source catalogs, it may be useful to find pixels which may have been affected. The flag image is a bit map, i.e., an integer map that represents the sum of bit-wise added values (flag = 1 indicates a muxbleed correction in the first epoch, flag = 2 indicates a correction in the second epoch).

2.3.5   Final Images

The final images of SIMPLE are publicly available[9]. The data release consists of FITS images of all IRAC observations in the E-CDFS. We provide science images, exposure time maps, RMS maps, and a flag map. These images comprise combined mosaics of all data taken (both epochs), including the $10'$ $\times 15'$ GOODS IRAC mosaics in the center. In addition, we provide combined mosaics and exposure maps of the data of the individual epochs (without the GOODS data), which may be useful to study the reliability and/or variability of sources. The units of the science and RMS images are DN s^{-1}, with the

---

[9]http://data.spitzer.caltech.edu/popular/simple

(GOODS) zeropoints as given in Table 2.3. The units of the exposure time maps are seconds. Figures 2.6 and 2.7 show the color composite image of the 3.6 μm and 5.8 μm mosaics.

2.4 Additional Data

2.4.1 The $U - K$ Data

To cover the optical to NIR regime, we use the $UBVRI$ imaging from the COMBO-17 and ESO DPS surveys (Wolf et al. 2004 and Arnouts et al. 2001, respectively) in the re-reduced version of the GaBoDS consortium (Erben et al. 2005; Hildebrandt et al. 2006). We include the $z'JHK$ images from the Multiwavelength Survey by Yale-Chile (MUSYC, Gawiser et al. 2006), which are available on-line[10]. The final UBVRI$z'JHK$ images typically have a seeing of $\sim 1''$. The images we use were PSF-matched to the image with the worst seeing (J-band, 1.5$''$) by Taylor et al. (2009). For more details on the construction of the MUSYC survey and the different data sets, we refer the reader to Taylor et al. (2009).

2.4.2 The MIPS 24 μm Data

The E-CDFS was also observed extensively by the Multi-band Imaging Photometer for *Spitzer* (MIPS) as part of FIDEL (PI M. Dickinson). The survey contains images at 24, 70, and 160 μm. We only consider the 24 μm image, due to its utility as an indicator of star formation and the severe source confusion at larger wavelengths. The FIDEL 24 μm image reaches a 5 σ sensitivity ranging from 40 to 70 μJy, depending on the source position (Magnelli et al.

---

[10]http://www.astro.yale.edu/MUSYC
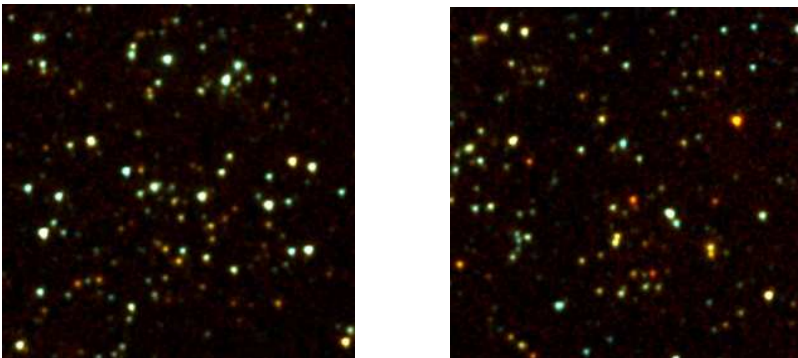
Figure 2.6 − Two example zoomed-in cut-out areas showing details of the full mosaic indicated in Fig. 2.7: (a) left, and (b) right. The images have been enlarged twenty times. The field size is 2.5$'$ × 2.5$'$.

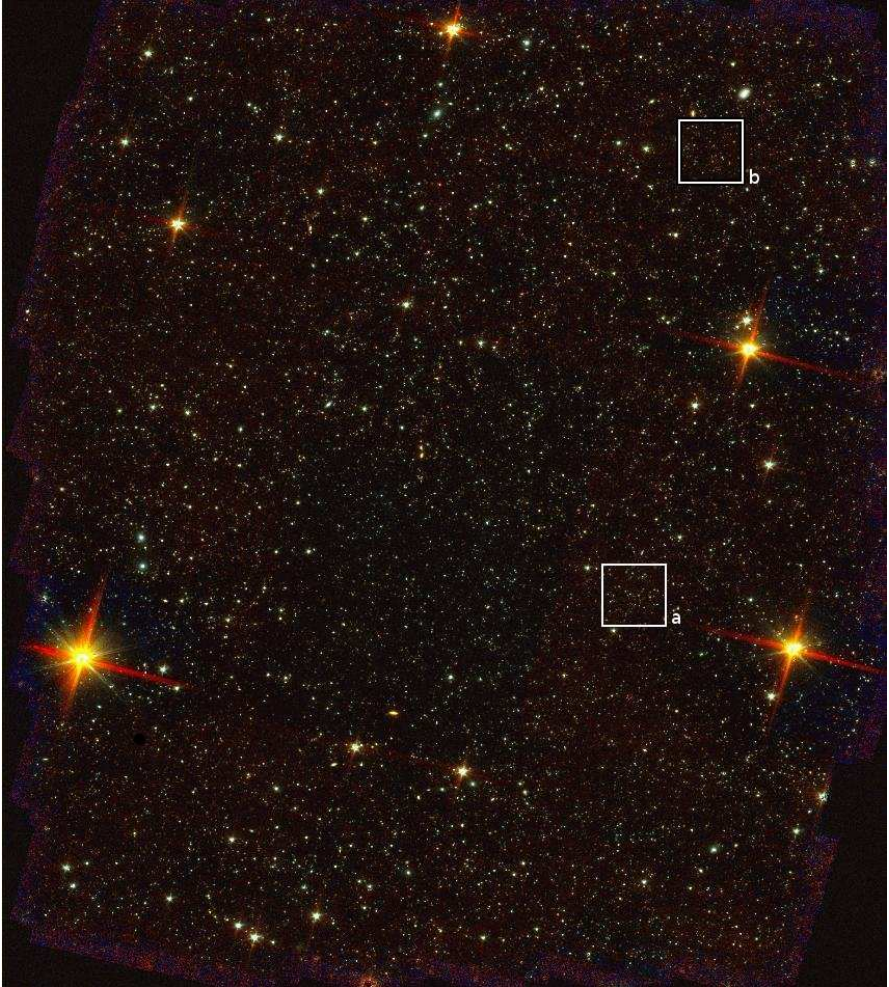**Figure 2.7** − Two-color composite image of the IRAC data of the E-CDFS, based on the 3.6 μm and 5.8 μm bands. The total field size is $38'$ × $48'$ and North is up. Figure 2.6 shows zoomed-in versions of the areas outlined in white.

2009). We use the v0.2 mosaic, which was released on a scale of $1.2''$ pixel^{-1}.

2.5 Source Detection and Photometry

2.5.1 Detection

Sources are detected and extracted using the SExtractor software (Bertin & Arnouts 1996) on a detection image. The detection image is an inverse-variance weighted average of the 3.6 and 4.5 μm images. The 3.6 and 4.5 μm band are the most sensitive IRAC bands and the combination of the two leads to a very deep detection image. To enable detection to a similar signal-to-noise limit over the entire field, we multiply the [3.6]+[4.5] image by the square root of the combined exposure map. This produces a "noise-equalized" image with approximately constant signal-to-noise, but different depth, over the entire field. Figure 2.1 shows the noise-equalized detection image in the background.

Subsequently we run SExtractor on the detection map with a 2 σ detection threshold. We choose this detection limit to be as complete as possible, at risk of severe confusion. We will discuss the matter of confusion later. In the detection process SExtractor first convolves the detection map with a detection kernel optimized for point sources. We use a 5×5 convolution mask of a gaussian PSF with a FWHM of 3 pixels. Furthermore, we require a minimum of 2 adjacent pixels above the detection threshold to trigger a detection. The resulting catalog contains 61,233 sources, 43,782 of which have a signal-to-noise ratio (S/N) > 5 at 3.6 μm.

Instead of our exposure time-detection image, we could have used the RMS map for detection. In practice, the RMS should be proportional to $1/\sqrt{(t_{exp})}$ and the choice of detection image should not significantly influence the output catalog. To test the correspondence of RMS and $1/\sqrt{(t_{exp})}$, we multiplied the RMS by the square root of the exposure time map, which results in a tight gaussian distribution with a width of $\sigma = 0.003$. Our exposure time detection image is therefore very similar to a detection image based on a RMS map.

As an aside, we note that SExtractor's RMS map underestimates the true noise as the pixels are correlated (see, e.g., Labbé et al. 2003). If we use SExtractor's RMS map in the catalog making process, we find ∼10% more objects than with our method, as expected. Many of these objects are near the edges of the image; none of them have a S/N > 5.

2.5.2 Photometry

2.5.2.1 Image Quality and PSF Matching

In order to obtain consistent photometry in all bands, we smooth all images (except MIPS) to a common PSF, corresponding to that of the 8.0 μm,

which has the broadest FWHM. To determine the FWHM, we compile a list of stars with $(J - K_s) < 0.04$. We select 5 different areas of the E-CDFS to check whether the PSF changes over the field. This is in particular important for the IRAC bands, which have a triangular-shaped PSF. Because of the rotation between the two epochs, the final IRAC PSF is a combination of two triangular-shaped PSFs that are rotated with respect to each other. This combined PSF can vary with position in the field of view and we first need to check how large these variations are. Radial profiles of the stars are determined using the IRAF task `imexam`. We find that the variation of the mean FWHM over the whole field of view is $< 5\%$ for all IRAC bands and there is no clear trend between the mean FWHM and the position on the field for any IRAC band. We convolve all images with a gaussian to produce similar PSFs in all bands. The mean original FWHM per band and the gaussian sigma values used for convolution are listed in Table 2.3.

2.5.2.2 $UBVRIz'JHK + IRAC$

We run SExtractor in dual-image mode, meaning that the program determines the location of sources in the combined [3.6]+[4.5] detection image, and then measures the fluxes in the smoothed science images in the exact same apertures. We perform photometry in fixed circular aperture measurements in all bands for each object, at radii of $1.5''$, $2.0''$, and $3.0''$. In addition we use SExtractor's autoscaling apertures based on Kron (1980) radii. Following Labbé et al. (2003) we refer to these apertures as APER(1.5), APER(2.0), APER(3.0), and APER(AUTO). We use these apertures to derive both color fluxes and total fluxes (see Labbé et al. 2003).

SExtractor provides a flag to identify blended sources that we include in our catalog as 'flag_blended'. In the SIMPLE catalog, $\gtrsim 60\%$[11] of all sources are flagged as blended. This is due to the large PSF of the camera and the depth of the image.

Given the large number of blended sources, it is useful to be able to identify only the most extreme cases of blending. If the sum of the aperture radius of a source and its nearest neighbor exceeds their separating distance and if the neighbor's flux is brighter than its own, we set the 'flag_blended' entry to 4. The percentage of sources suffering from this form of extreme blending is 32% for all sources with $S/N > 5$ at 3.6 μm.

While performing photometry we treat blended sources separately. Following Labbé et al (2003) and Wuyts et al. (2008), we use the flux in the color aperture to derive the total flux for sources that suffer from severe blending. For the identification of blended sources we prefer our own conservative blending criterion over SExtractor's blending flag, since this improves the

---

[11]62% of the sources suffer from blending (SExtractor's FLAGS keyword = 1), 61% of the sources have a close neighbor (FLAGS = 2), and for 66% of the sources FLAGS=1 $\vee$ FLAGS = 2.

comparison with other catalogs such as MUSYC and FIREWORKS significantly[12]. If we do not make a distinction between blended and non-blended sources, the comparison with other catalogs worsens slightly (< 0.02 magnitude on the mean deviation).

To determine the color fluxes, we use the circular apertures with $2''$ radius for all sources in all bands:

$$APER(COLOR) = APER(2.0). \qquad (2.1)$$

We calculate the total fluxes from the flux measured in the AUTO aperture. For sources with an aperture diameter smaller than $4''$ diameter, we apply a fixed aperture of $4''$.

$$APER(TOTAL) = \begin{cases} APER(AUTO), & Ap_{tot} > 4'' \\ APER(COLOR), & Ap_{tot} \leq 4'' \end{cases} \qquad (2.2)$$

Where Ap_{tot} is the circularized diameter of the kron aperture. If the source is blended (FLAG_BLENDED = 4), then

$$APER(TOTAL) = APER(COLOR)$$

Finally, we apply an aperture correction to the total fluxes using the growth curve of bright stars to correct for the minimal flux lost because it fell outside the "total" aperture.

For the IRAC data we apply individual growth curves for each band. The zeropoint for the aperture correction is based on the values listed in Table 5.7 of the IRAC Data Handbook[13]. We use the zeropoint in an aperture of $7.3''$ diameter (3 pixel radius in Table 5.7)[14]. For the MUSYC optical-IR data we use the K-band growth curve to correct the total fluxes in all bands. The aperture corrections are listed in Table 2.4.

2.5.2.3 The MIPS 24 μm Data

The photometry of the MIPS 24 μm image is performed in a different way, because of the larger PSF. Here, we use a deblending model to mitigate the

---

[12]The large number of sources of SExtractor blends would result in a catalog that mostly consists of blended sources ($\sim$90% for sources with a 5σ detection at 4.5 μm and in the K-band). These would all be assigned color fluxes that are, in our case, measured within a fixed aperture. The effect such a large fraction of aperture fluxes has on the comparison with the MUSYC catalog can be seen in Fig.A.1 of Appendix A. The upper left panel shows a large tail of bright sources that are significantly offset with respect to a one-to-one relation.

[13]http://ssc.spitzer.caltech.edu/irac/dh

[14]We use this aperture instead of the more generally used $12''$ diameter because of the high density of sources in our field, which would lead to source confusion at large radii. To avoid these complications, we determine the inner part of the growth curve from our data to a radius of $3.66''$ and combine it with the tabulated values from the handbook at larger radii. In this way we minimize the effect of blending.

Table 2.4 – aperture correctionstaken from Table 5.7 from the IRAC Data Handbook (corresponds to 3 pixel radius in that table), and $12''$ is the zeropoint aperture (see Section 2.3.3). The numbers in the second column are derived from our growth curves, the third column contains the corrections from the Data Handbook, and the total corrections are listed in the last column.

band	$4''$-$7.3''$	$7.3''$-$12''$	total correction
K	–	–	1.28
3.6 μm	1.22	1.112	1.35
4.5 μm	1.24	1.113	1.38
5.8 μm	1.37	1.125	1.55
8.0 μm	1.42	1.218	1.73

effects of confusion. We use the source positions of the IRAC 3.6 μm image, which has a smaller PSF, to subtract modeled sources from MIPS sources that show close neighbors, thus cleaning the image. After this procedure we perform aperture photometry in apertures of $6''$ diameter, and correct fluxes to total fluxes using the published values in Table 3.12 of the MIPS Data Handbook.

In principle a similar approach could have been attempted for the IRAC images themselves. Ground-based K-band data and space-based NICMOS imaging have been successfully used to deblend IRAC images (Labbé et al. 2006, Wuyts et al. 2008). However, whereas the resolution of our K-band image is appropriately high, the image is not deep enough for this kind of modeling.

2.5.3   Background and Limiting Depths

The determination of the limiting depth depends on the noise properties of the images. To analyze those, we place $\sim$4,000 circular apertures on the registered and convolved images and measure the total flux inside the apertures. Apertures are placed across the field in a random way, excluding all positions associated with sources using the SExtractor segmentation map. We use identical aperture positions for all bands, and repeat the measurements for different aperture sizes. The distribution of empty aperture fluxes can be fitted by a gaussian, which provides the flux dispersion of the distribution. The RMS depends on aperture size and is larger for larger apertures (see Fig. 2.8). The left panel shows the distribution of empty aperture fluxes for channel 1 for apertures of sizes $2''$, $3''$, and $4''$. The right panel shows how the RMS increases with aperture size for all IRAC bands. The noise level is higher than can be expected from uncorrelated Gaussian noise. The reason for this is that correlations between neighboring pixels were introduced while performing the data reduction and PSF matching (see also Labbé et al. 2003).

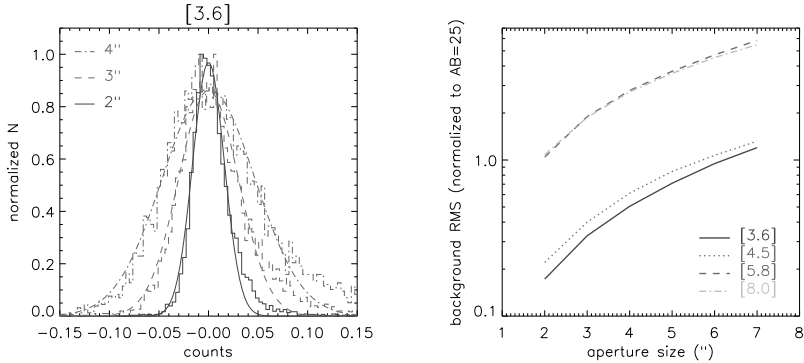The depth of our SIMPLE IRAC mosaic is a function of position, as

Figure 2.8 − Background RMS derived from the distributions of fluxes within randomly placed empty apertures. *Left* - Distribution of empty aperture fluxes within a 2" (*solid*), 3" (*dashed*), and 4" (*dash-dotted*) aperture diameter on the IRAC 3.6 μm image. The distribution is well described by a gaussian with an increasing width for increasing aperture size. *Right* - Background RMS as derived from flux measurements within empty apertures versus aperture size for the IRAC bands 3.6 μm (*solid*), 4.5 μm (*dotted*), 5.8 μm (*dashed*) and 8.0 μm (*dash-dotted*).

Table 2.5 − 5 σ limiting depths (total AB magnitude)

percentile	75%	50%	25%	(percentile of pixels)
exptime	>0.9	>1.5	>2.5	(hours)
area	∼1200	800	400	(area in arcmin^2 with at least this exposure time)
3.6 μm	23.66	23.86	24.00	(depth at 3.6 μm)
4.5 μm	23.50	23.69	23.82	(depth at 4.5 μm)
5.8 μm	21.68	21.95	22.09	(depth at 5.8 μm)
8.0 μm	21.69	21.84	21.98	(depth at 8.0 μm)

some parts have longer exposure times than others. Table 2.5 lists the total AB magnitude depths at 5 σ for point sources and the area over which this depth is achieved. Figure 2.9 provides a graphic representation of the limiting depths of all wavelength bands.

To investigate whether our measurement of the uncertainties in the IRAC photometry are reasonable, we compare the IRAC fluxes of epoch 1 with those of epoch 2. The results are shown in Fig. 2.10. The median offsets between the two epochs are printed in the lower left corner and are close to zero in each band. The scatter in each panel is small and comparable to the estimated RMS values.
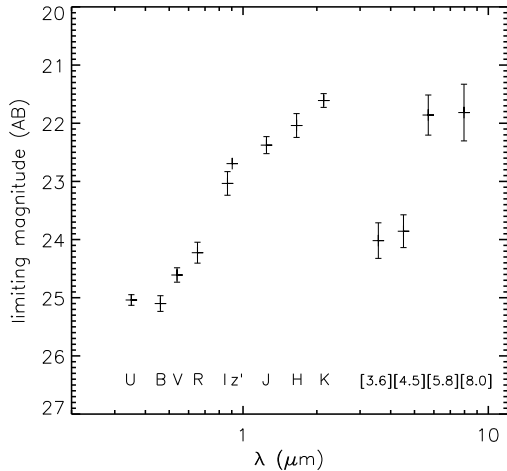
Figure 2.9 − Limiting magnitude vs. bandpass wavelength in the SIMPLE catalog. The limiting depths are $5\,\sigma$ total magnitudes of point sources measured in apertures with a $2.0''$ radius. Since the exposure time varies for each band, there is scatter around each limiting magnitude. The error bars denote the standard deviation of this scatter. Since we do not have an exposure map for the z'-band data, there is no error bar at the limiting magnitude of that band (see Taylor et al. 2009). The IRAC magnitude limits have been determined excluding the GOODS data.

2.5.4   Stars

We identify stars by their color and signal-to-noise ($J - K < 0.04 \wedge wK > 0.5 \wedge (S/N)_K > 5$) and find 978 stars in the total catalog. To test the validity of this selection criterion, we compare it to the BzK selection technique defined by Daddi et al. (2005). In the BzK-diagram stars have colors that are clearly separated from the colors of galaxies and they can be identified with the requirement $(z - K) < 0.3 \cdot (B - z) - 0.5$. From the 978 stars in the SIMPLE catalog with sufficient signal-to-noise in the B- and z-bands, 94% obey the BzK-criterion. In the BzK-diagram, the remaining 6% lie only slightly above the BzK stellar selection limit.

2.6   Derived Parameters

2.6.1   Spectroscopic and Photometric Redshifts

The E-CDFS is one of the principal fields for high-redshift studies and has consequently been the object of many spectroscopic surveys. Taylor et al. (2009) compiled a list of reliable spectroscopic redshifts from several of these surveys, which we cross-correlated with our SIMPLE catalog. The spectroscopic redshifts come from: Croom et al. (2001), Cimatti et al. (2002), le
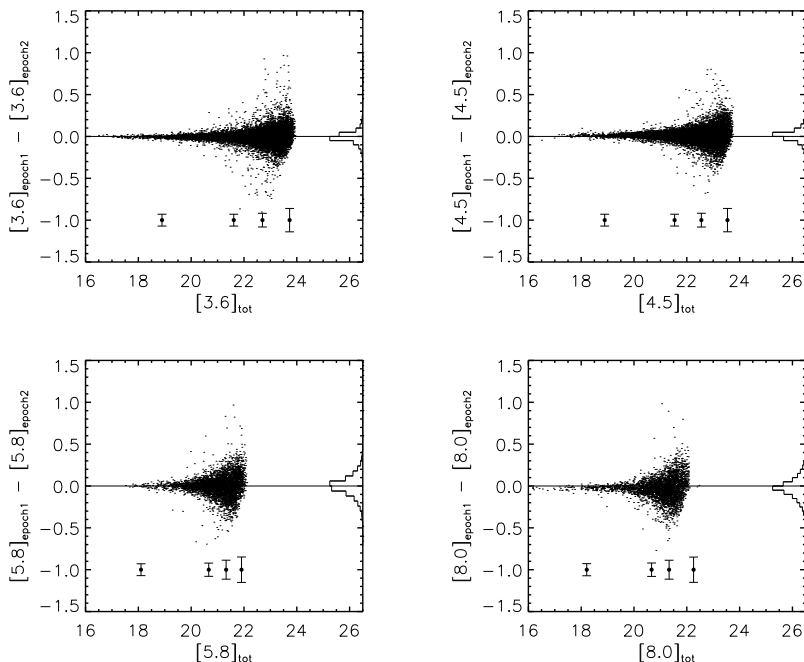
Figure 2.10 − Comparison between IRAC magnitudes of the first and second epoch of observations. The panels show the difference between the measured magnitudes of the four IRAC bands. At the right side of each panel, a histogram shows the distribution of the difference. The error bars are the mean errors in bins of equal number of sources, offset by -1 with respect to the measurements.

Fèvre et al. (2004), Strolger et al. (2004), Szokoly et al. (2004), van der Wel et al. (2004, 2005), Daddi et al. (2005), Doherty et al. (2005), Mignoli et al. (2005), Ravikumar et al. (2007), Kriek et al. (2008), Vanzella et al. (2008), Popesso et al. (2009), and Treister et al. (2009). The list contains 2,095 spectroscopic redshifts.

In addition, we include photometric redshifts from the COMBO-17 survey (Wolf et al. 2004) out to $z = 0.7$, which are very reliable at those redshifts. For the remainder of the sources we compute photometric redshifts using the photometric redshift code EAZY (Brammer et al. 2009). The EAZY algorithm provides a parameter Q_z, that indicates whether a derived photometric redshift is reliable. Brammer et al. (2009) show that for $Q_z > 2-3$ the difference between photometric and spectroscopic redshifts increases sharply and that quality cuts based on Q_z can reduce the fraction of outliers significantly. Therefore, when testing the accuracy of our photometric redshifts, we only include sources with $Q_z < 2$.

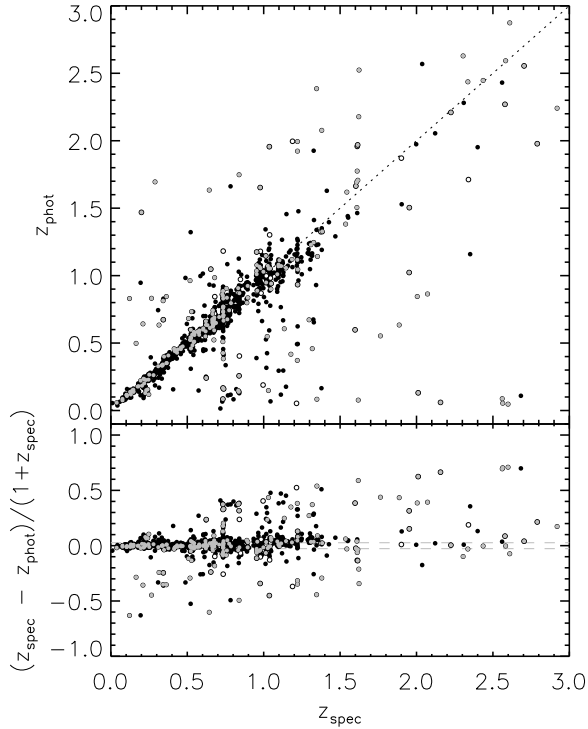Figure 2.11 shows the EAZY photometric redshifts compared against a

Figure 2.11 − Photometric and spectroscopic redshifts in the E-CDFS. *Upper panel* - Direct comparison between photometric and spectroscopic redshifts for 1,226 IRAC detected sources with reliable z_{spec} identification and coverage in all wavelength bands. The dotted line represents a one-to-one relationship. *Lower panel* - Residuals $dz = z_{spec} - z_{phot}/(1 + z_{spec})$ as a function of spectroscopic redshift. The σ_{NMAD} is 0.025, indicated by the dashed lines. Open circles denote AGN candidates, identified by their X-ray flux.

list of spectroscopic redshifts. The upper panel shows the direct comparison for sources with $S/N > 5$ in both K-band and 3.6 μm (a total of 1,280 sources, from which we remove 54 sources with $Q_z \geq 2$ (4%), resulting in a final sample of 1,226 sources). The lower panel shows $\Delta z/(1 + z_{spec})$, where $\Delta z = z_{\mathrm{phot}} - z_{\mathrm{spec}}$. X-ray detections are shown in gray.

To quantify the scatter, we determine the normalized median absolute deviation ($\sigma_{NMAD} = 1.48 \times$median $|x - \mathrm{median}(x)|$, which is a robust estimator of the scatter, normalized to give the standard deviation for a gaussian distribution). Overall the σ_{NMAD} of $|\Delta z|/(1 + z_{spec})$ is 0.025, but it varies with redshift, ranging from 0.024 at $z \sim 1$, 0.055 at $z \sim 1.5$, and 0.38 at $z \sim 2.0$. There is a significant fraction (8.2%) of outliers with $|\Delta z|/(1 + z_{spec}) > 5\sigma_{NMAD}$. This number agrees well with the 11% Taylor et al. (2009) found for the MUSYC catalog. Many of the outliers are detected in X-ray and are AGN candidates (43%). The high fraction of (candidate) AGN outliers could be explained by the fact that we do not have a AGN spectrum in our template set. EAZY photometric redshifts for X-ray detections are, therefore, uncertain. If we remove them from the sample, the overall accuracy improves and σ_{NMAD} becomes 0.024, 0.041, and 0.16 at redshifts $z \sim 1.0$, 1.5, and 2.0, respectively.

We also check whether the outliers suffer from blending. Out of the 101 outliers, 26 sources have a neighboring source whose APER(AUTO) exceeds their separating distance and whose flux is at least as bright as its own, which can affect their photometry. However, removing these sources from the sample does not decrease σ_{NMAD}, since there are many sources with nearby bright companions whose photometric and spectroscopic redshifts agree well.

2.6.2 Star Formation Rates, Rest-frame Photometry and Stellar Masses

In this section we describe the main characteristics of the the procedures for deriving star formation rates and stellar masses. For a more detailed description, the reader is referred to Chapter 4. We estimated SFRs using the UV and IR emission of the sample galaxies. We use IR template spectral energy distributions (SEDs) of star forming galaxies of Dale & Helou (2002) to translate the observed 24 μm flux to L_{IR}. First, we convert the observed 24 μm flux density to a rest-frame luminosity density at $24/(1 + z)\,\mu$m, then we extrapolate this value to a total IR luminosity using the template SEDs. To convert the UV and IR luminosities to a SFR, we use the calibration from Bell et al. (2005), which is in accordance with Papovich et al. (2006), using a Kroupa IMF:

$$\Psi/M_\odot \text{ yr}^{-1} = 1.09 \times 10^{-10} \times (L_{\mathrm{IR}} + 3.3\ L_{2800})/L_\odot, \qquad (2.3)$$

where $L_{2800} = \nu L_{\nu,(2800\mathring{A})}$ is the luminosity at rest frame 2800 Å, a rough

estimate of the total integrated UV luminosity (1216-3000Å).

To obtain stellar masses, we fitted the UV-to-8 μm SEDs of the galaxies using the evolutionary synthesis code developed by Bruzual & Charlot 2003. We assumed solar metallicity, a Salpeter IMF and a Calzetti reddening law. We used the publicly available HYPERZ stellar population fitting code (Bolzonella et al. 2000) and let it choose from three star formation histories: a single stellar population (SSP) without dust, a constant star formation (CSF) history and an exponentially declining star formation history with a characteristic timescale of 300 Myr (τ300), the latter two with varying amounts of dust. The derived masses were subsequently converted to a Kroupa IMF by subtracting a factor of 0.2 dex. We calculated rest-frame luminosities and colors by interpolating between observed bands using the best-fit templates as a guide (see Rudnick et al. 2003 and Taylor et al. 2009b for a detailed description of this approach and an IDL implementation of the technique dubbed 'InterRest'[15]).

2.7   Catalog Contents

The SIMPLE IRAC-selected catalog with full photometry and explanation is publicly available on the web[16]. We describe the catalog entries below.

- ID — A running identification number in catalog order as reported by SExtractor.
- x_pos, y_pos — The pixel positions of the objects based on the combined 3.6 μm + 4.5 μm detection map.
- ra, dec — The right ascension and declination in equinox J2000.0 coordinates, expressed in decimal degrees.
- i_colf — Observed color flux in bandpass i, where
  $i = U, B, V, R, I, z', J, H, K, irac1, irac2, irac3, irac4$ in circular apertures of $4''$ diameter. All fluxes are normalized to an AB magnitude zeropoint of 25.
- i_colfe — Uncertainty in color flux in band i (for derivation see Section 2.5.3).
- j_totf — Estimate of the total flux in band j, where
  $j = K, irac1, irac2, irac3, irac4$, corrected for missing flux assuming a PSF profile outside the aperture, as described in Section 2.5.2.1.
- j_totfe — Uncertainty in total flux in band j.
- ap_tot_j — Aperture diameter (in $''$) used for measuring the total flux in band j. This corresponds the circularized diameter of APER(AUTO) when the Kron aperture is used. If the circularized diameter is smaller than $4''$, the entry is set to APER(COL) = $4''$ (see Section 2.5.2).
- iw — Relative weight for each band i. For the IRAC bands the weights are determined with respect to the deepest area of the SIMPLE mosaic

---

[15]http://www.strw.leidenuniv.nl/~ent/InterRest
[16]http://www.strw.leidenuniv.nl/~damen/SIMPLE_release.html

without GOODS.
- *flag_star* — set to 1 if the source meets the criteria of Section 2.5.4.
- *flag_blended* — contains the SExtractor deblending flag, which indicates whether a source suffers from blending (bit = 1) or whether it has a close neighbor (bit = 2). If a source suffers from extreme blending (see Section 2.5.2) then bit = 4.
- *flag_qual* — bitwise added quality flag, that indicates whether a source lies in the GOODS area (bit = 1), lies in a stellar trail (bit = 2), falls outside the MUSYC field (bit = 4) or has been corrected for muxbleed.

Please note that all flux units in the catalog are converted to the same zero-point on the AB system: $AB\_MAG = 25. - 2.5 \log(flux)$.

2.8 Comparison to Other Catalogs

In this section we compare our SIMPLE catalog to the published catalogs of Taylor et al. (2009; MUSYC, E-CDFS) and Wuyts et al. (2008; FIRE-WORKS, CDFS). All catalogs cover (parts of) the same area in the sky. The important difference is that we detect sources in the IRAC 3.6 μm and 4.5 μm bands, whereas both the MUSYC as the FIREWORKS catalogs are K-band detected. The advantage of an IRAC-selected catalog is that IRAC probes the rest-frame NIR out to high redshift. The downside of IRAC selection is the lower resolution, which leads to confusion. The FIREWORKS catalog used a K-band selection specifically for this reason. We will investigate the effect these differences have on the catalogs below.

2.8.1 SIMPLE versus MUSYC

The optical-NIR part of the SIMPLE catalog (U-K) is based on the same data as the MUSYC catalog. The differences lie in the PSF, detection method, and photometry. Taylor et al. (2009) determine their total fluxes in a similar way as we do. However, they include an extra correction based on the measurement of the background, which they measure themselves instead of using the value derived by SExtractor and they do not make a distinction between blended and non-blended sources. We cross-correlated the two catalogs and in Fig. 2.12 we present the comparison.

Each panel shows sources with S/N > 10 in IRAC 4.5 μm and in the relevant band of the panel. We also applied a weight cut in K, $wK > 0.75$, recommended by Taylor et al. (2009). We determined the median offsets in different magnitude bins and show them at the bottom of each panel. The first number (*in black*) represents the median offset of all sources, the gray numbers represent the median offset in each magnitude bin; they are $\lesssim 0.05$ in all bands. The error bars represent the formal expected photometric errors, which are dominated by the Poisson uncertainties in the background. The offsets at bright magnitudes are not caused by Poisson statistics, but most
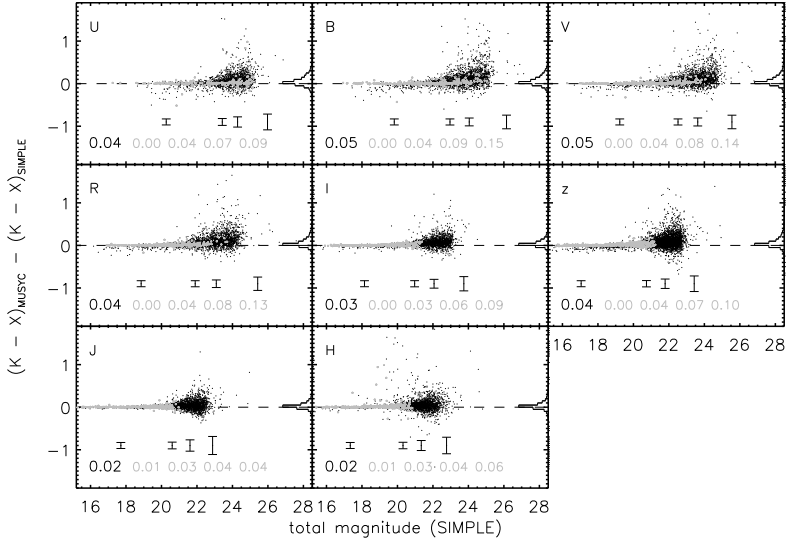
Figure 2.12 – Direct comparison between MUSYC and SIMPLE colors in the overlapping bands $(U - K)$ for sources with S/N> 10 in SIMPLE K-band. At the right side of each panel, a histogram shows the distribution of the offsets. Stars are shown in gray. The median offset is indicated at the lower left corner of each panel. For each band only the SIMPLE sources with S/N> 5 are included. The error bars indicate the formal errors expected from the SIMPLE and MUSYC photometric errors. They are mean values in bins of equal number of sources and are offset by -1 with respect to the measurements.

likely by slight systematic differences in methodology. We investigated the bright sources in the U-, B-, V-, and R-band, which show an offset of > 0.2 in color and found that this is an effect of the aperture sizes that were used. The MUSYC fluxes were determined using SExtractor's MAG_ISO, enforcing a minimum aperture diameter of $2.5''$. For the SIMPLE catalog, we used a fixed $4.0''$ aperture diameter. The large color differences at the bright end occur for galaxies for which the differences in aperture size are large too (factor 1.5 and greater).

2.8.2 SIMPLE versus FIREWORKS

2.8.2.1 *Photometry*

The FIREWORKS catalog is constructed from observations in wavelength bands that in some cases differ from the ones we use. The $UBVR$ and I data come from the Wide Field Imager and are the same as we use, except for the U-band, for which the FIREWORKS uses the U_{38}-imaging. The z_{850}-band image was observed by HST, J, H, and K_s data come from ISAAC. The

IRAC images were taken by the GOODS team and are nearly the same as the ones we use. Figure 2.13 shows the comparison of all these bands against each other. As in Fig. 2.12, we only show sources with S/N > 10 in IRAC 4.5 μm and in the relevant band of the panel, with a weight in K-band larger than 0.5. The median values are once more shown at the bottom left and the error bars again represent the expected formal errors.

The FIREWORKS catalog allows easy identification of blended sources and we have removed these from Fig. 2.13, since they worsened the comparison. This can be seen in Fig. B.1 in Appendix B, which shows the difference in K-band magnitude for FIREWORKS and SIMPLE. In that figure we did include the blended FIREWORKS sources and marked them in red. They form a specific tail and we have removed them from all further analysis. The sources that suffer from extreme blending in the SIMPLE catalog do not take up such a specific locus in the comparison figures. Excluding them from the sample does not significantly affect the comparison and therefore we keep them in the sample.

In Fig. 2.13, the comparison between FIREWORKS and SIMPLE tails upward at the faint end. There, the SIMPLE fluxes are brighter than FIRE-WORKS. This could be due to the fact that the SIMPLE apertures are quite large and will catch some light from neighboring sources.

A direct comparison between SIMPLE and FIREWORKS illustrates the strengths of both data sets as can be seen in Fig. 2.14, which shows a color magnitude diagram of both catalogs for sources with S/N > 5 in the relevant bands. The envelopes at the bright end agree well, but at the faint end FIREWORKS reaches greater depth. The advantage of the SIMPLE survey is its large area, and thus its large number of sources. Out to a magnitude of 21.5 in [3.6], the SIMPLE catalog contains 4061 sources at 5 σ, compared to 1250 for FIREWORKS.

2.8.2.2   Derived Properties

In addition to a comparison of the photometry, we compare derived quantities of the FIREWORKS and SIMPLE catalogs. Figure 2.15 shows the comparison between mass, (specific) star formation rate, MIPS 24 μm flux, and redshift. Mean values in bins of equal number of sources are indicated by the white line and given at the bottom of each panel. The panels with MIPS 24 μm flux and SFR show the best agreement, although the scatter in the comparison of the SFR is substantially higher than it is for the MIPS fluxes. This is caused by the difference in photometric redshifts. If we use FIREWORKS photometric redshifts to determine the SIMPLE SFRs, the scatter in the SFRs is reduced to the scatter in MIPS fluxes.

The scatter is highest in the panels where masses and sSFRs are compared, quantities that depend on photometric redshifts and model assumptions. These are, therefore, more susceptible to systematic errors. Since the
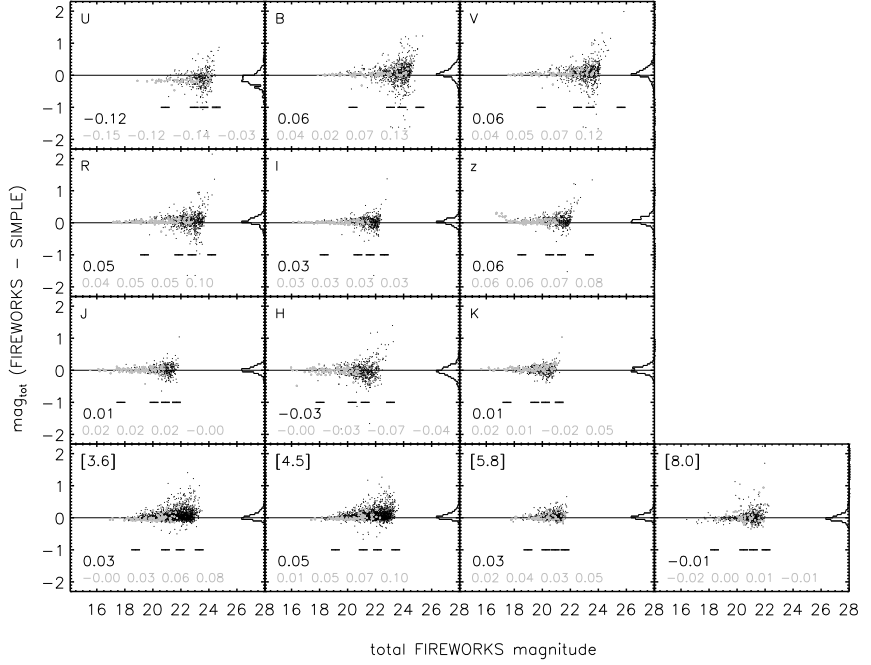
Figure 2.13 − Direct comparison of total magnitudes for sources with S/N> 10 at 4.5 μm for the $U − K$ + IRAC bands of the FIREWORKS catalog and our SIMPLE catalog. At the right side of each panel, a histogram shows the distribution of the offsets. The median offset is indicated at the lower left corner of each panel. For each band only the SIMPLE sources with S/N> 10 are included. Stars are shown in gray. The error bars indicate the formal errors expected from the SIMPLE and FIREWORKS photometric errors. They are mean values in bins of equal number of sources and are offset by -1.5 with respect to the measurements. All blended FIREWORKS sources have been removed from this figure.

Figure 2.14 $-$ *J-K* vs. [3.6] color-magnitude diagram for IRAC-selected sources in the E-CDFS. Stars (*dark gray stars*) are identified by their *J-K* color (see Section 2.5.4). Overplotted in light gray are the values from the FIREWORKS catalog, which reaches greater depth, but contains fewer sources out to a magnitude of 21.5. All blended FIREWORKS sources have been removed from this figure.
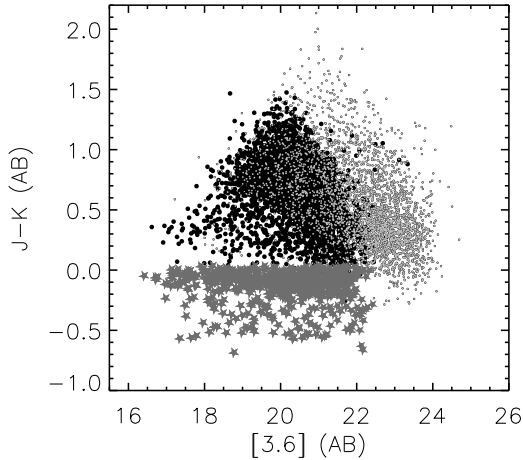
masses are derived in similar ways for SIMPLE and FIREWORKS (same models, dust extinction law, metallicity, and IMF), systematics in the modeling can not be responsible in this comparison. We redetermined our masses using FIREWORKS photometric redshifts and found that this reduces the number of outliers in the mass-comparison panel, but not the scatter. The main reason for the scatter in mass and sSFR is signal-to-noise. The mean absolute deviation of the scatter in the mass comparison is 0.5 for sources with $(S/N)_K < 10$. For sources with a $(S/N)_K \sim 20$ the scatter is reduced to 0.1. Further discussion on the differences between FIREWORKS and SIMPLE fluxes and derived parameters can be found in Appendix C.

2.9   Summary

The *Spitzer* IRAC/MUSYC Public Legacy Survey in the Extended Chandra Deep Field South (SIMPLE) consists of deep IRAC observations (1-1.5 hours per pointing) covering the $\sim$1,600 arcmin^2 area surrounding the GOODS CDF-South. This region of the sky has extensive supporting data, with deep observations from the X-rays to the thermal infrared. We describe in detail the reduction of the IRAC observations and the treatment of the main artifacts, such as column pulldown, muxbleed and muxstriping. The final SIMPLE IRAC mosaics were complemented with $10' \times 12'$ GOODS IRAC images in the center and are available on-line.

We also present a 13-band, IRAC-detected catalog based on the SIMPLE images and existing public optical and NIR data of the MUSYC project. The wavelength bands that are covered are $UBVRIz'JHK$ and the four IRAC bands at 3.6, 4.5, 5.8, and 8.0 μm. The 5 σ IRAC depths are 23.8, 23.6, 21.9,
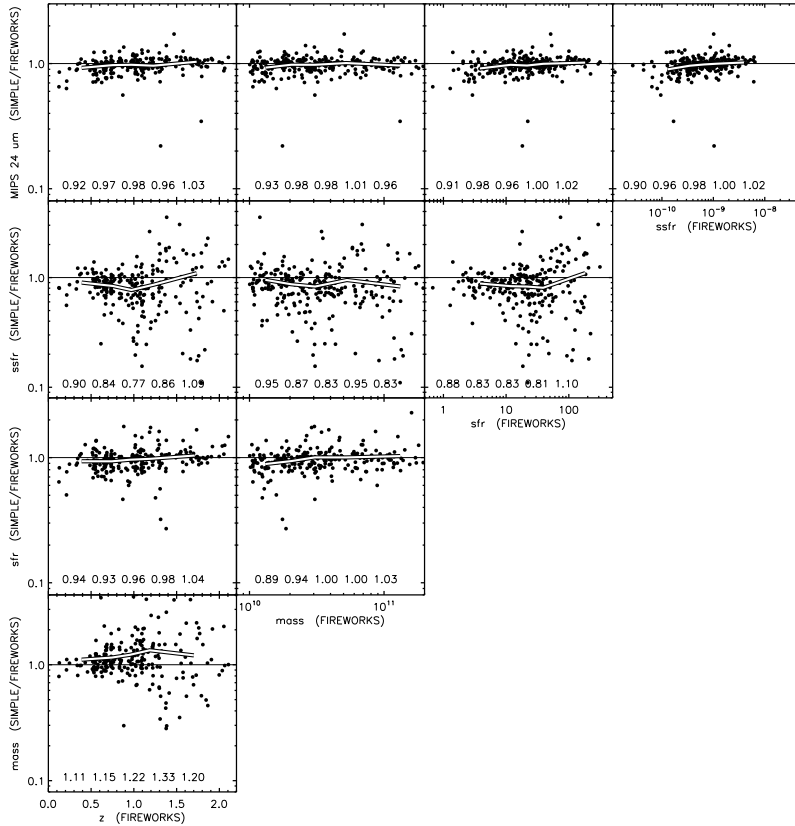
Figure 2.15 – Comparison between various observed or derived quantities in FIRE-WORKS and SIMPLE. The white line indicates a binned mean of the difference in each quantity. The mean values are derived for five intervals of equal number of sources and are shown at the bottom of each panel. All blended FIREWORKS sources have been removed from this figure.

and 21.7 for [3.6], [4.5], [5.8], and [8.0], respectively. The reduced images and catalog are publicly available on the web.

We compare the photometry of the SIMPLE survey to that of the MUSYC and FIREWORKS catalogs and find overall a good agreement. There is a small offset in the U, B, V-bands but this can be well explained by the difference in photometric technique.

Acknowledgments

Appendix A - Flux Apertures

When performing photometry we use SExtractor's AUTO aperture, since it is more robust than for instance the ISOCOR aperture, which depends more sensitively on the depth of the image. In addition, it allows an easy comparison with other catalogs such as the MUSYC and FIREWORKS catalogs, which are both based on AUTO apertures. In Fig. A.1 we show the effect different apertures have on the comparison between our catalog and the MUSYC catalog. As expected, the AUTO fluxes give the best agreement. The cause of the offset at the bright end of the panel showing the AUTO fluxes is discussed in Section 2.8.1.

Appendix B - Confusion

While building the SIMPLE catalog, we treated blended (or confused) sources very conservatively and only identified the sources that most severely suffered from blending. We were not able to simply use the quality flags SExtractor provided, since those identified 60% of all sources as blended. Performing photometry on these "blended" sources in a way commonly used for blended sources, exacerbated the disagreement with other catalogs (see Section 2.5.2).

In addition, it was not possible to model blended sources using a deep source map at lower wavelength, since our K-band data were not deep enough (see Section 2.5.2.3). The effect blending has on photometry is clear in e.g., the FIREWORKS catalog, where blended sources were identified by their SExtractor flags and take up 12% of the sample. Figure B.1 shows the comparison between the total $K-$band magnitude of SIMPLE and FIRE-WORKS. Blended sources in the FIREWORKS catalog are represented by open circles and form a distinct plume of scattered sources. Since the plume contains only blended sources, we removed these sources from all further analysis, since their photometry must be inaccurate (i.e., Figures 2.13, 2.14, and 2.15).

Unfortunately, we could not apply this trick to the SIMPLE catalog. In Section 2.5 we identified the sources that suffer from severe blending. We have not indicated them in Fig. B.1, since they do not fill a specific locus,
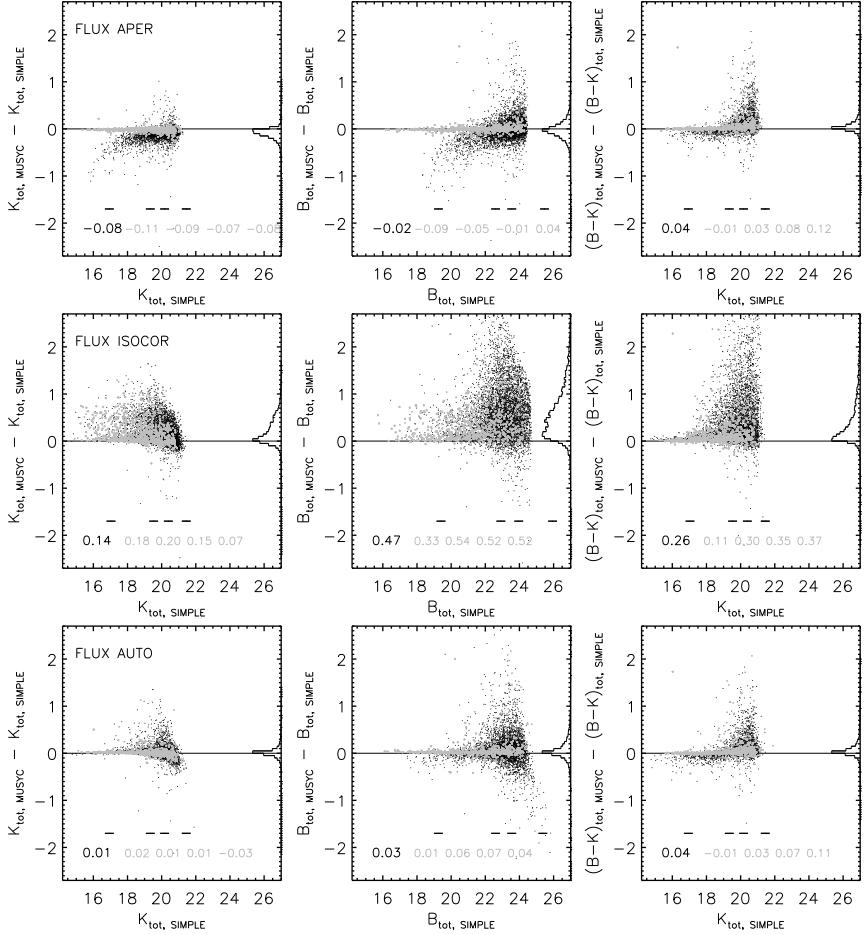
Figure A.1 – Comparison between MUSYC and SIMPLE magnitudes in the *B*- and *K*-bands for different apertures. The apertures used are (from top to bottom row) fixed apertures of 4″ (FLUX APER), corrected isophotal apertures (FLUX ISOCOR), and flexible elliptical apertures (FLUX AUTO). Stars are shown in gray. The median offset is indicated at the lower left corner of each panel. For each band only the SIMPLE sources with S/N> 5 are included. In the construction of this figure no distinction has been made between blended and non-blended sources.

Figure B.1 – Comparison between FIREWORKS and SIMPLE for K-band total magnitude. Sources that are blended in the FIREWORKS catalog are shown in gray. We removed these sources from all analysis (i.e., Figures 2.13, 2.14, and 2.15). The sources that are flagged as blended by SExtractor take up $\gtrsim 60\%$ of the 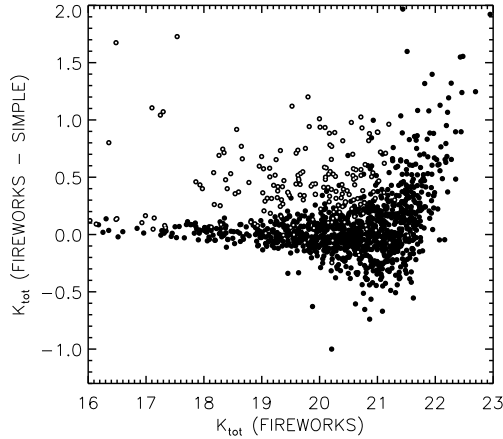complete SIMPLE sample and even a higher fraction (98%) of the sources shown above, which are relatively bright $((S/N)_K > 5)$.

but instead are spread out evenly over the whole figure. It is, therefore, not possible to quantify the effect blended sources have on our photometry and derived parameters. However, we can determine how results that we will discuss later in this thesis would change if we removed sources that are severely blended. In Chapter 4 we determine the redshift evolution of the average sSFR. It is interesting to see if removal of the sources that suffer from confusion will affect the results. We redetermined mean sSFRs for two different samples, removing all sources that a) were flagged as blended by SExtractor, and b) we consider blended by our own criterion. In the latter case, the mean sSFRs change by less than 5%, in no preferred direction. When all sources that were flagged as blended by SExtractor are removed, less than 10% of the sources remain in each mass bin. Whereas the resulting mean sSFRs differ up to ~40% from the original values, the change is not in one specific direction and the new values are simply scattered around the old ones. Hence, the global trends stay remarkably intact and the fact that our sample contains blended sources has no impact on the results.

Appendix C - Scatter between FIREWORKS and SIMPLE

In the comparison of the photometric and derived properties of the SIMPLE and FIREWORKS catalogs, we observed a large scatter. In Fig. C.1 we show
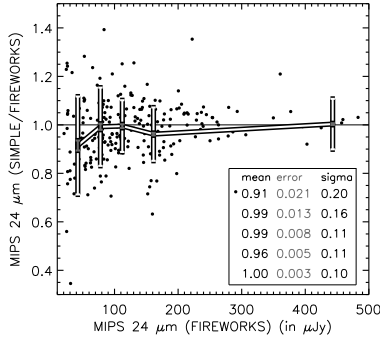
Figure C.1 – Comparison between FIRE-
WORKS and SIMPLE for MIPS 24 μm to-
tal magnitude. The mean values are indi-
cated by the white line and printed in the
lower right corner, together with the stan-
dard deviation in each bin. The formal er-
rors obtained from our deblending routine
are smaller than the observed standard de-
viation. It is clear however, that the MIPS
24 μm fluxes are consistent with each other
within 10-20%.

the comparison between MIPS fluxes. The mean values of the difference are
indicated by the white line and are printed in white in the lower right corner.
Error bars represent the standard deviation in each bin and are printed in
the lower right corner. The FIREWORKS MIPS fluxes have been determined
based on a K-band image with high spatial resolution. On the other hand,
the SIMPLE fluxes were determined using our IRAC imaging as a reference
(see Section 2.5.2.3). The IRAC data are deep, but have a PSF which is
much larger, leading to more confusion. This causes the difference in MIPS
fluxes, which are relatively modest (mean absolute deviation of 10% at the
bright end).

In Section 2.8.2.2 we stated that the scatter in mass was not caused by
photometric redshift errors. This can be inferred from Fig. C.2, which shows
the difference in masses from FIREWORKS and SIMPLE against spectro-
scopic (*left*) and photometric (*right*) redshift. Despite a few dramatic outliers,
it is not clear that the scatter is much reduced when using spectroscopic red-
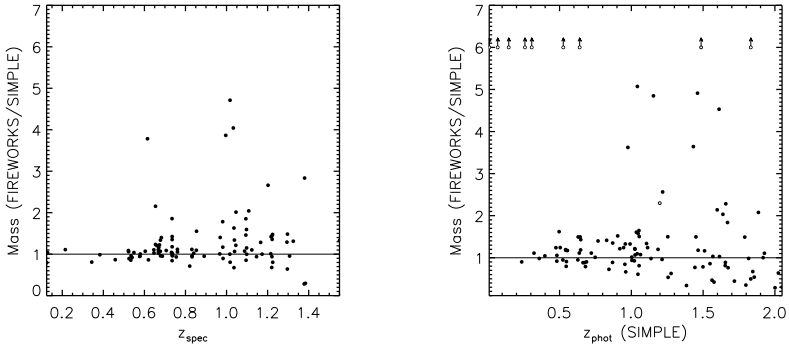shifts only.

Figure C.2 – Comparison between the masses of FIREWORKS and SIMPLE versus a) spectroscopic and b) photometric redshifts. The red points in the right panel represent sources with photometric redshifts that differ more than 0.5 between FIREWORKS and SIMPLE. Despite these outliers, it is clear that the observed scatter is not caused by photometric redshift errors.

References

Arnouts, S., et al. 2001, A&A, 379, 740

Ashby, L. N. et al. 2009, ApJ, 701, 428

Barger, A. J., Cowie, L. L., Smail, I., Ivison, R. J., Blain, A. W., Kneib, J.-P. 1999, AJ, 117, 2656

Bertin, E. & Arnouts, S. 1996, A&AS, 117, 393

Brammer, G. B., van Dokkum, P. G., Coppi, P. 2008, ApJ, 686, 1503

Cimatti, A., et al. 2002, A&A, 392, 395

Cimatti, A., et al. 2004, Nature, 430, 184

Cohen, M., Megeath, S. T., Hammersley, P. L., Martín-Luis, F., Stauffer, J. 2003, AJ125, 2645

Daddi, E., Cimatti, A., Pozzetti, L., Hoekstra, H., Röttgering, H. J. A., Renzini, A., Zamorani, G., Mannucci, F. 2000, A&A, 361, 535

Daddi, E., et al. 2005, ApJ, 626, 680

Dickinson, M, et al. The Mass of Galaxies at Low and High Redshift: Proceedings of the European Southern Observatory and Universitäts-Sternwarte München Workshop Held in Venice, Italy, 24-26 October 2001, ESO ASTROPHYSICS SYMPOSIA. Edited by R. Bender and A. Renzini. Springer-Verlag, 2003, p. 324

Elston, R., Rieke, G. H., & Rieke, M. J. 1988, ApJ, 331, 77

Erben T., et al. 2005, AN, 326, 432

Fazio, G. G., et al. 2004, ApJS, 154, 10

Franx, M. et al. 2003, ApJ, 587, 79

Gawiser, E., et al. 2006, ApJS, 162, 1

Giacconi, R., et al. 2002 ApJS, 139, 369

Giavalisco, M., & the GOODS Team 2004, ApJ, 600, L93

Hildebrandt, H., et al. 2006, A&A, 452, 1121

Kriek, M., et al. 2008, ApJ, 677, 219

Kroupa, P. 2001, MNRAS, 322, 231

Labbé, I. et al. 2003, AJ, 125, 1107

Labbé, I., Bouwens, R., Illingworth, G, D., Franx, M. 2006, ApJ, 649, 67

Lehmer et al. 2005, ApJS, 161, 21

le Fèvre, O., et al. 2004, A&A, 428, 1043

Lonsdale, C. J. et al. 2003, PASP, 115, 897

Luo, B., et al. 2008, ApJS, 179, 19

Martin, D. C., et al. 2005, ApJ, 619, 1

Magnelli, B., Elbaz, D., Chary, R. R., Dickinson, M., Le Borgne, D., Frayer, D. T., Willmer, C. N. A. 2009, A&A, 496, 57

Miller, N. A., Formalont, E. B., Kellermann, K. I., Mainieri, V., Norman, C., Padovani, P., Rosati, P., Tozzi, P, 2008, ApJS, 179, 114

McCarthy, P. J., et al. 2001, ApJ, 560, 131

Monet, D. G. et al. 2003, AJ, 125, 984

Popesso, P., et al. 2009, A&A, 494, 443

Quadri, R., et al. 2007, AJ, 134, 1103

Ravikumar, C. et al. 2007, A&A, 465, 1099

Reach, W. T., et al. 2005, PASP, 117, 978

Rix, H.-W, et al. 2004, ApJS, 152, 163

Rudnick, G., et al. 2003, ApJ, 599, 847

Sanders, D. B., et al. 2007, ApJS, 172, 86

Spinrad, H., Dey, A., Stern, D., Dunlop, J., Peacock, J., Jimenez, R., Windhorst, R. 1997, ApJ, 484, 581

Steidel, C. C., Giavalisco, M., Dickinson, M., Adelberger, K, L. 1996, AJ, 112, 352

Steidel, C. C., Adelberger, K. L., Giavalisco, M., Dickinson, M., Pettini, M. 1999, ApJ, 519, 1

Szokoly, G. P., et al. 2004, ApJS, 155, 271

Taylor, E. N., et al. 2009, ApJS, 139, 369

Treister, E., et al. 2009, ApJ, 693, 1713

Vanzella, E., et al. 2008, A&A, 478, 83

van Dokkum, P. G., et al. 2006 ApJ, 638, 59

Wolf, C., et al. 2004, A&A, 421, 913

Wuyts, S., Labbé, I., Förster-Schreiber, N., M., Franx, M., Rudnick, G., Brammer, G., B., van Dokkum, P. G 2008, ApJ, 682, 985

Zheng, X. Z., Bell, E. F., Papovich, C., Wolf, C., Meisenheimer, K., Rix, H.-W., Rieke, G. H., Somerville, R. 2007, ApJ, 661, 41

_3_

Sample Selection by Mass and Luminosity

We analyze how rest-frame optical and UV-selected samples can be used to construct mass-selected samples. To that end, we use a deep sample of galaxies in the CDFS, based the FIREWORKS catalog. We draw galaxy samples with redshifts $1 < z < 2$, limited in the rest-frame UV, rest-frame B-band, and mass, respectively. We find a tight correlation between mass and rest-frame B-band; more massive galaxies are typically more optically bright. A well-defined upper limit exists in the M/L_B-ratio, corresponding to quiescent galaxies. A sample selected in rest-frame B-band can, therefore, serve as a basis for a mass-selected sample. In contrast, mass and rest-frame UV luminosity are not tightly correlated; there is a paucity of high-mass galaxies with bright rest-frame UV-luminosities, and we do not find a useful upper limit to the M/L_{UV}-ratio. It is not possible to convert a UV-limited sample into a mass-limited sample in a straightforward way. In addition, we analyze how luminosity-selected samples can give deviant correlations of specific star formation with mass. As star forming galaxies tend to be bluer than quiescent galaxies, they enter luminosity-selected samples preferentially, and affect the relation between specific star formation and mass. We show that this can lead to elevated values of the specific star formation, and a steepening of the slope of the specific star formation rate with mass. Other parameters which depend on color more indirectly can also be affected. As an example, quiescent red galaxies have smaller sizes than star forming galaxies with the same mass. Hence luminosity-selected samples will produce a relation between mass and size with larger sizes than properly mass-selected samples. These results strengthen the case for using mass-selected samples in the analysis of galaxy properties.

Maaike Damen, Natascha M. Förster Schreiber, Marijn Franx, Ivo Labbé,
Pieter G. van Dokkum, Stijn Wuyts
to be submitted to the Astrophysical Journal

3.1   Introduction

WHEN studying the assembly and evolution of galaxies, a good census of the mass is pivotal. It is important to trace the evolutionary history of galaxies as a function of time and mass, which requires large samples of galaxies. Such samples are typically selected by flux (or flux-related properties, such as surface brightness, magnitude and color) or mass[1]. Flux-limited samples do not select the same absolute magnitudes at increasing redshifts. They contain preferentially brighter galaxies toward higher redshifts and should, therefore be either corrected for distance modulation and bandpass shifting, or used in a narrow redshift regime.

Color selection is very efficient in selecting large numbers of galaxies in a specific redshift regime. A very effective color selection technique is the Lyman Break technique pioneered by Steidel et al. (1996, 1999), which uses observed optical wavelengths to select galaxies at $z > 3$ (LBGs), or at $1.4 < z < 2.5$ (BM/BX). The optical selection bands correspond to the rest-frame ultra-violet (UV) at those redshifts. A different technique, based on a NIR-color-criterion, selects redder (more dusty or older) galaxies at $z \geq 2$ (DRGs, Franx et al. 2003, Labbé et al. 2004). A third example uses BzK-colors to select z $\sim$ 2 galaxies (Daddi et al. 2004).

Several authors have studied and compared the properties of these selection techniques (Reddy et al. 2005; van Dokkum et al. 2006; Quadri et al. 2007). These studies show that samples selected by different color techniques have some overlap[2] between the two samples, but generally complement each other. When applying color criteria, it is important to realize that the efficiency of e.g., the DRG-criterion is not constant, but depends on magnitude (Wuyts et al. 2009c). At the brightest K-band magnitudes, most DRGs are at $z < 2$. To summarize: each color criterion is efficient in selecting a large sample of galaxies with a range of properties at a well-defined redshift interval; combined, color selection techniques provide a reasonably complete census of the high redshift galaxy population.

A third way of sample selection is by mass. Mass-selected samples are, by definition, extracted from flux-limited samples and are generally quite different from their parent samples. This is usually due to variations in the star formation histories (SFHs), which can cause galaxies of similar mass to have a wide range in luminosities. Mass-selected samples are generally used to overcome the limitations of luminosity-selected samples. Luminosity can change rapidly with time (e.g., due to bursts of star formation), and evolutionary differences in luminosity-selected samples can be caused by the inclusion of subsamples, instead of true evolution of the galaxies.

---

[1] At every instance of the word 'mass' in the remainder of this chapter, we mean the stellar mass

[2] The overlap between color-selected samples can actually be quite high. For example, starforming galaxies at $z \sim 2$, i.e. BM/BX and sBzK galaxies, have optical and near-IR color distributions that show up to 80% overlap (Reddy et al. 2005).

To study the evolution of galaxies it is therefore important to have mass-selected samples. In this chapter, we will explore rest-frame optical and rest-frame UV-selected samples and compare them to a mass-complete sample.

We will keep this exploration simple and will limit ourselves to two luminosity cuts in the rest-frame B-band (L_B) and rest-frame UV (at 1700 Å; L_{1700}). We will not include color selection techniques, since their properties can be roughly deduced from the luminosity limited samples we use.

We will also investigate the impact of luminosity- and mass-selected samples on well-known relations between specific star formation rate (sSFR), size, and mass. This is in the same line as work done at z $\sim$ 1 on the morphology-density relation by Holden et al. (2007) and Tasca et al. (2009). These authors compared the evolution of the morphology-density relation of L_B- and mass-selected samples and found significant differences.

3.2   Data

For the analysis we use the FIREWORKS catalog for the GOODS-CDFS, which is a multi-wavelength catalog generated by Wuyts et al. (2008). It combines deep space- and ground-based observations into a K-selected catalog consisting of the following bands: $U_{38}BVRI$ (WFI), $B_{435}V_{606}i_{775}z_{850}$ (ACS), JHK_s (ISAAC), 3.6-8.0 μm (IRAC) and 24 μm (MIPS). It has a 5 sigma depth in K_s of $\sim$24.3 and a total area of 138 arcmin^2. For details on observations, source detection and astrometry we refer to Wuyts et al. (2008). Using the CDFS X-ray catalog of Giacconi et al. (2002), we flagged all X-ray detected sources in the sample as they are likely AGN. We restricted the selection to sources with a signal-to-noise higher than 10 in the K_s-band, which results in a total sample size of 5,274 sources. This sample is also used in Chapter 5 to derive a mass-selected sample and compare the observed growth rate of galaxies to model predictions.

3.3   Derived Quantities

Wuyts et al. (2008) compiled a list of 1477 spectroscopic redshifts. For sources without a spectroscopic redshift, Wuyts et al. (2008) determined photometric redshifts using the photometric redshift code EAZY (Brammer et al. 2008). We use the masses, extinction values, SFRs, and ages that were derived using modeling of Spectral Energy Distributions (SEDs) by N. M. Förster Schreiber et al. (in preparation), for a Calzetti extinction law, solar metallicity, and a Salpeter IMF. We renormalized masses and SFRs to a Kroupa (2001) IMF by dividing them by $10^{0.2}$.

Rest-frame luminosities were derived by interpolating between observed bands using the best-fit templates as a guide (see Rudnick et al. (2003) for a detailed description of this technique and Taylor et al. (2009) for the IDL

implementation of the algorithm, dubbed 'InterRest'[3]). More details of the fits and accuracies of the derived parameters can be found in Wuyts et al. (2008) and N. M. Förster Schreiber et al. (in preparation).

In addition to the SFRs determined by SED-fitting, Wuyts et al. (2009b) independently derived SFRs using a combination of the rest-frame UV and IR emission. In this way both the light of young, unobscured stars and the light reprocessed by dust are taken into account and a complete census of the bolometric luminosity of young stars can be obtained. The MIPS 24 μm is converted into a total IR luminosity using a wide range of templates from Dale & Helou (2002). The SFR was determined following Wuyts et al. (2009b), assuming:

$$\Psi/M_\odot \ \mathrm{yr}^{-1} = 1.09 \times 10^{-10} \times (L_{\mathrm{IR}} + 3.3 \ L_{2800})/L_\odot. \qquad (3.1)$$

The sizes we use were derived by Franx et al. (2008) following the procedures of Trujillo et al (2006) and Toft et al. (2007). In short, the sizes were determined in the band redwards of the redshifted 4000 Å break and closest to the rest-frame g-band. Each galaxy was fit by a convolved Sersic profile using GALFIT (Peng et al. 2002). For more details on the procedure and systematic uncertainties, we refer to Franx et al. (2008).

3.4   Mass versus Rest-Frame Luminosity

In the left panel of Fig. 3.1 we show mass versus rest-frame optical luminosity for galaxies between $1 < z < 2$. We use this redshift range in the rest of this chapter, unless explicitly stated otherwise. The white line indicates the completeness limit due to the underlying K-band selection of the FIRE-WORKS catalog. To determine this limit, we selected the sources at redshift $1 < z < 2$ and scaled the masses and B-band luminosities down to the K-band detection limit at 10 σ. In this way we determined the limiting mass and rest-frame B luminosity that could have been observed for each galaxy, given the detection limit. The white line indicates the limit for which 75% of the galaxies would be detected[4].

The left panel shows that there is a good correlation between mass and L_B. The galaxies do not lie on a line; they span a range of one order of magnitude in L_B at $\log(M_*) = 10.5$. However, this is only to be expected, as different galaxies have different colors and different M/L-ratios. Overall the masses of galaxies in the sample increase with increasing L_B. Most importantly, we note that at every given mass, there is a value of L_B below which we find no (or very few) galaxies. We indicate this with the dotted

---

[3]http://www.strw.leidenuniv.nl/∼ent/InterRest
[4]This technique for determining the mass completeness works well, provided that the galaxies above the mass-limit have similar or higher (mass/K-band flux) ratios than those on the mass limit (i.e., the mass-to-light ratio increases or is constant with mass).
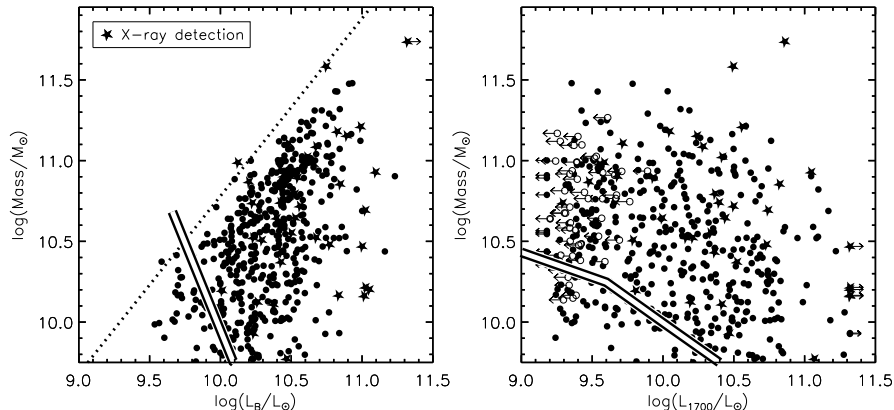
Figure 3.1 − Stellar mass against rest-frame *B*-band (*left*) and UV (*right*) luminosity. Stars represent sources that are detected in X-ray. The white line indicates where we become incomplete due to our *K*-band magnitude limit. Open circles with arrows represent upper limits at 1 σ of sources that are not detected in observed *B*-band, which corresponds with $\lambda = 1700$Å at the mean redshift of the sample. In the left panel there is a clear correlation between the mass and L_B, which indicates that selection in the rest-frame *B*-band is a good basis for a mass-selected sample. The absence of galaxies at the upper left side of the diagram means that, given a L_B-limited sample, we can always define a mass limit to which we are complete. This is illustrated by the dotted line, which traces the upper envelope of the data points and hence the lowest mass at which a source with a given *B*-band luminosity exists. A limit in *B*-band luminosity can, therefore, be directly translated into a limit in mass. Such a straightforward conversion is not possible using the rest-frame UV. In the right panel, there is no clear correlation between mass and L_{1700} and a notable lack of massive galaxies at bright UV-luminosities. Selecting in the rest-frame UV is therefore not a good basis for obtaining a mass-selected sample.

line, which has a slope of ∼1.1. No galaxies lie to the upper left of this line. Hence, if we wish to construct a mass-complete sample, we can use this line to calculate the limit in L_B to which we have to go. We can not rule out that no galaxies exist to the left of this line in other fields, but is likely that very few will. As we will see later, the galaxies close to this line are devoid of star formation and relatively old. Therefore, they logically have the maximum allowed M/L_B. The diagram clearly shows that selection in the rest-frame *B*-band can be used to construct a mass-selected sample. This is, of course, under the assumption that our SED-derived masses are correct (see Wuyts et al. (2009a) for detailed tests of SED-derived masses using simulations and radiative transfer).

The situation is strikingly different when looking at the right panel of Fig. 3.1, where mass is shown with respect to the rest-frame UV luminosity at 1700Å. Arrows denote 1 σ upper limits. At the depth of our data, there is no positive correlation between L_{UV} and mass. There is a lack of massive, UV-bright sources and, if anything, mass seems to decrease with increasing L_{1700}. As a consequence, there is no minimum value of L_{1700} for a given
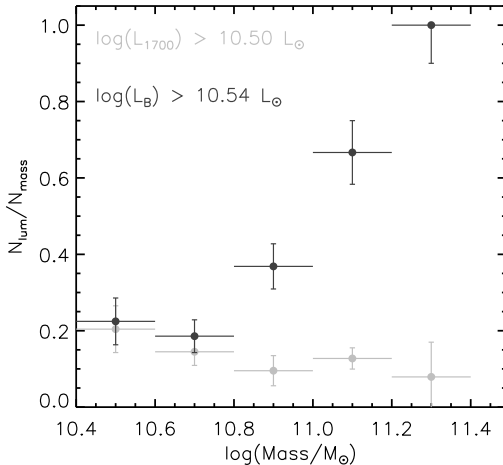
Figure 3.2 – The fraction of massive galaxies that is left when applying a rest-frame optical (*gray points*) and UV luminosity (*black points*) limit to a mass-selected sample. The error bars represent bootstrap errors. A UV-selected sample misses more and more galaxies going to higher masses, while an optically-selected sample recovers the mass-selected sample at the high-mass end.

mass that allows construction of a mass-selected sample in a straightforward way.

3.4.1 UV- and Optical Selection Limits

We next investigate the differences between UV-, optically, and mass-selected samples. We construct a mass-complete sample from our FIREWORKS sample by selecting all galaxies with masses greater than $3 \cdot 10^{10} M_\odot$. To investigate how a UV-selection changes the properties of a sample, we apply a UV-limit of $\log(L_{1700}) > 10.50 \, L_\odot$ to our mass-complete sample[5]. This leaves 124 (or 21%) sources out of the total of 569 sources with $M_* > 3 \cdot 10^{10} M_\odot$ between $1 < z < 2$. To see how optical selection affects sample properties, we apply a limit of $\log(L_B) > 10.54 \, L_\odot$, which renders a sample consisting of the same number of sources as the UV-selected sample. Figure 3.2 shows the fraction of galaxies that are left when using this UV-selected sample. Paradoxically, when applying a UV-limit of $\log(L_{1700}) > 10.50 \, L_\odot$ to our sample, an increasing fraction of sources is lost when going to higher masses (up to $\sim$92% for $\log(M_*) > 11 \, M_\odot$). In comparison, an optically-selected sample recovers the full mass-complete sample at $\log(M_*) > 11.2 \, M_\odot$.

Table 3.1 gives an overview of the derived properties of a UV-, an optically, and a mass-selected sample. UV-selected galaxies are, on average, larger, younger, and typically have higher SFRs than the mass-complete sample from which they are drawn. The mean values of the optically-selected sources lie between those of the UV- and mass-selected samples.

---

[5]See 3.6 for more information on the choice of this limit plus the effects of different UV-limits.

Table 3.1 – mean derived parameters

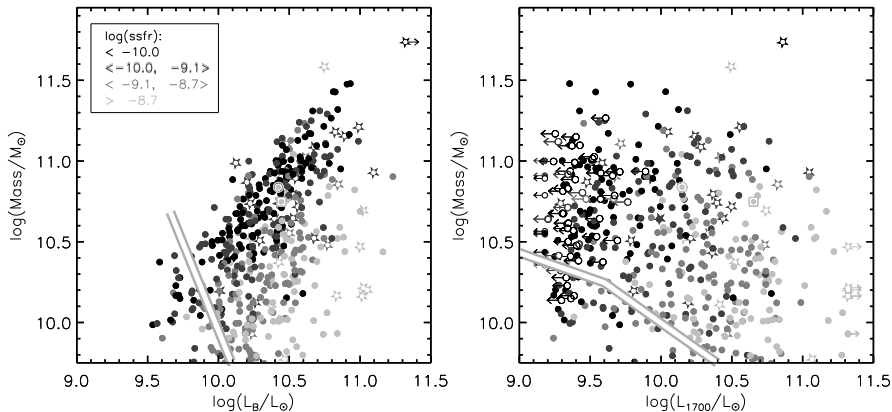| selected by	SFR $(M_\odot \mathrm{yr}^{-1})$	Age (Myr)	Mass $(M_\odot)$	sSFR (Gyr^{-1})	R_e (kpc)
Mass	38	1.6	10.8	0.66	3.1
Optical luminosity	52	1.4	11.0	0.83	4.0
UV luminosity	112	0.95	10.8	2.24	5.9

Figure 3.3 – Same as Fig. 3.1, now color-coded with respect to specific star formation rate (sSFR). The sSFR limits are the 25th, 50th, and 75th percentiles of the sSFR. *Left* — Lines of constant sSFR follow the trend between mass and rest-frame B-band luminosity. A cut in B-band luminosity would provide a sample with a wide range of sSFRs. Some passive galaxies would not be selected with respect to a mass-selected sample, and some highly starforming galaxies would be added. *Right* — Lines of constant sSFR lie almost vertical in the plane of the figure. The passive galaxies with the lowest sSFRs have the faintest UV luminosities. These will not be included in a L_{1700}-selected sample. We also see an intermediate population of sources with high sSFRs and intermediate UV luminosity ($L_{1700} \sim 10^{10} L_\odot$). These are starforming galaxies obscured by dust (see Fig. 3.4) that will not be selected when a limit of $\log(L_{1700}) = 10.5 \ L_\odot$ is used.

3.5 Correlations between Mass, Luminosity, Size, and Star Formation Rate

In this section we investigate in more detail how the average properties of a sample change when using different selection techniques. In Fig. 3.3, mass is shown against rest-frame luminosity and sources are color-coded as a function of sSFR, which increases from dark to light gray. In the left panel we show mass against L_B. We see that sources with the same sSFR follow a nearly linear trend between mass and L_B. On average, galaxies with the lowest sSFRs have the highest M/L_B and shape the envelope in the mass-luminosity diagram. These are the galaxies that effectively define the mass limit of the L_B-selected sample.
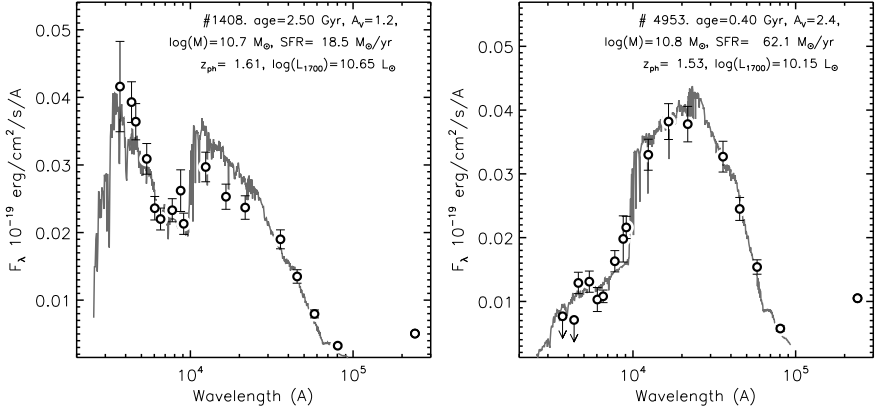
Figure 3.4 − Spectral energy distributions of star forming galaxies with high rest-frame UV flux (*left*) and with low rest-frame UV flux (*right*). The shape of the SED on the right is characteristic for galaxies that have high star formation rates, but intermediate UV luminosities. The UV luminosity is reduced due to the presence of dust in the galaxy.

The right panel shows mass against L_{1700}. Sources with similar sSFRs have similar rest-frame UV luminosities. The red, passive population lies at the lowest UV-luminosities and a higher L_{1700} corresponds to a higher sSFR. However, there are some intermediate sources that have a relatively low UV-luminosity and some of the highest sSFRs (massive blue sources around $\log(L_{1700}) = 10.2$ in Fig. 3.3). We show the spectral energy distribution of one of these sources (indicated with an open circle) in the right panel of Fig. 3.4. We compare it to the SED of a typical starforming galaxy (*left panel of Fig. 3.4*) with a high UV-luminosity (*the source around log(L_{1700}) = 10.6, indicated with an open square in Fig. 3.3*). The high SFR of the UV-faint source is caused by dusty star formation, whereas the source on the left is relatively unobscured. Some information on the dust content or a dust correction is evidently necessary to obtain a reliable sSFR estimate.

The right panel of Fig. 3.3 clearly shows that the galaxies with the lowest UV luminosities are the quiescent galaxies -those with the smallest specific star formation rates. It explains immediately why it is so hard to obtain a mass-selected sample from a UV-selected sample. Based on Bruzual & Charlot (2003) models, a simple stellar population with an age of 2 Gyr is ∼600 times fainter at 1700 Å than a galaxy of the same mass and age with constant star formation. The range in UV luminosity is tremendous.

We know that for a mass-selected sample, the sSFR is a decreasing function of mass in a particular redshift regime (Brinchmann et al. 2004; Elbaz et al. 2007; Noeske et al. 2007; Zheng et al. 2007; Patel et al. 2009; and Chapter 4 of this thesis). Figure 3.5 shows how this relation differs when an optically ($\log(L_B) > 10.54$ $L_{\odot}$) or a UV-selected sample ($\log(L_{1700})$ > 10.50
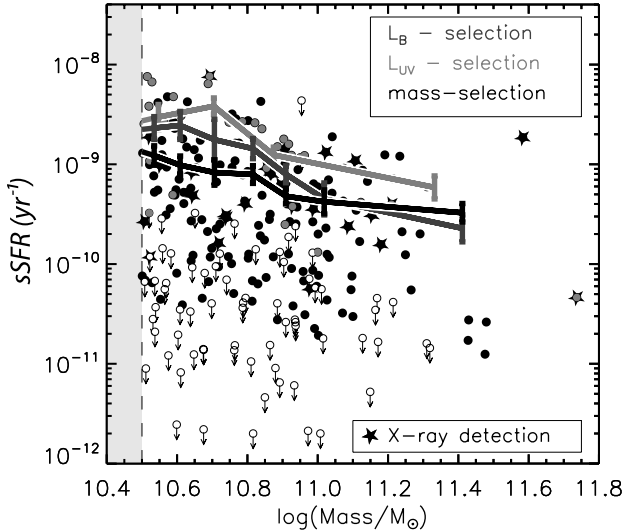
Figure 3.5 − The effect of luminosity cuts on the sSFR-mass-relation. In a mass-selected sample (*all points*), the mean sSFR decreases with mass (*black line*). A UV-selected sample (*light gray points*) does not contain the passive galaxies and its mean sSFR is therefore higher (*light gray line*). When applying a rest-frame *B*-band limit (*dark gray line*), the sSFR-mass relation is recovered at high masses. At the low-mass end, the passive galaxies are not selected and the mean sSFR is higher than for a mass-selected sample. Consequently, the slope of the sSFR-mass relation is much steeper for the optically selected sample than it is for the mass-limited sample. The stellar symbols represent sources that are detected in X-ray and are likely AGNs. If we remove these from the sample, the results do not change much.

$L_\odot$) is used. The light gray points and line denote the sSFRs of a UV-selected sample and its mean. It is higher than the mean mass-selected sSFR at all masses, by a factor of ~ 3 on average. The optically-selected sample (*dark gray line*) recovers the relation between sSFR and mass at the high-mass end but it does not select the passive, low-mass galaxies. This can also be deduced from Fig. 3.3. These results are not affected when X-ray detected sources are excluded.

Whereas the effects described above are simple to understand, as they are due to variations in SFR, more complex effects can arise from other correlations. Franx et al. (2008) found that the size of a galaxy is correlated with the mass and sSFR. Hence the mean size at a given mass will change with the selection band used. We illustrate this effect in Fig. 3.6, where we show mass versus luminosity labeled by size. The size in this diagram ($\hat{r}_e$) is normalized with respect to the size-mass relation of Shen et al. (2003). We define $\hat{r}_e = r_e / (M_*/\bar{M}_*)^{0.4}$, where $\bar{M}_* = 10^{10.8} M_\odot$, the mean mass of our sample. The trends are not as clear as for sSFR, but there are still some noticeable features.
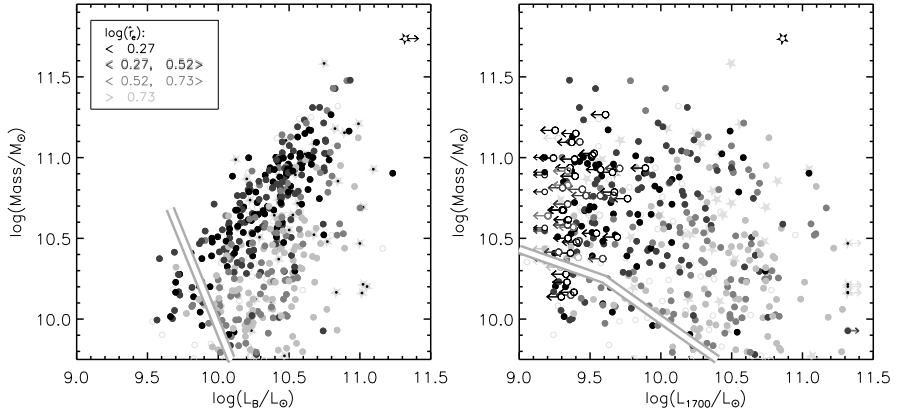
Figure 3.6 – Same as Fig. 3.1, now color-coded by size normalized to the size of similar mass galaxies today. The r_e-limits are the 25th, 50th, and 75th percentiles of the size. Open gray circles represent sources without a reliable size measurement. They take up 30% of the sample and almost all X-ray detections. *Left* — Size increases with decreasing M/L_B. Galaxies with small sizes lie along the ridge line, characteristic of red galaxies. A selection in L_B gives the full range in sizes, although it is incomplete with respect to compact galaxies. *Right* — In the mass-L_{1700}-diagram the galaxies with the smallest sizes typically have low rest-frame UV fluxes. They will not be selected in a UV-limited sample.

In the left panel we show mass versus L_B. It is striking that the size is smallest for the galaxies with the highest M/L, i.e. those who shape the upper left envelope in the diagram. The right panel shows mass against L_{1700}. The galaxies with the lowest sizes typically have the lowest UV-luminosities. It is interesting to see that, in addition to the size-mass relation (e.g., Trujillo et al. 2004; Williams et al. 2009), size also seems to be correlated with UV-luminosity.

In Fig. 3.7 we show how imposing a luminosity limit affects the size-mass relation. Figure 3.6 already showed that a luminosity-selected sample does not select the smallest galaxies. In Fig. 3.7 this is more clearly visible. The sizes of a UV-selected sample are on average ∼2 times larger than sizes of a mass-selected sample. The optical sample displays the same behavior at the low-mass end, where the mean size differs from the mean mass-selected size by a similar factor. At the high-mass end, the sizes of the optically and mass-selected sample overlap.

3.6   Summary and Discussion

Using the FIREWORKS catalog of the CDFS we investigate how luminosity selection affects the properties of a sample of galaxies at $1 < z < 2$. We find that the rest-frame B-band can adequately serve as a basis for a mass-selected sample, because of the relatively tight correlation between mass and
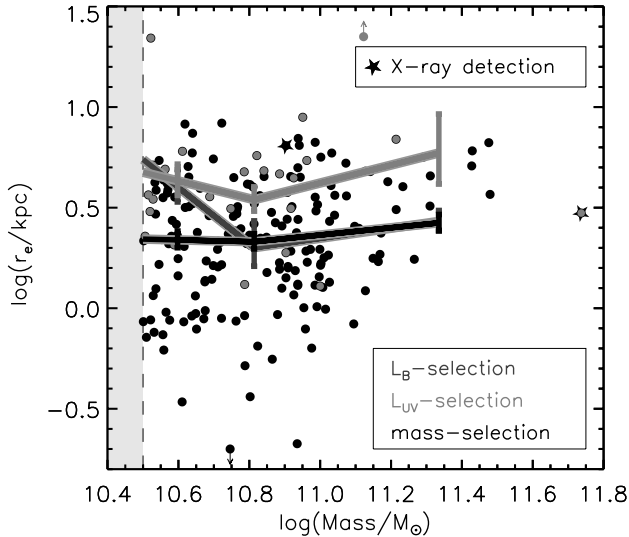
Figure 3.7 − The effect of luminosity cuts on the size-mass-relation. A UV-limited sample (*light gray points*) does not select the smallest galaxies (see also Fig. 3.6), its mean size (*light gray line*) hence lies above the mean size of a mass-selected sample (*black line*). The mean sizes of optically-selected sources (*dark gray line*) agree with the mass-selected sample for high-mass galaxies. At the low-mass end they are much higher than for the mass-selected sample.

L_B and the presence of an effective upper limit in M/L_B-ratio. The galaxies with the highest M/L_B-ratios are generally quiescent galaxies.

In contrast, when we select in L_{UV} (at 1700 Å), we find an inverse trend between L_{UV} and mass; the mass goes down with increasing L_{UV}. Constructing a mass-selected sample from a UV-limited sample is, therefore, not straightforward.

When an L_B-selection limit is applied, the resulting sample contains more blue sources than a mass-selected sample. As a consequence, an L_B-limited sample will contain a higher fraction of starforming sources. This results in a higher mean sSFR for an optically-selected sample with respect to a mass-selected sample, but only for low-mass galaxies. At the high-mass end, the mean sSFRs of the two samples agree. Therefore, the slope of the sSFR-mass relation is much steeper for the optically-selected sample than it is for the mass-limited sample. All this is to say that, even though L_B-selected samples can be converted into mass-selected samples, they can still lead to spurious correlations if the mass incompleteness at the faint-luminosity end is not properly accounted for.

A cut in UV luminosity will produce much stronger selection effects. Since the most passive galaxies typically have the lowest rest-frame UV luminosities, those galaxies will not be included in a UV-selected sample. The result

is that, overall, the average sSFR of such a sample is significantly higher (factor 2-5) than it is for a mass-selected sample.

As a result of these selection effects, one obtains the incorrect relation between sSFR and mass. The decline with mass is too strong for L_B-selected samples, and the overall value of the sSFR is too high for L_{UV}-selected samples.

In addition to the sSFR as a function of mass, other properties, less directly related to color, are affected too. We show the example of the sizes of galaxies as a function of mass. The smallest galaxies typically have the highest M/L_B-values and the faintest UV luminosities. When a optical selection limit is imposed, the mass-size-relation shifts to larger sizes than for a mass-selected sample, but only at the low-mass end. At high masses the two selection techniques agree. A UV-selected sample will not select the faint-L_{1700}, compact sources and its average size at a given mass will be ~ 2 times higher than for a mass-complete sample.

Finally, we examine different rest-frame luminosities to determine the lowest wavelength at which a sample can be selected without being susceptible to the selection effects that arise at 1700Å. In other words, we search for the wavelength at which we still observe an upper envelope in the mass-luminosity diagram. We find that the upper envelope arises around 2800Å. However, the upper limit shifts to fainter luminosities with decreasing wavelength. At near-UV wavelengths a deeper sample is necessary to reach the same mass-completeness limit as in the optical regime. For example, to obtain a sample that is complete at masses $M_* > 10^{11} M_\odot$ from an optically-selected sample, a depth of $L_B = 10.2 \ L_\odot$ is necessary. To reach the same completeness using a near-UV-selected sample at 2800Å, one needs a depth of $L_{2800} = 9.7 \ L_\odot$. Using samples that are selected at rest-frame wavelengths blueward of the rest-frame U-band is therefore possible, but it is not efficient.

The results presented here show clearly that galaxies need to be selected in a band red enough to lead to properly mass-selected samples. Obviously, at higher redshifts this means selecting at redder passbands. One of the interesting questions is how many dusty and quiescent galaxies exist at higher redshifts. It is possible that this fraction is negligible at $z \geq 4$ (see e.g., Bouwens et al. 2010, but also Mobasher et al. 2005, who state the opposite). The final determination will probably have to wait until the James Webb Space Telescope, which has very deep imaging capacity at 5 μm, sampling the rest-frame B-band to $z = 10$.

Appendix A - Additional Selection Limits

In Section 3.3 we showed that a UV-limited sample will select a lower fraction of galaxies when going to higher mass. It is interesting to see how this behavior changes with different UV-limits. In the left panel of Fig. A.1 we

show the same information as in Fig. 3.2 and include the mass fractions of samples selected by several other rest-frame UV limits.

These limits are not chosen at random, but reflect sample selection limits used in the literature. They roughly represent the observed R-band magnitude limits of Steidel et al. (1996, 1999), Adelberger et al. (2004), and Davis et al. (2003) used to select objects at $z \sim 3$, $1.4 < z < 2.5$, and $z < 1.4$, respectively. We also include the B-band limit used by Lilly et al. (2007) for objects between $1.4 < z < 2.5$. To see how these selections would affect our mass-selected sample, we translate the observed luminosity limits into rest-frame UV limits at wavelengths appropriate for their redshift regime. We caution the reader that these are rough indications to illustrate the effect of different UV-luminosity limits on our mass-limited sample.

It is difficult to determine a single rest-frame limit at a specific UV wavelength for each selection limit, due to the wide range in redshifts targeted. Therefore, we also investigate the effect of selection directly in the observed bands. To do this we adapted the redshift range of our mass-selected sample to the regimes targeted by the observed B- and R-band-selected samples used above. For each redshift subsample we redetermine the completeness limits and determine the fraction of sources with respect to a mass-limited sample. The results are shown in the right panel of Fig. A.1 and are substantially different from those of the left panel. To discuss in detail the cause of those differences would be beyond the aim of this chapter. These figures serve as a rough indication of the effects of different luminosity limits only.

For completeness, we show in Figure A.2 how different UV-limits affect the sSFR-mass and size-mass relation. As expected, the difference between a mass-selected and a UV-selected sample becomes smaller when applying a lower limit, and greater when a higher UV-limit is used.
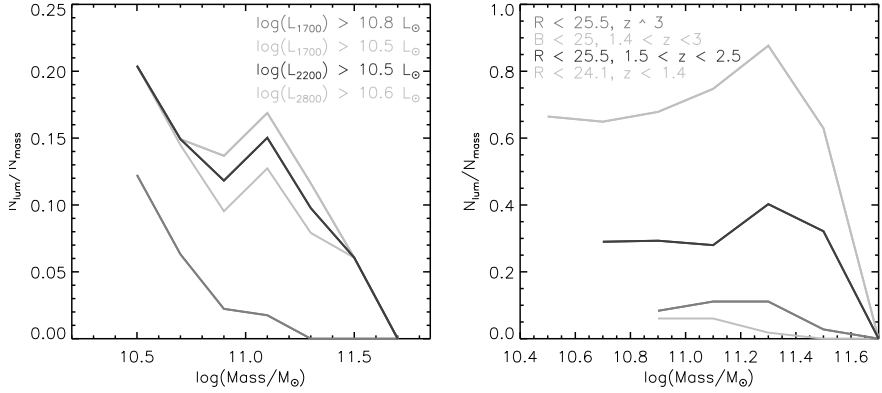
Figure A.1 − The fraction of massive galaxies left in a luminosity-selected sample with respect to a mass-selected sample, for different rest-frame UV-limits (*left*) and different observed limits in the *R*- and *B*-band (*right*). See text for more details.
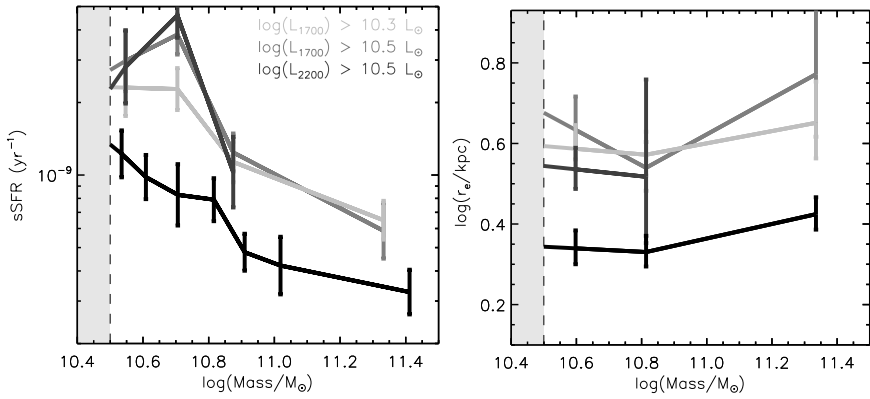
Figure A.2 − Mean sSFR (*left*) and mean size (*right*) against mass for different selection limits. The black line represents the mass limit, the other lines represent UV-selected samples at $\log(L_{1700}) = 10.3, 10.5$, and $\log(L_{2200}) = 10.5 L_{\odot}$, respectively. As can be expected, imposing a higher UV-limit on the sample makes the difference between the UV- and mass-selected sample bigger, while a lower limit makes it smaller. When applying the high UV-limit of $\log(L_{2200}) = 10.5 L_{\odot}$ to the sample of trustworthy sizes, (which contains fewer sources than the complete mass-limited sample, see caption Fig. 3.6), very few sources remain in the sample. Therefore, the lower UV-selected line in the right panel is not reliable.

References

Adelberger, K. L., Steidel, C. C., Shapley, A. E., Hunt, M. P., Erb, D. K., Reddy, N. A., Pettini, M. 2004, ApJ, 607, 226A

Brammer, G. B., van Dokkum, P. G., Coppi, P. 2008, ApJ, 686, 1503

Brinchmann, J., et al. 2004 MNRAS351, 1151

Bruzual, G., & Charlot, S. 2003, MNRAS, 2, 344, 1000

Bouwens, R. J., et al. 2010, ApJ, 709, 133

owie, L. L., Songaila, A., Hu, E. M., Cohen, J. G. 1996, AJ, 112, 839

Daddi, E., Cimatti, A., Renzini, A., Fontana, A., Mignoli, M., Pozzetti, L., Tozzi, P., Zamorani, G. 2004, ApJ, 617, 746

Dale, D. A. & Helou, G. 2002, ApJ, 576, 159

Davis, M. et al. 2003, in Guhathakurta P., ed., SPIEConf. Ser.Vol. 4834, Discoveries and Research Prospects from 6- to 10-Meter-Class Telescopes II. SPIE, Bellingham, p. 161

Dunlop, J. S., Guiderdoni, B., Rocca-Volmerange, B., Peacock, J. A., Longair, M. S. 1989, MNRAS, 240, 257

Elbaz et al. 2007, A&A, 468, 33

Franx, M., et al. 2003, ApJ, 587, 79

Franx, M., van Dokkum, P. G., Förster Schreiber, N. M., Wuyts, S., Labbé, I., Toft, S. 2008, ApJ, 688, 770

Giacconi, R., et al. 2002 ApJS, 139, 369

Glazebrook, K., Peacock., J. A., Miller, L., Collins, C. A. 1995, MNRAS, 275, 169

Holden, B. P., et al. 2007 ApJ, 670,190

Mobasher, B., et al. 2005, ApJ, 635, 832

Kroupa, P. 2001, MNRAS, 322, 231

Labbé, I. 2004, PhD Thesis

Noeske, K. G., et al. 2007, ApJ, 660, 47

Patel, S. G., Holden, B. P., Kelson, D. D., Illingworth, G. D., Franx, M. 2009, ApJ, 705, 67

Peng, C. Y., Ho, L. C., Impey, C. D., & Rix, H.-W. 2002, AJ, 124, 266

Quadri, R., et al. 2007, AJ, 134, 1103

Reddy, N., Steidel, C. C. 2009, ApJ, 692, 778

Rudnick, G., et al. 2003, ApJ, 599, 847

Shen, S., Mo, H. J., White, S. D. M., Blanton, M. R., Kauffmann, G., Voges, W., Brinkmann, J., Csabai, I. 2003, MNRAS, 343, 978

Steidel, C. C., Giavalisco, M., Dickinson, M., Adelberger, K, L. 1996 AJ, 112, 352

Steidel, C. C., et al. 1999 ApJ, 519, 1

Tasca, L. A. M., et al. 2009, A&A, 503, 379

Taylor, E. N., et al. 2009, ApJS, 139, 369

Toft, S., et al. 2007, ApJ, 671, 285

Trujillo, I., et al. 2004, ApJ, 604, 521

Trujillo, I., et al. 2006, ApJ, 650, 18

van Dokkum, P. G., et al. 2006, ApJ, 638, L59

Williams, R. J., Quadri, R. F., Franx, M., van Dokkum, P., Toft, S., Kriek, M., Labbé, I. 2009, preprint (astro-ph/0906.4786)

Wuyts, S., Labbé, I., Förster-Schreiber, N., M., Franx, M., Rudnick, G., Brammer, G., B., van Dokkum, P. G 2008, ApJ, 682, 985

Wuyts, S., van Dokkum, P. G., Franx, M., Förster Schreiber, N. M., Illingworth,

G. D., Labbé, I., Rudnick, G. 2009, ApJ, 706, 885

Wuyts, S. et al. 2009 ApJ, 700, 799

Wuyts, S., Franx, M., Cox, T. J., Hernquist, L., Hopkins, P. F., Robertson, B. E., van Dokkum, P. G. 2009, ApJ, 696, 348

Zheng, X. Z., Bell, E. F., Papovich, C., Wolf, C., Meisenheimer, K., Rix, H.-W., Rieke, G. H., Somerville, R. 2007, ApJ, 661, 41

4

Evolution of the Specific Star Formation Rate

We study the evolution of the star formation rate (SFR) of mid-infrared
(IR) selected galaxies in the extended Chandra Deep Field South (E-
CDFS). We use a combination of $U - K$ GaBoDS and MUSYC data,
deep IRAC observations from SIMPLE, and deep MIPS data from
FIDEL. This unique multi-wavelength data set allows us to investi-
gate the SFR history of massive galaxies out to redshift $z \sim 1.8$. We
determine star formation rates using both the rest-frame ultraviolet
luminosity from young, hot stars and the total IR luminosity of ob-
scured star formation obtained from the MIPS $24\,\mu$m flux. We find
that at all redshifts the galaxies with higher masses have substantially
lower specific star formation rates than lower mass galaxies. The av-
erage specific star formation rates increase with redshift, and the rate
of incline is similar for all galaxies (roughly $(1 + z)^n, n = 4.5$). It does
not seem to be a strong function of galaxy mass. Using a subsample
of galaxies with masses $M_* > 10^{11}M_\odot$, we measured the fraction of
galaxies whose star formation is quenched. We consider a galaxy to
be in quiescent mode when its specific star formation rate does not
exceed $1/(3 \times t_H)$, where t_H is the Hubble time. The fraction of qui-
escent galaxies defined as such decreases with redshift out to $z \sim 1.8$.
We find that, at that redshift, $30 \pm 7\%$ of the $M_* > 10^{11}M_\odot$ sources
would be considered quiescent according to our criterion.

Maaike Damen, Ivo Labbé, Marijn Franx, Pieter G. van Dokkum,
Edward N. Taylor, Eric J. Gawiser

4.1   Introduction

T HE star formation history of massive galaxies is not well understood. Standard galaxy formation models have difficulty reproducing today's red and dead galaxies, unless mechanisms are introduced that prevent the gas from cooling and forming stars. To better constrain the models, it is useful to determine the star formation rates (SFRs) of galaxies as a function of mass and redshift. This has been done out to redshift $z = 1$, using the COMBO-17 survey (Zheng et al. 2007).

A surprising result of their study was that the specific star formation rates (SFR per unit stellar mass, sSFR) of high mass galaxies evolve at the same rate as those of low mass galaxies, where the most massive galaxies are offset to lower sSFRs. At higher redshifts, studies of star formation have so far focused mainly on either specific galaxy populations or specific redshift regimes (e.g., Lyman break galaxies, (Steidel et al. 1996, 1999), distant red galaxies, (Papovich et al. 2006)). Papovich et al. (2006) found that massive, red galaxies at $1.5 \leq z \leq 3$ have sSFRs that are comparable to the global value integrated over all galaxies. Given the fact that we can already see the Hubble sequence in place at $z \sim 1$, this means that the period between $1 \lesssim z \lesssim 2.5$ is an interesting stage of transition, where massive galaxies evolve from actively star forming systems to the passive galaxies we observe in the local universe. The connection between the high and low redshift galaxy populations is not yet clear.

In this chapter, we investigate the star formation history of massive galaxies ($M_* > 10^{11} M_\odot$), through measurements of the specific star formation rate from $z \sim 0.2$ to $z \sim 1.8$. For this analysis we use the SIMPLE survey and ancillary data ranging from the near-ultraviolet (near-UV) to the mid-infrared (MIR).

Throughout this chapter we assume a ΛCDM cosmology with $\Omega_m = 0.3$, $\Omega_\Lambda = 0.7$, and $H_0 = 70$ km s^{-1} Mpc^{-1}. All magnitudes are given in the AB photometric system. We denote magnitudes from the four *Spitzer* IRAC channels as [3.6 μm], [4.5 μm], [5.8 μm], and [8.0 μm], respectively. Stellar masses are determined assuming a Kroupa (2001) initial mass function (IMF).

4.2   Data

4.2.1   Observations and Sample Selection

We have combined imaging from the near-UV to MIR. The IR imaging was primarily taken from the SIMPLE survey (*Spitzer*'s IRAC and MUSYC Public Legacy of the Extended CDFS). This survey consists of deep observations with the Infrared Array Camera (IRAC; Fazio et al. 2004) covering the 0.5 × 0.5 deg area centered on the Chandra Deep Field South (CDFS) in wavelength bands 3.6 μm, 4.5 μm, 5.8 μm , and 8.0 μm. The SIMPLE IRAC

observations are supplemented with the IRAC images from the Great Observatories Origins Deep Survey (GOODS; Dickinson et al. (in prep.)). These very deep images were taken on the central $\sim$160 arcmin^2 of the field. The combined mosaics are publicly available from the *Spitzer* Science Center[1]. A detailed description of the observations and data reduction is given in Chapter 2.

For coverage of the optical/near-infrared (NIR) wavelengths, we used ground-based data from different sources. To cover the UV to optical regime, we used the UBVRI imaging from the COMBO-17 and ESO DPS surveys (Wolf et al. 2004 and Arnouts et al. 2001, respectively) in the re-reduced version of the GaBoDS consortium (Erben et al. 2005, Hildebrandt et al. 2006). We obtained $z'JHK$ images from the Multiwavelength Survey by Yale-Chile (MUSYC, Gawiser et al. 2006), which are available online[2]. The final $UBVRIz'JHK$ images we used were position-matched by Taylor et al. (2009). We also include the MIR 24 μm MIPS image from the Far-Infrared Deep Extragalactic Legacy Survey (FIDEL; PI M. Dickinson).

Sources were detected and extracted using the SExtractor software (Bertin & Arnouts 1996) on a detection image, which is an inverse-variance weighted average of the most sensitive IRAC bands, 3.6 and 4.5 μm. The images were convolved with a Gaussian to match the 8.0 μm image, which has the broadest FWHM ($\sim$2$''$). Using an aperture diameter of 4$''$, we detected $\sim$61,000 galaxies to a limiting depth of $([3.6\mu\text{m}] + [4.5\mu\text{m}])/2 < 24.0$ (24.3 for the GOODS area).

By selecting all sources with $([3.6\mu\text{m}] + [4.5\mu\text{m}])/2 < 21.2$, we created a subsample of 3948 sources, 95% of which have $S/N > 5$ in K. From this subsample we excluded all X-ray detected sources as they are highly likely active galactic nuclei (AGN; Alexander et al. 2003 and Virani et al. 2006). Stars were identified using the color criterion $J - K < 0.04$ and removed from the sample. The final sample contains 3391 sources out to $z = 2$. From this sample, 60% of the sources are detected in MIPS ($S/N > 10$). At $z \sim 1.8$, our highest redshift bin, 83% of the sources are detected in MIPS. Such high detection rates are consistent with earlier results (Daddi et al. 2005, Papovich et al. 2006). Since we interpret 24 μm flux directly as star formation activity (rather than evidence of AGN activity), the high fraction of MIPS detected sources contributes greatly to our conclusions regarding the star formation history (see sections 4.3.1 and 4.5).

The MIPS fluxes in particular were treated for blending. We used the IRAC 3.6 μm image, which has a smaller PSF to subtract modeled sources from MIPS sources that showed close neighbors, thus deblending the image (see Labbé et al. (2004, 2006) and also Chapter 2 for more information on this technique). For the IRAC images themselves, which also suffer from blending,

---

[1]http://data.spitzer.caltech.edu/popular/simple
[2]http://www.astro.yale.edu/MUSYC

this method could not be applied since the K-band image we would like to use for this is not deep enough for this kind of modeling. We compared our final MIPS fluxes with the deeper observations of the GOODS team as a check and found that at the faint end, our fluxes were slightly larger. This could be an effect of remaining blending issues and we investigate this further and see how it affects our results in section 4.5.

4.2.2   Spectroscopic and Photometric Redshifts

The E-CDFS has been intensely targeted for observations the last few years and, as a result, many spectroscopic redshifts are available for our sample. We collected 438 spectroscopic redshifts from large surveys by Cimatti et al. (2002), le Fèvre et al. (2004), Vanzella et al. (2008), and Ravikumar et al. (2007), which accounts for 13% of our sample. In addition, we included photometric redshifts from the COMBO-17 survey out to $z = 0.7$ Wolf et al. (2004). For the remainder of the sources we used the new photometric redshift code EAZY (Brammer et al. 2008) to obtain redshifts.

We measure the scatter by determining the median absolute deviation of $|dz| = 0.025$ where $dz = (z_{spec} - z_{phot})/(1 + z_{spec})$. For $z \geq 1$, which is the regime we are specifically interested in, this value is somewhat higher: $|dz| = 0.055$.

In Section 4.4 we will inspect the fraction of quiescent galaxies. Uncertain photometric redshifts can affect this fraction and it is, therefore, important to verify that for the quiescent galaxies the photometric redshifts are not dramatically offset. We find that their photometric redshifts do not lie among the most extreme outliers and their median absolute deviation is $|dz| = 0.024$ (0.050 at $z \geq 1$), which is smaller than for the complete sample.

4.2.3   Low-Redshift Sample

We include data from the Sloan Digital Sky Survey (SDSS) to check whether we are consistent with the local universe. SDSS masses were determined by Kauffmann et al. (2003) using spectra. Brinchmann et al. (2004) derived SFRs from emission lines. For details on the derivation of the masses and SFRs in the SDSS we refer to their papers.

4.3   Star Formation Rates, Mass and Completeness

4.3.1   Inferring the SFRs from the 24 μm Flux and UV Luminosity

We estimated SFRs using the UV and IR emission of the sample galaxies. The UV flux probes the unobscured light from young stars, whereas the IR flux measures obscured star formation through light that has been re-processed by dust. Combined they give a complete census of the bolometric luminosity of young stars in the galaxy (Gordon et al. 2000; Bell 2003).

At the redshifts of interest ($z \sim 0.2 - 1.8$), MIPS 24 μm probes rest-frame 8-15 μm, which broadly correlates with the total IR luminosity ($L_{IR} = L(8 - 1000\mu m)$). We use IR template spectral energy distributions (SEDs) of star forming galaxies of Dale & Helou (2002) to translate the observed 24 μm flux to L_{IR}. First, we convert the observed 24 μm flux density to a rest-frame luminosity density at $24/(1 + z)\,\mu$m, then we extrapolate this value to a total IR luminosity using the template SEDs. The model spectra cover a wide range of spectral shapes, allowing for different heating levels of the interstellar environment. Following Wuyts et al. (2008) we adopt the mean of $\log(L_{IR})$ derived from the templates ranging from quiescent to active galaxies as the best estimate for the the total IR luminosity. To convert the UV and IR luminosities to a SFR, we use the calibration from Bell et al. (2005), which is in accordance with Papovich et al. (2006), using a Kroupa IMF:

$$\Psi/M_\odot \text{ yr}^{-1} = 1.09 \times 10^{-10} \times (L_{IR} + 3.3\ L_{2800})/L_\odot, \qquad (4.1)$$

where $L_{2800} = \nu L_{\nu,(2800\text{\r{A}})}$ is the luminosity at rest-frame 2800 Å, a rough estimate of the total integrated UV luminosity (1216-3000Å). The scatter in the conversion to L_{IR} induces a systematic error of typically 0.3 dex (Bell et al. 2005, Papovich et al. 2006). Another source of error is the uncertainty in photometric redshifts, as small changes in redshift can have a significant effect to the conversion. Applying the 68% confidence values of the photometric redshifts induces variations in the inferred L_{IR} of 0.1 dex.

There are some additional sources of error that are harder to quantify. Firstly there is the assumption that local IR SEDs represent the high-redshift galaxy population accurately. The reliability of this assumption has been investigated by Adelberger et al. (2000), who found that the bulk of intermediate to high-redshift galaxies have IR SEDs similar to galaxies in the local universe. However, the physical grounds for this are still unknown. Secondly, an AGN would also contribute to the 24 μm emission. Although we removed all X-ray detections from our sample, dust-obscured AGN could still be present and some SFRs may in fact be upper limits.

4.3.2 Stellar Mass and Rest-Frame Colors

We fitted the UV-to-8 μm SEDs of the galaxies using the evolutionary synthesis code developed by Bruzual & Charlot (2003) to obtain stellar masses for our sample. We assumed solar metallicity, a Salpeter IMF and a Calzetti reddening law. We used the publicly available HYPERZ stellar population fitting code (Bolzonella et al. 2000) and let it choose from three star formation histories: a single stellar population (SSP) without dust, a constant star formation (CSF) history and an exponentially declining star formation history with a characteristic timescale of 300 Myr (τ300), the latter two with
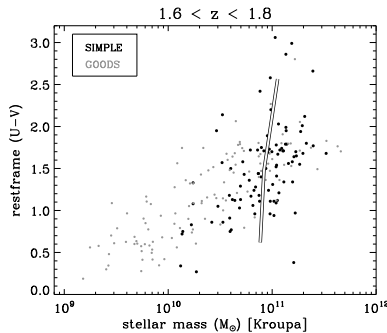
Figure 4.1 – Mass completeness: Rest-frame U-V color versus stellar mass for $1.6 < z < 1.8$. Our sample is shown in black dots. The white line is determined by scaling the detected sources down to the SIMPLE detection limit. It shows the minimal mass for 90% of these scaled down sources, which means that out to $z \sim 1.8$, we are complete for galaxies with $M_* > 10^{11} M_\odot$. Gray points refer to the deeper GOODS data, added to illustrate the incompleteness at the low-mass end.

varying amounts of dust. To facilitate comparison with other studies, the derived masses were subsequently converted to a Kroupa IMF by subtracting a factor of 0.2 dex. We calculated rest-frame luminosities and colors by interpolating between observed bands using the best-fit templates as a guide (see Rudnick et al. (2003) and Taylor et al. (2009) for a detailed description of this approach).

4.3.3   Mass Completeness

To determine the mass limit to which we are complete, we take detected sources with $1.6 < z < 1.8$ and scale them down in mass to the flux detection limit ($(([3.6\mu m] + [4.5\mu m])/2 = 21.2)$. This is illustrated in Fig. 4.1 where rest-frame U-V colors are plotted against mass. The white line is the mass limit to which we can detect 90% of the scaled sources. The black dots in this figure represent sources in our sample. Sources from the significantly deeper GOODS-ISAAC catalog (Wuyts et al. 2008) are overplotted in gray to illustrate the effect of incompleteness. We can conclude that we are 90% complete for $M_* > 10^{11} M_\odot$ in the highest redshift bin ($1.6 < z < 1.8$).

4.4   Star Formation Rates as a Function of Redshift

We determine the average SFR in different mass bins to examine the evolution of specific SFR with redshift out to $z \sim 1.8$. The average is based on the SFRs determined from the UV and MIPS fluxes, as described in section 4.3.1. Sources with no significant MIPS flux were also included in the average.

Figure 4.2 shows the redshift evolution of the average sSFR in different mass bins (filled circles), the mean sSFRs are also listed in Table 4.1 Dots show where we suffer from incompleteness, the error bars represent the bootstrapped 68% confidence levels on the measurement of the mean sSFR. The sSFRs of more massive galaxies are typically lower than those of less massive galaxies over the whole redshift range.

In addition, Fig. 4.2 shows that the sSFR increases with redshift for all

Table 4.1 − specific star formation rates in mass and redshift bins

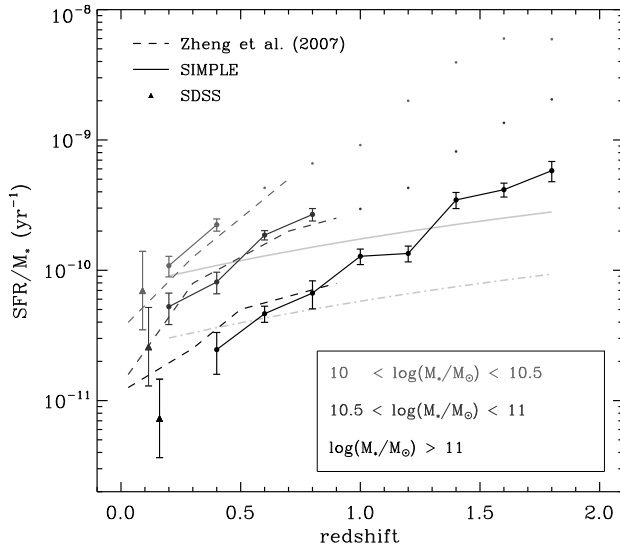| z	sSFR (10^{-9} yr^{-1})		
	$10. < \log(M_*/M_\odot)< 10.5$	$10.5 <\log(M_*/M_\odot)< 11.$	$\log(M_*/M_\odot)> 11.$
0.2	0.11 ± 0.02	0.051 ± 0.013	$--$
0.4	0.22 ± 0.03	0.078 ± 0.013	0.025 ± 0.009
0.6	$--$	0.18 ± 0.02	0.046 ± 0.006
0.8	$--$	0.26 ± 0.03	0.063 ± 0.014
1.0	$--$	$--$	0.12 ± 0.02
1.2	$--$	$--$	0.13 ± 0.02
1.4	$--$	$--$	0.34 ± 0.05
1.6	$--$	$--$	0.41 ± 0.05
1.8	$--$	$--$	0.57 ± 0.10

Figure 4.2 − Specific star formation rate versus redshift in different mass bins. Filled circles are SIMPLE results, dots show where we become incomplete with respect to mass. Triangles denote SDSS data. The error bars represent bootstrap errors for SIMPLE and a systematic error of 0.3 dex for the SDSS data. The dashed lines represent the results from Zheng et al. (2007) in identical mass bins. The gray solid line is the inverse of the Hubble time ($1/t_H$ in yr^{-1}). Sources above this line are in a starburst mode: the time they needed for their stars to form is shorter than the Hubble time. Star formation is quenched in galaxies under the gray dashed line ($1/(3 \times t_H)$); the bulk of their stars has already been formed. The sSFR increases with redshift at a rate that appears independent of mass and sSFRs of more massive galaxies are typically lower than those of less massive galaxies over the whole redshift range. These results both confirm and expand the findings of Zheng et al. (2007).
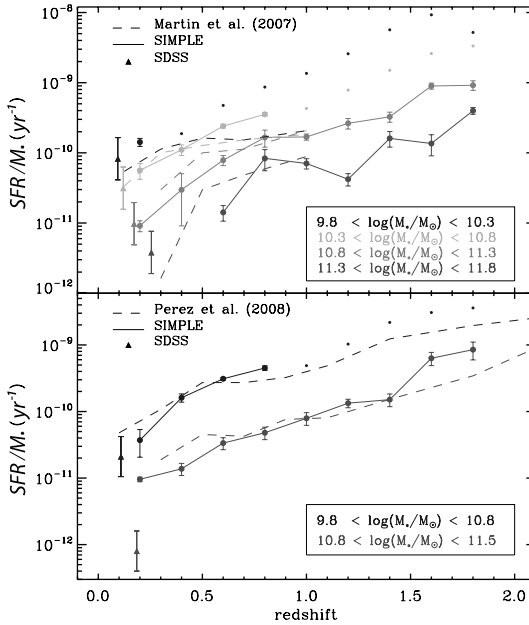
Figure 4.3 – Same as Fig. 4.2, now compared with results from Martin et al. (2007) (upper panel) and Perez-Gonzalez et al. (2008) (lower panel). The mass bins differ from those in Fig. 4.2 and were determined by subtracting a factor of 0.2 dex from the mass bins the quoted authors use, to correct for the difference in IMF. sSFR values in the lower panel are calculated using the median, following Perez-Gonzalez et al. (2008).

mass bins and that the slope $(dlog(sSFR)/dz)$ does not seem to be a strong function of mass (see also Chapter 5). To quantify this, we fitted the sSFR with $(1 + z)^n$ over the redshift range where we are complete with respect to mass. The value of the slope n is 5.1±0.6 and 4.6±0.3 for galaxies with masses $10.5 < log(M/M_\odot) \le 11$ and $log(M/M_\odot) > 11$, respectively. These numbers are consistent within 1 σ with results based on the FIREWORKS catalog over the same redshift range (3.6±0.3 ($z < 0.8$), and 4.8±0.4 ($z < 1.8$), for both mass bins, respectively; Chapter 5 of this thesis).

The trends in sSFR we find for each mass bin are consistent with local values from SDSS data, represented in Fig. 4.2 with triangles. We account for the difference in SFR derivation by applying a systematic error of 0.3 dex (J. Brinchmann, private communication).

Our results directly expand and confirm the findings of Zheng et al. (2007), who carried out a similar study based on a R-band selected sample in the E-CDFS and Abell 901/902. Their results are included in Fig. 4.2 as dashed lines. For galaxies with $M_* > 10^{11} M_\odot$ we can extend the trend in sSFR they find to $z \sim 1.8$. At $z < 0.6$ the results diverge because of the low number (7) of sources in that specific bin.

In Fig. 4.3 we compare our results with other studies in similar fields: a study by Martin et al. (2007) (E-CDFS; upper panel) and by Pérez-Gonzáles et al. (2008) (CDFS, Hubble Deep Field North and the Lockman Hole Field; lower panel). We converted the mass intervals of both studies to our choice of IMF and recalculated our mean sSFRs appropriate for these mass intervals.

Our data broadly agree with the results of Martin et al. (2007), especially in the intermediate mass bin ($10^{10.8} < M_*/M_\odot < 10^{11.3}$). However, there are discrepancies at the high-mass end, where the evolution of the sSFR with redshift they find is stronger than what we find, and at the low-mass end, where it appears to be weaker. As a result, Martin et al. (2007) do see a mass-dependence in the evolution of the sSFR. The reason for these differences is not immediately clear, particularly given the fact that both studies use the same field. We note, however, that Martin et al. (2007) use a different method for determining star formation rates: they derive SFRs from the UV and correct for extinction using MIPS. Furthermore, the difference at the high mass end may be caused by the poor number statistics in the highest mass bin ($M_* > 10^{11} M_\odot$). The number of galaxies in this mass bin is 4, 3, and 6 for redshifts $z \sim 0.6, 0.8$, and 1.0, respectively, which is probably comparable to their sample. Hence the significance of the difference at these masses is small and no strong statement about the evolution is possible.

Pérez-González et al. (2008) use an IRAC selected sample and their SFRs are determined using a combination of rest-frame UV and MIPS 24 μm flux, similar to what we do. The lower panel of Fig. 4.3 shows their results, which are based on the median of the sSFR in each mass and redshift bin. The agreement out to $z \sim 1.4$ is good, beyond that, our median values are somewhat larger. Since the results come from different fields, it could be that field-to-field variation plays a role. Note that we use the mean SFR, rather than the median, in our main analysis, in contrast to Pérez-Gonzáles (2008). In our sample the mean SFR is on average a factor of 1.8 higher than the median.

Also shown in Fig. 4.2 is the inverse of the Hubble time (t_H, gray solid line). Sources above this line are forming stars rapidly: the time they needed for their stars to form is shorter than the Hubble time. Sources below the line have had a declining SFR. Massive galaxies ($M_* > 10^{11} M_\odot$) have on average a specific star formation rate of $\sim 2 \times 10^{-10} \text{yr}^{-1}$ at $z \sim 1.1$, which is consistent with having a constant SFR over $z = \infty$ to $z \sim 1.1$.

Even though the average sSFR increases rapidly with redshift, the spread in sSFR is very high at all redshifts, with a peak at very low sSFRs. This is explicitly shown in Fig. 4.4 which contains histograms of the sSFR of the most massive galaxies ($M_* > 10^{11} M_\odot$) in three different redshift bins. The arrows point at the average value of the sSFR in each redshift bin. To characterize this low sSFR peak, we define quiescent galaxies with the criterion $sSFR < 1/(3 \times t_H)$. These galaxies must have had strong quenching of their star formation. This criterion is represented in Fig. 4.2 by the dashed gray line. In Fig. 4.4 the dashed histograms represent sources that obey this criterion.

Figure 4.5 shows the evolution of the fraction of quiescent galaxies thus defined with time. The upper panel shows a histogram of all galaxies with $M_* > 10^{11}$ and those that have sSFR smaller than $1/(3 \times t_H)$ yr^{-1} are
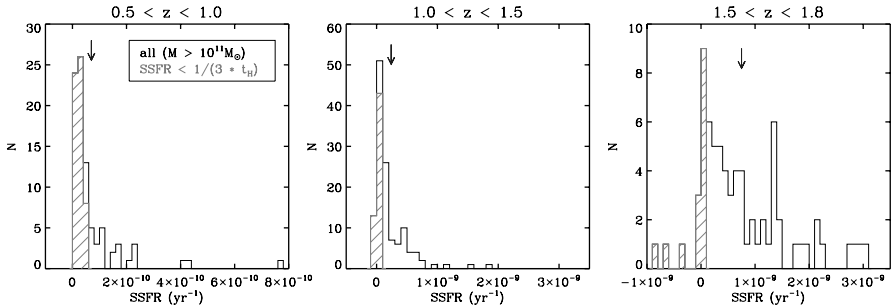
Figure 4.4 – The distribution of the sSFR for galaxies with $M_* > 10^{11} M_\odot$ in three redshift bins: left: $0.5 < z < 1.0$, middle: $1.0 < z < 1.5$, right: $1.5 < z < 1.8$. In all three redshift regimes the distribution is quite wide and peaks at low sSFRs. Arrows point to the average value of the sSFR in each redshift bin.

overplotted using dashes. The lower panel shows the fraction of galaxies with quenched star formation as a function of redshift. SDSS data have been used to determine a local value (triangle). The error bars are again bootstrap errors. The fraction of quiescent galaxies decreases monotonically with redshift from the local universe out to $z \sim 1.8$, with the exception of $z \sim 0.5$. The fraction of passive galaxies in our lowest redshift bin seems inconsistent with this trend, which could be due to the low number of galaxies at this redshift.

Another thing to note is the elevated number of galaxies in the $z \sim 0.7$ bin, which shows a slightly higher quiescent fraction than its neighboring bins. This is probably due to overdensities known to exist at this redshift in the E-CDFS (Gilli et al. 2003, Wolf et al. 2004). Such overdensities may harbor more passive galaxies, which can account for the high quiescent fraction. The same effect can be seen in Fig. 9 of Kaviraj et al. (2008). This figure shows the evolution of recent star formation with redshift based on UV to optical colors. At $z \sim 0.7 - 0.75$ there is less star formation than in the neighboring redshift bins, which agrees with what we find.

The main point to take from Fig. 4.5 is that we can still see massive quiescent galaxies out to $z \sim 1.8$, where they make up $30 \pm 7\%$ of all massive galaxies.

4.5   Conclusions

We investigate the star formation history of massive galaxies out to redshift $z \sim 1.8$, by analyzing specific star formation rates (sSFRs) of a sample of $\sim 3,400$ sources from SIMPLE, a survey that combines new *Spitzer*/IRAC observations of the E-CDFS with ancillary data ranging from the near-UV to the MIR. We find quiescent galaxies with masses higher than $10^{11} M_\odot$ out to the highest redshift probed, $z \sim 1.8$. At this redshift, they form
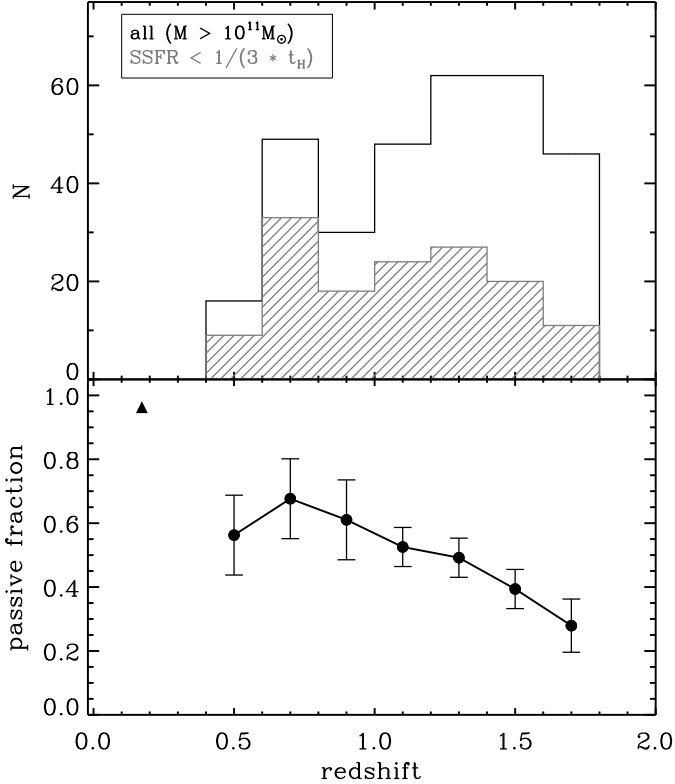
Figure 4.5 – Overview of the fraction of quiescent galaxies in the highest mass bin ($M_* > 10^{11} M_\odot$), for which we are complete out to $z \sim 1.8$. Quiescent galaxies are defined as sources with sSFR $< 1/(3 \times t_H) \, \mathrm{yr}^{-1}$, where t_H is the age of the universe at a given redshift. The upper panel shows a histogram of all galaxies in this mass range. Overplotted is the number of galaxies whose star formation is quenched (*dashed area*). The lower panel shows the fraction of galaxies in quiescent mode, determined from the histogram values. The error bars represent bootstrap errors. SDSS data have been used to determine a local value (triangle).

$30 \pm 7\%$ of the total number of massive galaxies. The sSFR is an increasing function with redshift (roughly $(1 + z)^n, n = 4.5$) for galaxies in all mass bins. The mean sSFRs are smaller in high-mass galaxies than in low-mass galaxies at all redshifts. It is interesting to consider this result in the context of "downsizing", a term which generally is taken to imply that more massive galaxies formed their stars before less massive galaxies (Cowie et al. 1996). An increasing amount of observational evidence supports this idea, in particular through studies of the (specific) star formation rate (Juneau et al. 2005; Pérez-González et al. 2005; Caputi et al. 2006; Papovich et al. 2006; Reddy et al. 2006; Noeske et al. 2007). Figure 4.2 shows that the sSFRs of massive galaxies are the lowest of the whole sample. This indicates that they have already formed the bulk of their stars and that active star formation has shifted to the galaxies that are less massive. Additional support comes from a theoretical perspective. Guo & White (2008) investigated the contribution of star formation to galaxy growth in the Millennium Simulation. They found that even out to $z \sim 4 - 5$ less massive galaxies are always growing faster than galaxies of high stellar mass.

It is interesting to see that although we see a change in the locus of star formation (from massive to less massive systems), we do not find any mass-dependence of the *evolution* of the specific star formation rates. High-mass galaxies and low-mass galaxies appear to evolve at the same rate out to $z \sim 1.8$, although deeper data are necessary to reduce possible effects of incompleteness of the lowest mass bins at high redshift.

Next we compare our passive fraction in our highest redshift bin to observational results from the literature. A recent estimate can be found in work by Labbé et al. (in prep.), who found $35 \pm 7\%$. We also re-determined the quiescent fraction for Kriek et al. (2006) by analyzing the full sample presented in Kriek et al. (2008). We defined all galaxies without emission lines and $sSFR < 0.05$ Gyr^{-1} to be quiescent. Out of the 28 galaxies at redshift $z > 2$, $36 \pm 9\%$ are quiescent according to this method, applying a bootstrap error. The values of Labbé et al. (in prep.) and Kriek et al. (2008) are consistent with our fraction within 1σ. We note that our value is lower, but we emphasize that all studies use different definitions which can influence the result. We return to that below.

To investigate the difference in the estimates of the quiescent fractions further, we look at our MIPS fluxes and compare them with results from the CDFS (Labbé et al. 2005). For the overlapping sources in their sample and ours, we observed a median positive offset in MIPS flux of $4 \, \mu Jy$ with respect to the CDFS, which means our SFRs are overestimated. To investigate whether this offset could be responsible for the difference in passive fraction, we simulated the effect errors in MIPS flux would have on our results. We randomly added a measurement of the difference in MIPS flux to a collection of simulated passive galaxies with $M_* > 10^{11} M_\odot$ and determined the number of times the sSFR of such a source would scatter above the limit by which

we define a passive galaxy. Fifteen percent of the passive galaxies were classified as star forming after performing this test. This raises the fraction of quiescent galaxies at redshift $z \sim 1.8$ by 2%, which is not enough to explain the difference between the fractions.

We next compare our quiescent classification with the results from restframe optical spectroscopy of Kriek et al. (2008). Their sample contains 11 sources in the E-CDFS, 2 of which show no emission lines and are best fit with a passively evolving SED. We detect one of these sources in 24 μm with $S/N < 1$. Our SFR for it is $9 \pm 10\, M_\odot \mathrm{yr}^{-1}$, which is consistent with the $0.7 \pm 0.7\, M_\odot \mathrm{yr}^{-1}$ that Kriek et al. (2008) find. The other source has a sSFR of $2.4 \times 10^{-10}\,\mathrm{yr}^{-1}$, which exceeds the limit of $1/(3 \times t_H)$. It is still likely to be quenched as its sSFR is smaller than $1/t_H$. In summary, our results agree reasonably well for these two sources, but the exact definition of quiescence may cause variations in the result. As to illustrate this further, we relaxed our limit to sSFR$< 1/t_H$. For this limit, we find a quiescent fraction of 47±7% at $z \sim 1.8$ which is more than 1.5 times the fraction we found earlier.

In addition, the 24 μm emission we detect could be due to the presence of a weak and obscured AGN. This would mean that some of the galaxies we call star forming could in fact be quiescent galaxies hosting an obscured AGN. If this is the case, our fraction underestimates the real fraction. This is possible as evidence exists that AGN activity is widespread among massive galaxies at these redshifts (Daddi et al. 2007; Rubin et al. 2004; Kriek et al. 2007). We removed all X-ray detected sources from our sample as probable AGN candidates, but have no means to identify obscured AGNs that show strong 24 μm flux and weak X-ray emission. Our fraction would also be underestimated if the galaxy would hide an obscured star burst in its center.

Another effect is the error in the photometric redshifts, which we could have undervalued. The EAZY redshifts we use here are the results of several runs where we varied templates and error determination, which did not largely affect the outcome. We found that taking the 68% confidence range on the photometric redshifts of the galaxies leads to variations in the inferred SFR of 0.1 dex, which is not enough to significantly affect the results. Finally, there is a large diversity in the fields used for these studies and field-to-field variations could also be causing discrepancies.

Our most robust result is that we find a high fraction of galaxies with MIPS detections at redshift $z \sim 1.8$ and a small, but non-negligible fraction of quiescent galaxies, which we interpret as a lower limit. The galaxies that are detected in MIPS at redshift $z \sim 1.8$ are in some way active, either through star formation or black hole growth. Deeper 24 μm data and spectroscopic information will be crucial to be able to elaborate on this more.

Acknowledgments

References

Adelberger, K. L., Steidel, C. C. 2000, ApJ, 544, 218

lexander, D. M., et al. 2003, AJ, 126, 539

Arnouts, S., et al. 2001, A&A, 379, 740

Bell, E. F. 2003, ApJ, 586, 794

Bell, E. F., et al. 2005, ApJ, 625, 23

Bertin, E. & Arnouts, S. 1996, A&AS, 117, 393

Bolzonella, M., Miralles, J.-M., Pellø, R. 2000, A&A, 363, 476

Brammer, G. B., van Dokkum, P. G., Coppi, P. preprint (astro-ph/0807.1533)

Brinchmann, J., Charlot, S., White, S. D. M. , Tremonti, C., Kauffmann, G., Heckman, T., Brinkmann, J. 2004 MNRAS, 351, 1151

Bruzual, G., & Charlot, S. 2003, MNRAS, 2, 344, 1000

Cimatti, A., et al. 2002, A&A, 392, 395

Caputi, K., I., et al. 2006, ApJ, 637, 727

Cowie, L., L., Songaila, A., Hu, E., M., Cohen, J. G. 1996, AJ, 112, 839

Cristiani, S., et al. 2000, A&A, 359, 489

Daddi, E., et al. 2007, ApJ, 670, 173

Dale, D. A. & Helou, G. 2002, ApJ, 576, 159

Dickinson, M, et al. preprint (astro-ph/0204213)

Erben T., et al. 2005, AN, 326, 432

Fazio, G. G., et al. 2004, ApJS, 154, 10

Gawiser, E. et al. 2006, ApJS, 162, 1

Gilli R., et al. 2003, ApJ, 592, 721

Gordon, K. D., Clayton, G. C., Witt, A. N., Misselt, K. A. 2000, ApJ, 533, 236

Guo, Q. & White, S. D. M 2008, MNRAS, 384, 2

Hildebrandt, H., et al. 2006, A&A, 452, 1121

Juneau, S., et al. 2005, ApJ, 619, L135

Kauffmann, G. et al. 2003, MNRAS, 341, 33

Kaviraj, S., et al. 2008, MNRAS, 388, 67

Kriek, M., et al. 2006, ApJ, 649, 71

Kriek, M., et al. 2007, ApJ, 669, 776

Kriek, M., et al. 2008, ApJ, 677, 219

le Fèvre, O., et al. 2004, A&A, 428, 1043

Labbé, I. 2004, PhD Thesis

Labbé, I. et al. 2005, ApJ, 624, 81

Labbé, I., Bouwens, R., Illingworth, G, D., Franx, M. 2006, ApJ, 649, 67

Martin, D. C., et al. 2007, ApJS, 173, 415

Noeske, K. G., et al. 2007, ApJ, 660, 47

Papovich, C., et al. 2006, ApJ, 640, 92

Pérez-González, P. G., et al. 2005, ApJ, 630, 82

Pérez-González, P. G., et al. 2008, ApJ, 675, 234

Ravikumar, C. et al. 2007, A&A, 465, 1099

Reddy, N. A., Steidel, C. C., Fadda, D., Yan, L., Pettini, M., Shapley, A., Erb, D., Adelberger, K. L. 2006, ApJ, 644, 792

Rubin, K. H. R., van Dokkum, P. G., Coppi, P., Johnson, O., Förster-Schreiber, N., M., Franx, M., van der Werf, P. 2004, ApJ, 613, 5

Rudnick, G., et al. 2003, ApJ, 599, 847

Steidel, C. C., Giavalisco, M., Dickinson, M., Adelberger, K, L. 1996, AJ, 112, 352

Steidel, C. C., Adelberger, K. L., Giavalisco, M., Dickinson, M., Pettini, M. 1999, ApJ, 519, 1

Vanzella, E., et al. 2008, A&A, 478, 83

Virani, S., Treister, E., Urry, C. M., Gawiser, E. 2006, AJ, 131, 2373

Wolf, C., et al. 2004, A&A, 421, 913

Wuyts, S., Labbé, I., Förster-Schreiber, N., M., Franx, M., Rudnick, G., Brammer, G., B., van Dokkum, P. G 2008, ApJ, 682, 985

Zheng, X. Z., Bell, E. F., Papovich, C., Wolf, C., Meisenheimer, K., Rix, H.-W., Rieke, G, Somerville, R. 2007, ApJ, 661, 41

5

OBSERVATIONS VS. SIMULATIONS

We investigate the star formation history of the universe using FIRE-WORKS, a multiwavelength survey of the CDFS. We study the evolution of the specific star formation rate (sSFR) with redshift in different mass bins from z $= 0$ to $z \sim 3$. We find that the sSFR increases with redshift for all masses. The logarithmic increase of the sSFR with redshift is nearly independent of mass, but this cannot yet be verified at the lowest-mass bins at $z > 0.8$, due to incompleteness. We convert the sSFRs to a dimensionless growth rate to facilitate a comparison with a semi-analytic galaxy formation model that was implemented on the Millennium Simulation. The model predicts that the growth rates and sSFRs increase similarly with redshift for all masses, consistent with the observations. However, we find that for all masses, the inferred observed growth rates increase more rapidly with redshift than the model predictions. We discuss several possible causes for this discrepancy, ranging from field-to-field variance, conversions to SFR, and shape of the IMF. We find that none of these can solve the discrepancy completely. We conclude that the models need to be adapted to produce the steep increase in growth rate between redshift $z = 0$ and $z = 1$.

5.1   Introduction

To understand galaxy formation and evolution, it is essential to have a clear idea of how galaxies assemble their mass. Multiwavelength galaxy surveys of the high-redshift universe provide estimates of masses and star formation rates out to $z \sim 6$ (Lilly et al. 1996, Madau et al. 1996, and the compilations by Hopkins (2004) and Hopkins & Beacom (2006)). Recent studies of the evolution of the SFR per unit mass (specific SFR, sSFR) have shown that this quantity is an increasing function with redshift out to $z \sim 2$ and that, at a given redshift, the most massive galaxies typically have the lowest specific SFRs (Juneau et al. 2005, Bauer et al. 2005, Pérez-González et al. 2005; 2008, Caputi et al. 2006, Papovich et al. 2006, Reddy et al. 2006, Noeske et al. 2007, Martin et al. 2007, Zheng et al. 2007, Damen et al. 2009). Many of these studies support the idea of downsizing, where the locus of active star formation shifts from massive galaxies to less massive galaxies with time (Cowie et al. 1996).

It is interesting to compare these observations to model predictions. Using semi-analytical modeling (SAM) techniques, the formation of galaxies can be simulated within the standard cold dark matter (ΛCDM) cosmogony. SAMs have been relatively successful in reproducing numerous systematic properties of the observed local population at $z < 0.4$, such as number densities, luminosity functions, mass functions, and SFRs (e.g., Madau, Pozzetti & Dickinson 1998, Cole et al. 2000, Fontana et al. 2006, Fontanot et al. 2009). Since the recipes in the SAMs are arguably tuned to obtain such a good match, it is an interesting exercise to extend the comparison with observations to higher redshift, leaving the parameters of the SAMs to their locally tuned values. Several studies make the comparison for the high-redshift universe (Bower et al. 2006; Kitzbichler & White 2007; Marchesini & van Dokkum 2007; Davé 2008; Genzel et al. 2008; Guo & White in preparation, Elbaz et al. 2007, Daddi et al. 2007a, Santini et al. 2009).

Bower et al. (2006) find their model to be in good agreement with the observed mass function out to $z \sim 2$. However, their models overpredict the star formation density by $\sim$20% at low redshift ($z < 0.4$), whereas at $z \sim 1$ they underpredict the observations by a similar factor. Refinements to the code with respect to heating by active galactic nuclei (AGN; Bower et al. 2008) have not yet helped to reduce the relatively small discrepancies. A similar effect, where the models underpredict star formation observed at high redshift, is also seen in hydrodynamical simulations (both for multiwavelength (Davé 2008) and spectroscopic (Genzel et al. 2008) observations). Kitzbichler & White (2007) find an abundance of massive galaxies that overpredicts the observed abundance by a factor of $\sim$2 at $z = 2$. Studies by Elbaz et al. (2007), Daddi et al. (2007a), and Santini et al. (2009), reveal how SAMs underpredict the observed star formation rate by a factor 2-5 out to redshift $z = 2$.

In this chapter we explore the evolution of the star formation history of galaxies from redshift $z \sim 3$ to 0, using FIREWORKS, a K_S-band selected multiwavelength catalog of the CDFS, that includes deep MIPS data to allow derivation of SFRs. Galaxy growth can be conveniently quantified using the dimensionless growth rate, defined as sSFR $*t_H(z)$, where $t_H(z)$ is the Hubble time (Guo & White 2008). It provides a direct and quantitative constraint on the models. We first compare our results to other observational studies and then, using the growth rate, make a comparison with a SAM built on top of the Millennium Simulation. Throughout this chapter we assume a ΛCDM cosmology with $\Omega_{\mathrm{m}} = 0.3$, $\Omega_{\Lambda} = 0.7$, and $H_0 = 70$ km s^{-1} Mpc^{-1}. All magnitudes are given in the AB photometric system. Stellar masses are determined assuming a Kroupa (2001) initial mass function (IMF).

5.2   Data

5.2.1   Observations and Sample Selection

We use the FIREWORKS catalog for the GOODS-CDFS, generated by Wuyts et al. (2008). This catalog is based on high quality photometry ranging from the NUV to MIR. Wuyts et al. (2008) included deep space based optical imaging with HST using ACS (Giavalisco, Steidel & Macchetto 1996). They complemented this with optical imaging obtained as part of the COMBO-17 (Wolf et al. 2003) and ESO DPS (Arnouts et al. 2007) surveys, in the re-reduced form of the GaBoDs consortium (Erben et al. 2005; Hildebrandt et al. 2006). NIR imaging was obtained with VLT/ISAAC (Vandame 2002, Vandame et al. in preparation). For mid-IR wavelength coverage they used deep *Spitzer* imaging (IRAC and MIPS) from Dickinson et al. (in preparation).

A K_s-selected catalog was constructed following the procedures of Labbé et al. (2003) and contains the following bands: $U_{38}BVRI$ (WFI), $B_{435}V_{606}i_{775}$ z_{850} (ACS), JHK_s (ISAAC), 3.6-8.0 μm (IRAC) and 24 μm (MIPS). It has a 5 sigma depth in K_s of $\sim$24.3 and a total area of 138 arcmin^2. For details on observations, source detection and astrometry we refer to Wuyts et al. (2008). Using the CDFS X-ray catalog of Giacconi et al. (2002), we excluded all X-ray detected sources from the sample as they are likely AGN. We further restricted the selection to sources with a signal-to-noise higher than 10 in the K_s-band, which results in a total sample size of 5,274 sources.

5.2.2   Redshifts, masses and star formation rates

Wuyts et al. (2008) derived photometric redshifts using EAZY (Brammer et al. 2008) which are in good agreement with the available spectroscopic redshifts. The normalized median absolute deviation (NMAD) of $(z_{\mathrm{phot}} - z_{\mathrm{spec}})/(1 + z_{\mathrm{spec}})$ is 0.031 over the whole redshift range and NMAD = 0.071 at $z > 1.5$ (Wuyts et al. 2008). To obtain stellar masses, ages, dust attenuation and star formation rates, stellar population models were fitted to the

spectral energy distribution (SED) out to 8 μm. The SED modeling follows standard procedures, and is described by Förster Schreiber et al. (in preparation; see also e.g., Förster Schreiber et al. 2004). Bruzual & Charlot (2003) models were used with solar metallicity, a Salpeter IMF and a Calzetti reddening law. Masses and SFRs were converted to a Kroupa IMF by subtracting 0.2 dex. The fits were performed with the HYPERZ program (Bolzonella, Miralles & Pelló 2000), fixing the redshift to the photometric redshift derived with EAZY, or the spectroscopic redshift when available. Three star formation histories were fit and the best fitting model was used. The three star formation histories were: a single stellar population without dust, a constant star formation history and an exponentially declining star formation history with a characteristic timescale of 300 Myr, the latter two with varying amounts of dust ($0 < A_v < 4$). A full description of the SED fitting procedure and extensive tests on the outcome can be found in Förster Schreiber et al. (in preparation). Rest-frame luminosities were derived by interpolating between observed bands using the best-fit templates as a guide (see Rudnick et al. (2003) for a detailed description of this technique and Taylor et al. (2009) for the IDL implementation of the algorithm, dubbed 'InterRest'[1]).

In addition to the SFRs derived from SED fitting, SFRs were determined independently using a combination of rest-frame UV and IR emission. Between $1 < z < 3$, MIPS 24 μm traces the rest-frame 6-12 μm luminosity, which correlates broadly with the total IR luminosity. Using a wide range of templates from Dale & Helou (2002), bolometric luminosities were determined, adopting the mean of $\log(L_{IR})$, following Wuyts et al. (2008) and Labbé et al. (in preparation). In other words, we apply a linear conversion from observed 24 μm flux to L_{IR}, using a coefficient which depends also on redshift. The SFR was determined assuming

$$\Psi/M_\odot \ \text{yr}^{-1} = 1.09 \times 10^{-10} \times (L_{\text{IR}} + 3.3 \ L_{2800})/L_\odot, \qquad (5.1)$$

based on the conversion by Bell et al. (2003) converted to a Kroupa IMF (see also Wuyts et al. (2008), Labbé et al. (in preparation)). Unless stated otherwise, we use the MIPS derived SFRs in our analysis. The SFR determined from the SED fitting is used for comparison in later sections.

We include data from the Sloan Digital Sky Survey (SDSS) to extend our redshift coverage to $z = 0$. SDSS masses were determined by Kauffmann et al. (2003) using spectra. Brinchmann et al. (2004) derived SFRs from emission lines. For details on the derivation of the masses and SFRs in the SDSS we refer to their papers. Figure 5.1 shows the specific star formation rate with mass in four different redshift regimes ($z = 0, 1, 2, 3$). The first panel shows SDSS results, the others are based on the FIREWORKS data. Although the spread in sSFR is high at a given mass (see also Franx et al.
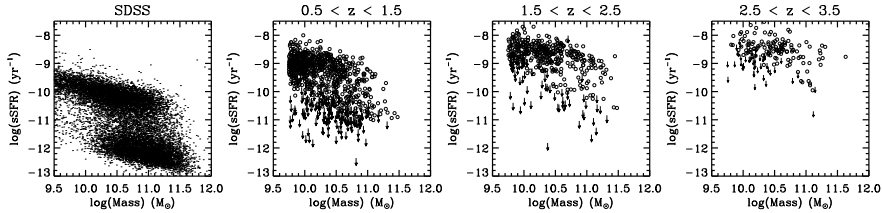
---

[1]http://www.strw.leidenuniv.nl/~ent/InterRest

Figure 5.1 − sSFR against mass, for the low redshift sample from the SDSS, and at mean redshifts, $z = 1, 2, 3$. Open circles are the FIREWORKS detections, arrows show 2σ upper limits of the sSFR.

Table 5.1 − 75% completeness limits

$\log(M_*/M_\odot)$	z
9.0 -9.5	0.5
9.5 -10.0	0.9
10.0 -10.5	1.5
10.5 -11.0	2.9
> 11.0	2.9

2008), two trends are clear. Galaxies of higher mass typically have lower sSFRs and at fixed mass the sSFR rises with redshift. Both trends have been observed before and confirm earlier results (Bauer et al. 2005, Zheng et al. 2007, Pérez-González et al. 2008, Damen et al. 2009). We will discuss the evolution of the sSFR further in Section 5.3.

5.2.3 Mass completeness

We determine the mass completeness limit using our K_s-band selection limit. We scale the masses of sources down to flux selection limit of 10 σ ($M_{scaled} = M \times 10/[S/N]_{K_S}$) and determine the mass limit to which we can detect 75% of the sources at $10\,\sigma$ in a narrow redshift bin. We find that our sample is 75% complete for masses higher than $10^{11} M_\odot$ out to $z \sim 3$. The completeness limits are listed in Table 5.1. In the remainder of this chapter, all references to completeness are based on the 75% completeness limits.

5.3 The Evolution of the Specific Star Formation Rate

In Chapter 4 we studied how the SFR changes with mass and redshift out to $z \sim 2$. We used the SIMPLE survey, which is based on NUV to NIR observations of the E-CDFS. With an area of $0.5° \times 0.5°$, the E-CDFS is ∼6.5 times larger than the much deeper FIREWORKS area. Here we extend this analysis to higher redshift and lower masses, using the FIREWORKS survey of the CDFS. We determine the average SFR in five different mass bins
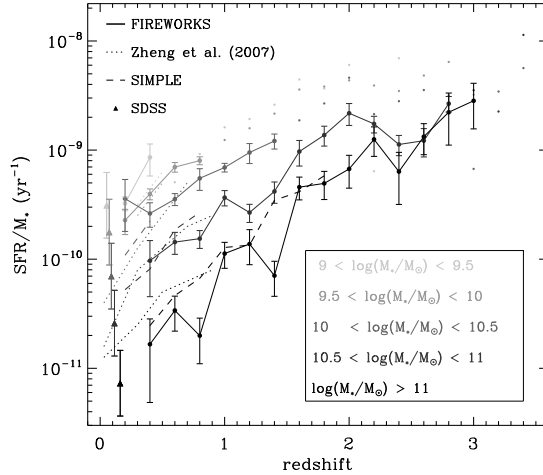
Figure 5.2 − sSFR versus redshift in different mass bins. Filled, connected circles are the FIREWORKS results, dots show where mass incompleteness starts to play a role. The error bars represent bootstrap errors. The dashed and dotted lines represent results from Damen et al. (2009) and Zheng et al. (2007), respectively. SDSS data were used to include a local data point (*triangles*).

and investigate the evolution of the specific SFR with redshift. For sources with no significant MIPS flux, we did not use upper limits to determine the average, but included the measured fluxes.

Our results are shown in Figure 5.2. Different shades represent different mass bins and dots denote where we suffer from incompleteness. Error bars represent the bootstrapped 68% confidence levels on the average sSFRs. Local SDSS data points (triangles) were added to the figure and lie on the same trend as our results. We also compare our results to previous similar studies. Dotted lines show the results of Zheng et al. (2007) who used the COMBO-17 survey. Dashed lines represent the work of Damen et al. (2009), based on the SIMPLE survey.

Those papers showed that sSFRs of massive galaxies are typically smaller than those of less massive galaxies and that the increasing trend of sSFR with redshift has a similar slope for all masses. For the lowest to average mass bins ($9.0 < \log(M/M_\odot) < 11$) we confirm results from Zheng et al. (2007) and Damen et al. (2009) and extend them out to higher redshifts. However, the sSFRs in the highest mass bin ($M_* > 10^{11} M_\odot$), seem to be lower than both the results from SIMPLE and Zheng et al. 2007. This can be a matter of low number statistics, since the average number of galaxies per redshift bin for these masses is ~ 8.

To quantify the slopes of the trends in each mass bin, we fitted the sSFR

Table 5.2 − Slope of sSFR-z relation

$\log(M_*/M_\odot)$	n
9.5 -10	4.40$\pm$ 0.31
10 -10.5	3.36$\pm$ 0.87
10.5-11	3.63$\pm$ 0.33
> 11	4.78$\pm$ 0.37

with $(1 + z)^n$ over the redshift range where it is complete with respect to mass. We used a bootstrapping technique to determine errors on the fits. The resulting values for the steepness of the slope, n, are listed in Table 5.2.

It is interesting to regard these values in the context of downsizing. We can see that at fixed redshift, the sSFR decreases with increasing mass. This indicates that the most massive galaxies have already formed the bulk of their stars and that active star formation has shifted to galaxies that are less massive. However, we do not see a strong mass dependence in the decline of the sSFR with time. This confirms results from Zheng et al. (2007) and Damen et al. (2009), whereas it seems to disagree with the results of Juneau et al (2005), who find that, out to $z = 1.5$, the sSFRs of more massive galaxies decrease faster in time than those of the lowest-mass galaxies. Taking into account the error bars in their Figure 3, this disagreement could be subtle.

Admittedly, the redshift range over which we determined n is small for the low-mass bins (see Figure 5.2). In addition, the highest mass bin $\log(M_*) > 11M_\odot$ suffers from low number statistics. We verified whether our results would change with a larger number of sources by including the SIMPLE data, and find that the trend in Figure 5.2 at the high-mass end remains the same. Including the SIMPLE data does not alter the results in a way that evolution in the slope can be confirmed. To be more conclusive, these fits need to be determined over similar redshift ranges for all mass bins. Deeper observations, that solve the incompleteness issues, are needed to accurately make a statement about the possible evolution of n with mass.

5.4   Comparison with Model Predictions

Next, we compare our results with model predictions. We use the work of Guo & White (2008), who have used data from the Millennium Simulation to study the growth of galaxies through mergers and star formation in the semi-analytic models of de Lucia & Blaizot (2007)[2].

In a qualitative way, the results of Guo & White (2008) concerning star

---

[2]Please note that the de Lucia & Blaizot (2007) model assumes a Chabrier IMF. This will not significantly affect the comparison, since it greatly resembles the Kroupa IMF that we apply.
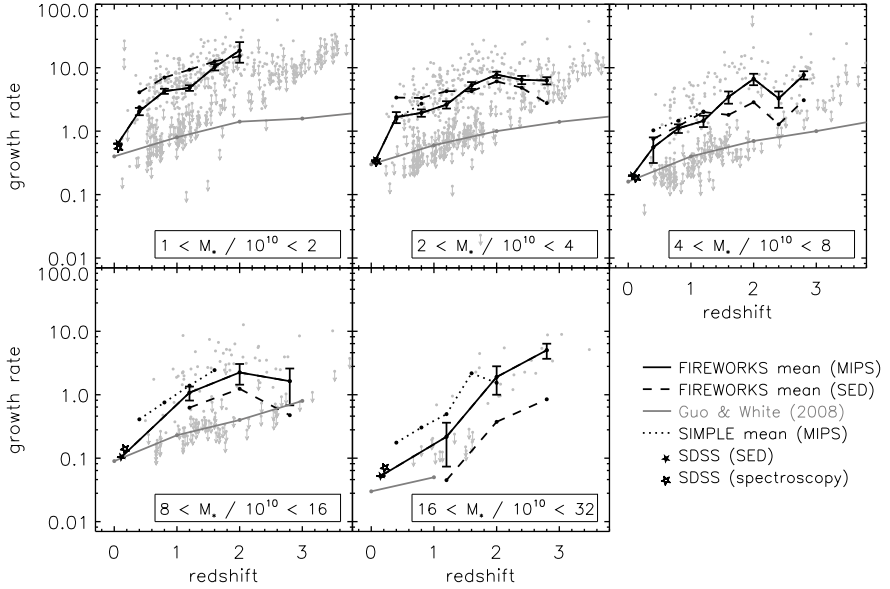
Figure 5.3 − Dimensionless growth rate through star formation as a function of redshift. The different panels represent different mass bins in units of 10^{10} $M_\odot$. The gray dots are the FIREWORKS values, the black line is their mean. Open circles with arrows denote upper limits set at the 2σ level. Overplotted in gray are the results from Guo & White (2008), based on the Millennium Simulation. Additional observational measurements are added, based on SFRs determined from SED fitting (*dashed line*) and the results from SIMPLE (*dotted line*, Damen et al. 2009). To represent the local universe, both a photometric (*black star*) and a spectroscopic (*open star*) measurement from SDSS were included. Note the large offset between the model and the observations between redshift z=0 and z=1. The model and observations both show an increase of the growth rate with redshift, but for the model this trend is more gentle.

formation are consistent with the observed trends in Figure 5.2. They find that the growth rates through star formation increase rapidly with redshift, for all stellar masses. In addition, they find that specific growth rates through star formation are smaller in high-mass than in low-mass galaxies at all redshifts. Although qualitatively their model predictions agree with our results, quantitatively this is not the case. We determine dimensionless growth rates for our sample similar to Guo & White (2008). The growth rate is defined as $GR_{sf} = SFR/M_* \cdot t(z)$: the sSFR multiplied with the age of the universe at the redshift of observation. We determine mean values of this growth rate at all redshifts, in the same mass bins Guo & White (2008) use. The results can be seen in Figure 5.3. The gray dots and black line represent the FIREWORKS growth rates and their binned mean. The results from Guo & White (2008) are shown in black. For comparison with the local universe we used SFRs and masses from the SDSS to determine growth rates at $z = 0$. We included both estimates from SED fitting (J. Brinchmann, private communication, black star) and from emission lines (Brinchmann et al. 2004, open star). The SAMs are tuned to fit the local universe and, except for the highest mass bin, the agreement is excellent.

Although the growth rates agree at redshift $z = 0$, at higher redshifts the observed growth rates increase much more rapidly than the model growth rates. The overall offset between redshifts $z = 1$ and $z = 2$ is a factor of ~ 6.3 for all masses. Per mass bin, we find offsets by factors of 4.0 ($8 \cdot 10^{10} M_\odot - 16 \cdot 10^{10} M_\odot$), 6.2 ($4 \cdot 10^{10} M_\odot - 8 \cdot 10^{10} M_\odot$), 6.0 ($2 \cdot 10^{10} M_\odot - 4 \cdot 10^{10} M_\odot$) and 9.1 ($10^{10} M_\odot - 2 \cdot 10^{10} M_\odot$) at redshifts $z = 1 - 2$. This agrees well with recent results in the literature. Elbaz et al. (2007) and Daddi et al. (2007a) found an excess in observed sSFRs with respect to those predicted by the Millennium Simulation of a factor of ~ 2.5 ($z \sim 1$) and ~ 4 ($z \sim 2$), respectively, for galaxies of $3 \cdot 10^{10} M_\odot$. Recent work by Santini et al. (2009) shows a similar trend where the Millennium Simulation undepredicts star formation activity by a factor 3-5. Though both these studies and our own are based on observations of the same field, there are a differences in sample selection, determination of SFRs and photometric redshifts. Given the wide variety in methods and samples used, it is remarkable that the observations converge to consistent results, namely high sSFRs with respect to model predictions.

This discrepancy could have its origin in the derivation of our SFRs based on the MIPS 24 μm fluxes. To test this we include the growth rates derived from the SFRs from our SED fits (*dashed lines*). The growth rates derived from the bolometric fluxes and the SED fits are generally consistent with each other, except at the highest masses. This result is remarkable and it argues against the hypothesis that a simple conversion error in the calculation of the SFR causes the problem. It is interesting to note that the SED fits generally give lower sSFRs for the highest mass galaxies than the sSFRs based on UV + 24 μm. AGN may be partially responsible (Daddi et al. 2007b). We will
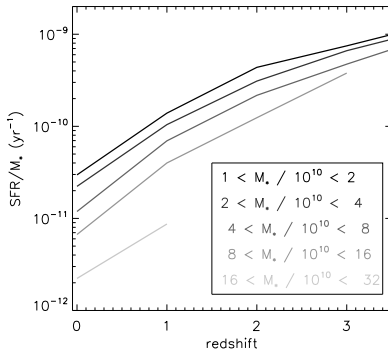
Figure 5.4 − sSFR versus redshift for the Guo & White (2008) results. Different colors represent the mass bins used in Figure 5.3. The slope of the evolution of sSFR with redshift is nearly independent of mass, which agrees with the FIREWORKS results.

return to the effect of errors in the SFR determination in the next section.

A different cause could be that the CDFS suffers from cosmic variance. We added in the results from the SIMPLE survey, which is based on observations on the E-CDFS and has ∼6.5 times more area (*dotted lines*). Both fields show similar results. As an additional exercise, we redetermined the SIMPLE growth rates excluding the CDFS and for the CDFS only, to see whether the different areas show substantial differences in growth rates. We find that for all masses and at all redshifts, the growth rates for both areas are consistent with each other within 1σ. Field to field variation, therefore, does not seem to cause a significant error. It is interesting to note, that although the steepness of the observed slope is not reproduced by the model, the slope is the same for galaxies of low and high mass. To illustrate this, we used the model growth rates to derive sSFRs for the Guo & White (2008) data. The results are shown in Figure 5.4. Different shades represent the same mass bins used in Figure 5.3. Both for the model and observations, the rate of increase of sSFR does not seem to be a strong function of mass.

5.5 Discussion

We use the FIREWORKS survey to investigate the star formation history in the CDFS. We find that the sSFR is an increasing function with redshift for all masses. The slope of the trend is similar for galaxies of all masses, although some uncertainties remain due to incompleteness at the low-mass end and low number statistics in the highest mass bin ($> 10^{11} M_\odot$). These findings are in agreement with results from previous studies (Martin et al. 2007, Zheng et al. 2007, Pérez-González et al. 2008, Damen et al. 2009).

We also compare our results to model predictions of Guo & White (2008), who use the galaxy formation model of de Lucia & Blaizot (2007) based on the Millennium Simulation and find that for both the model and the observations the growth rate increases with redshift for all masses. However, the model

fails to reproduce the steep rise that is observed in the data, particularly between $z = 0$ and $z = 1$, a redshift range where observations are most reliable. The overall value of the growth rate is higher in the observations than in the models, by a factor of $\sim$6.3 on average. This discrepancy between the model and the data is caused by problems with the observations, the model, or both.

First of all, field to field variation may play a role. We have already discussed in Section 5.4 that this is unlikely to be a large effect. An additional factor of uncertainty resides in our estimate of the SFR based on MIPS fluxes. AGNs would contribute to the 24 μm emission and generate overestimated SFRs. Although we removed all X-ray detections from our sample, dust-obscured AGNs that show strong 24 μm flux can not be identified. Furthermore, systematic uncertainties in the conversion from MIPS fluxes to total IR luminosities are of the order of a factor 3 at $z \sim 2$ (Labbé et al. in preparation). In addition, we can not be sure that the local IR templates on which we base our conversion still hold in the $z > 1$ universe. Marcillac et al. (2006) suggest that local templates are still accurate out to $z \sim 1$. Papovich et al. (2007) argue that at $z \sim 2$, local templates overpredict the total IR luminosity by a factor of a few. However, their local templates include a luminosity dependent conversion. In contrast, we apply a single template (without luminosity dependence), which results in smaller systematic offsets. In addition, we found good agreement between the average SFRs based on MIPS flux and SED modeling for the low- to intermediate-mass galaxies. It is interesting to compare and investigate other measurements of the SFR. SFRs based on H_α, for instance, agree quite well with SFRs based on SED modeling (Förster Schreiber submitted). Furthermore, growth rates based on H_α show significant disagreement with model predictions (Genzel et al. 2008), similar to what we find. Concluding, it is unlikely that the full discrepancy is caused by the systematic uncertainties in deriving SFRs. A third reason why our SFRs are large, could be the assumption of a non-evolving IMF. Recently, there have been several authors who suggest that the IMF is not constant, but instead evolves with redshift. Van Dokkum (2008; vD08) found that reconciling the evolution of color and mass-light-ratio of massive, early-type cluster galaxies favors a top-heavy IMF. Davé (2008; D08) argues that an evolving IMF brings the observed evolution in the relationship between SFR and stellar mass in better agreement with model predictions. Finally, Wilkins et al. (2008; W08) claim that the assumption of a simple model for an evolving IMF significantly reduces the discrepancy between the integrated SFH and stellar mass density measurements.

We used the effect an evolving IMF would have on SFRs (Figure 3 from W08, Figure 3 from D08) and sSFRs (Figure 12a and Figure 14b from vD08) to redetermine our growth rates and show the results in Figure 5.5[3]. It is

---

[3]The model predictions were kept to the values based on the non-evolving Chabrier IMF
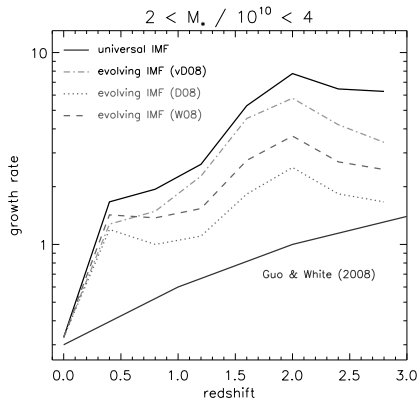
Figure 5.5 − Dimensionless growth rate as a function of redshift for galaxies with masses ranging from $2 \cdot 10^{10} M_\odot$ to $4 \cdot 10^{10} M_\odot$. The black solid line shows the FIREWORKS result when a Kroupa (2001) IMF is applied. The dashed-dotted lines, dashed, and dotted lines show the FIREWORKS growth rate based on an evolving IMF, according to the parametrization of van Dokkum (2008; vD08), Davé (2008; D08), and Wilkins et al. (2008; W08), respectively. The corrected values based on the IMFs of D08 and W08 are lower limits, since they do not include the effect an evolving IMF has on the stellar mass. Introducing a time-dependent IMF decreases the discrepancy between the observations and the simulated results from Guo & White (2008; *dark gray solid line*), but it does not completely resolve it. In particular, the steep increase in observed growth rate at low redshift (z = 0 - 1) is still evident.

important to note that for the W08 and D08 growth rates (*represented by the dashed and dotted lines*), we only included the effect an evolving IMF has on SFR, and not on mass. For this reason those curves should be regarded as lower limits. The overall factor with which the growth rate decreases when an evolving IMF is applied is ∼1.3 for van Dokkum (2008), ≲1.8 for Wilkins et al. (2008) and ≲ 2.4 for Davé (2008). Although this helps reducing the discrepancy between the instantaneous SFR and SFR based on the mass function (W08), the steep increase between z = 0 and z = 1 is still intact.

Finally, the use of photometric redshifts introduces some uncertainty to the SFR estimates. We note, however, that the growth rates of SIMPLE (*dotted line in Figure 5.3*) are based on the photometric redshifts of COMBO-17, which are highly accurate out to $z \sim 0.8$. Since the SIMPLE results show the same strong slope as the FIREWORKS growth rates, we do not expect photometric redshift errors to be a significant cause for the discrepancy between the model and observations.

None of the effects we discussed above can provide a clear-cut solution to explain the difference between the model and observations, particularly the observed steep rise in growth rate between z=0 and z=1. The discrepancy could be caused by a flaw in the models, e.g., concerning for instance the gas supply to the galaxy. The current way stars are formed in SAMs is by

heating gas to the virial temperature after which it gradually cools to the temperature where star formation can commence. Dekel et al. (2009) show that this process is too slow to explain the fact that massive galaxies have already formed most of their stars at high redshift. They introduce a new way of star formation, where cold gas enters the dark matter halo through filaments and can start forming stars immediately. It would be interesting to investigate how this implementation of star formation would alter model predictions and whether it would be able to reproduce the steep rise of the growth rate at low redshifts.

Despite the differences we identified between our observations and the model values of Guo & White (2008), we also found an interesting agreement. It is remarkable that both observations and models find that the increase in sSFR is the same for low- and high-mass galaxies. There is no evidence for a "break" redshift at any of the masses studied here. Any modification in model recipes would have to maintain this mass independence.

Acknowledgments

References

Arnouts, S., et al. 2007, A&A, 476, 137

Bauer, A. E., Drory, N., Hill, G. J., Feulner, G. 2005, ApJ, 621, 89

Bell, E. F. 2003, ApJ, 586, 794

Bolzonella, M., Miralles, J.-M., Pelló, R. 2000, A&A 363, 476

Bower, R. G., Benson, A. J., Malbon, R., Helly, J. C., Frank, C. S., Baugh, C. M., Cole, S., Lacey, C. G. 2006, MNRAS, 370, 645

Bower, R. G., McCarthy, I. G., Benson, A. J. 2008, MNRAS, 390, 1399

Brammer, G. B., van Dokkum, P. G., Coppi, P. preprint (astro-ph/0807.1533)

Brinchmann, J., Charlot, S., White, S. D. M. , Tremonti, C., Kauffmann, G., Heckman, T., Brinkmann, J. 2004 MNRAS, 351, 1151

Bruzual, G., & Charlot, S. 2003, MNRAS, 2, 344, 1000

Caputi, K., I., et al. 2006, ApJ, 637, 727

Cole, S. et al. 2000, MNRAS, 319, 168

Cowie, L., L., Songaila, A., Hu, E. M., Cohen, J. G. 1996, AJ, 112, 839

Daddi, E., et al. 2007a, ApJ, 670, 156

Daddi, E., et al. 2007b, ApJ, 670, 173

Dale, D. A. & Helou, G. 2002, ApJ, 576, 159

Damen, M. C., Labbé, I., Franx, M., van Dokkum, P. G., Taylor, E. N., Gawiser, E. J., 2009, ApJ, 690, 937

Davé, R. 2008, ApJ, 385, 147

Dekel, A., et al. 2009, Nature, 457, 451

De Lucia, G. & Blaizot, J. 2007 MNRAS, 375, 2

Dickinson, M, et al. preprint (astro-ph/0204213)

Elbaz, D., et al. 2007, A&A, 468, 33

Erben T., et al. 2005 AN, 326, 432

Fontana, A., et al. 2004, A&A, 23

Fontanot, F., De Lucia, G., Monaco, P., Somerville, R. S., Santini, P. 2009, in press (astro-ph/0901.1130)

Förster Schreiber, N. M. et al. 2004, ApJ, 616, 40

Förster Schreiber, N. M. et al. (astro-ph/0903.1872)

Franx, M., Dokkum, P. G, van, Förster Schreiber, N. M, Wuyts, S., Labbé, I., Toft, S. 2008, ApJ, 688, 770

Genzel, R., 2008, ApJ, 687, 59

Giacconi, R. 2002, ApJS, 139, 369

Giavalisco, M., Steidel, C. C., Macchetto, F. D., 1996, ApJ, 470, 189

Guo, Q. & White, S. D. M 2008, MNRAS, 384, 2

Guo, Q. & White, S. D. M, preprint (astro-ph/0809.4259)

Hildebrandt, H., et al. 2006, A&A, 452, 1121

Hopkins, A. M. & Beacom, J. F. 2006, ApJ, 651, 142

Hopkins, A. M. 2004, ApJ, 615, 209

Juneau, S., et al. 2005, ApJ, 619, L135

Kauffmann, G. et al. 2003, MNRAS, 341, 33

Kitzbichler, M, G, White, S. D. M 2007, MNRAS, 376, 2

Kroupa, P. 2001, MNRAS, 322, 231

Labbé, I. et al. 2003, AJ, 125, 1107

Lilly, S. J., Le Févre, O., Hammer, F., & Crampton, D. 1996, ApJ, 460, L1

Madau, P., Ferguson, H. C., Dickinson, M. E., Giavalisco, M., Steidel, C. C., &

Fruchter, A. 1996, MNRAS, 283, 1388

Madau, P., Pozzetti, L., Dickinson, M. 1998, ApJ, 498, 106

Marchesini, D., & van Dokkum, P. G. 2007, ApJ, 663, 89

Marcillac, D., Elbaz, D., Chary, R. R., Dickinson, M., Galliano, F., Morrison, G. 2006, A&A, 451, 57

Martin, D. C., et al. 2007, ApJS, 173, 415

Noeske, K. G., et al. 2007, ApJ, 660, 47

Papovich, C., et al. 2006, ApJ, 640, 92

Papovich, C., et al. 2007, ApJ, 668, 45

Pérez-González, P. G., et al. 2005, ApJ, 630, 82

Pérez-González, P. G., et al. 2008, ApJ, 675, 234

Reddy, N. A., Steidel, C. C., Fadda, D., Yan, L., Pettini, M., Shapley, A., Erb, D., Adelberger, K. L. 2006, ApJ, 644, 792

Santini, P., et al. 2009, A&A, in press (astro-ph/0905.0683)

Rudnick, G., et al. 2003, ApJ, 599, 847

Taylor, E. N., et al. in press (astro-ph/0903.3051)

Vandame, B. 2002, SPIE, 4847, 123

Vandame, B. et al. preprint (astro-ph/0102300)

van Dokkum, P. G. 2008, ApJ, 674, 29

Wilkins, S, M, Trentham, N., Hopkins, A., M. 2008 MNRAS, 385, 687

Wolf, C., Meisenheimer, K., Rix, H.-W., Borch, A., Dye, S., Kleinheinrich, M. 2003, A&A, 401, 73

Wuyts, S., Labbé, I., Förster Schreiber, N. M., Franx, M., Rudnick, G., Brammer, G., B., van Dokkum, P. G 2008, ApJ, 682, 985

Zheng, X. Z., Bell, E. F., Papovich, C., Wolf, C., Meisenheimer, K., Rix, H.-W., Rieke, G. H., Somerville, R. 2007, ApJ, 661, 41

Nederlandse samenvatting

Het nabije heelal

Ons zonnestelsel maakt deel uit van de Melkweg, een verzameling van honderden miljarden sterren, die op een heldere nacht zeer duidelijk zichtbaar is als een brede baan van sterren aan de hemel. Objecten als de Melkweg, ook wel sterrenstelsels genoemd, zijn de belangrijkste bouwstenen van ons heelal en we kunnen aan de hand van eigenschappen van sterrenstelsels nu en in het verleden een beeld krijgen hoe het heelal zich sinds de oerknal heeft ontwikkeld tot de diversiteit aan hemelobjecten die we in het nabije heelal waarnemen.

Zo zijn er twee duidelijk verschillende soorten sterrenstelsels te onderscheiden: spiraal- en ellipsstelsels (zie Fig. 1.1). Dit onderscheid werd voor het eerst gemaakt door Edwin Hubble, een beroemd astronoom die aan het begin van de vorige eeuw ontdekte dat ons sterrenstelsel niet het enige is aan de nachtelijke hemel. Hij was daarmee de grondlegger van de extragalactische astronomie: de studie van objecten buiten onze Melkweg. Hij stelde een classificatiesysteem op dat tot op de dag van vandaag gebruikt wordt. De classificatie gaat uit van morfologische kenmerken, maar vorm is niet het enige verschil tussen de twee soorten sterrenstelsels. Spiraal- en ellipsstelsels verschillen ook op het gebied van kleur, de hoeveelheden stof en gas die aanwezig zijn, en de snelheid waarmee sterren gevormd worden.

In spiraalstelsels worden bijvoorbeeld voortdurend nieuwe sterren gevormd. Dit leidt tot een blauwe kleur, aangezien jonge sterren heet zijn en hun straling voornamelijk uitzenden in het ultraviolette gebied van het elektromagnetisch spectrum. Een ellipsstelsel daarentegen bestaat voornamelijk uit oude sterren die helder zijn op (infra)rode golflengten. Qua vorm vertonen spiraalstelsels een rijke structuur van spiraalarmen die, vervlochten met stroken van stof in een schijf roteren. Dit lijkt in sterk contrast met de homogene verdeling van sterren die een ellipsstelsel kenmerkt. Dit is slechts schijn, want uit nadere inspectie blijkt dat elliptische stelsels een rijke interne structuur vertonen, waarin de sterren onverwachts en tegendraads kunnen bewegen.

Deze tweedeling in de nabije sterrenstelsels manifesteert zichzelf duidelijk in een diagram waarin de kleur van de stelsels wordt uitgezet tegen de massa. Hierin is te zien dat de rode stelsels veel zwaarder zijn en een nauwe

zogenaamde 'rode reeks' vormen. De blauwe, stervormende stelsels zijn veel minder zwaar en losser gegroepeerd in een 'blauwe wolk' (zie ook Fig. 1.2). Deze strikte scheiding is opmerkelijk. Blijkbaar hebben de twee soorten sterrenstelsels zeer uiteenlopende onstaansgeschiedenissen. Hoe is deze tweedeling ontstaan? Waarom hebben de sterrenstelsels de vormen die ze hebben en welke processen zijn daarvoor verantwoordelijk? Deze vragen komen allemaal op hetzelfde neer; de grote vraag is: Hoe en wanneer zijn sterrenstelsels ontstaan?

Om deze vraag te kunnen beantwoorden, moeten we de sterrenstelsels in meer detail bestuderen en het liefst op het moment dat ze zich net vormden. Dat lijkt moeilijk te realiseren, maar er is een specifiek kenmerk van het heelal dat dit mogelijk maakt: de eindigheid van de lichtsnelheid.

Het verre heelal

Om te ontdekken hoe sterrenstelsels zijn gevormd en te weten te komen hoe ze zich daarna hebben ontwikkeld moeten we het verre heelal bestuderen. Dankzij de eindigheid van de lichtsnelheid bereikt het licht van een afgelegen bron ons namelijk pas na een hele tijd. Op die manier krijgen we een beeld van het stelsel zoals het eruit zag toen het licht werd uitgezonden, soms wel miljoenen jaren geleden. Hoe groter de afstand tussen ons en het object dat de straling heeft uitgezonden, des te verder we in het verleden kunnen kijken. In de afgelopen jaren is het steeds beter mogelijk geworden om dergelijke afgelegen (en dus zeer lichtzwakke) bronnen te observeren, dankzij indrukwekkende technologische ontwikkelingen. Grote telescopen en gevoelige instrumenten hebben een luik geopend naar het verre heelal, wat betekent dat we tegenwoordig sterrenstelsels kunnen vinden waarvan het licht al ∼13 *miljard* jaar onderweg is. Kosmologisch gezien is dat slechts een fractie na de oerknal. We kunnen de evolutie van sterrenstelsels dus over de gehele geschiedenis van het heelal bestuderen, door simpelweg te registreren welk soort sterrenstelsels we op welke afstand aantreffen.

Dit soort 'terugblikstudies' zou niet mogelijk zijn zonder een andere belangrijke eigenschap van het heelal, namelijk het feit dat het al sinds de oerknal expandeert. Vrijwel alle informatie over het verre heelal is gebaseerd op de analyse van elektromagnetische straling, uitgezonden door afgelegen objecten. Tijdens hun reis van de bron naar de telescoop ondervinden de fotonen het effect van kosmische expansie: hun golflengte wordt uitgetrokken (roodverschoven). Dit effect wordt groter naarmate een foton langer onderweg is. De mate van verschuiving is dus een nauwkeurige bepaling van de afstand tot de bron (ook wel roodverschuiving genaamd). Deze twee belangrijke kenmerken van het heelal maken het voor astronomen mogelijk om in kaart te brengen hoe en wanneer sterrenstelsels zich vormden.

Dit wil echter nog niet zeggen dat dit een makkelijke opgave is. Tijdens hun reis verliezen de fotonen energie en daarmee lichtkracht. In het onderzoek

naar de evolutie van sterrenstelsels wordt gewerkt met zeer zwakke signalen. Het was dan ook pas in de jaren '90 van de vorige eeuw dat het verre heelal voor het eerst goed waargenomen kon worden, door de ontwikkeling van een nieuwe generatie telescopen met een diameter van 8-10 m. Dankzij die telescopen en een slimme selectiemethode werd het mogelijk een grote populatie van afgelegen sterrenstelsels te identificeren. Deze zogenaamde 'Lyman Break Galaxies' (LBGs) worden geselecteerd op hun specifieke kleur. Ze zijn zeer helder en vormen actief nieuwe sterren. De jonge, hete sterren in de LBGs stralen zeer helder in het ultraviolet. Dit uv-licht wordt onderweg roodverschoven en komt als optische straling op aarde aan. Het specifieke kenmerk van LBGs is dat ze in groene en rode optische filters zeer helder zijn, maar in het ultraviolet niet te zien. Deze techniek is ontzettend succesvol geweest en heeft honderden LBGs geïdentificeerd. Maar aangezien ze slechts de actief stervormende stelsels selecteert, geeft deze selectiemethode niet een compleet beeld van de totale populatie sterrenstelsels in het verre heelal.

Wanneer een sterrenstelsel zijn gasvoorraad heeft uitgeput, kan het geen nieuwe sterren meer vormen. Het licht van het stelsel verzwakt en wordt roder. De enige verandering die dan nog optreedt is het verouderingsproces van de sterren, dit wordt passieve evolutie genoemd. Omdat dit soort systemen geen jonge, hete sterren bevatten, zenden ze geen uv-straling uit en worden ze gemist door de LBG selectietechniek. Dat dit niet bewijst dat ze er niet zijn, toonden de eerste resultaten van krachtige infrarode (IR) telescopen. Met behulp van infrarode waarnemingen werd een significante populatie rode stelsels gevonden, die veel overeenkomst vertoont met de elliptische stelsels in het nabije heelal. Deze rode stelsels vormen op een roodverschuiving van $z = 1$, dat wil zeggen, zo'n 8 miljard jaar geleden, eenzelfde 'rode reeks' als die in het nabije heelal is waargenomen.

Uit de waarnemingen kon worden berekend dat de hoeveelheid massa in de 'rode reeks' sinds $z = 1$ verdubbeld is. Dit kan niet verklaard worden door de vorming van nieuwe sterren in de rode stelsels, aangezien daar voornamelijk passieve evolutie plaatsvindt. Daar komt bij dat de totale massa van de 'blauwe wolk' over dezelfde tijdspanne ongeveer gelijk is gebleven, terwijl in die stelsels continu nieuwe sterren worden gevormd. Op de een of andere manier moeten er dus blauwe stelsels in de rode wolk terecht zijn gekomen (zie nogmaals Fig. 1.2). Het is nog niet helemaal duidelijk welk proces hiervoor verantwoordelijk is. Het kan zijn dat het komt door de samensmelting van twee blauwe stelsels. Tijdens een dergelijke botsing gaat veel gas verloren en zal het vormen van nieuwe sterren gestaag afnemen. Het kan zijn dat er ook andere processen meespelen.

Het is in ieder geval duidelijk dat het al dan niet vormen van sterren een grote rol speelt bij de ontwikkeling van sterrenstelsels. De zogenaamde stervormingssnelheid is dan ook een belangrijke parameter in het onderzoek naar de evolutie. Een van de wapenfeiten van dit vakgebied is het zogenaamde Madau-diagram. Dit diagram toont de evolutie van de gemiddelde

stervormingssnelheid in het heelal vanaf meer dan 12 miljard jaar geleden tot nu. Dankzij dit diagram, dat opgesteld is aan de hand van resultaten van verscheidene onderzoeksgroepen, weten we dat de snelheid waarmee sterren werden gevormd haar maximum bereikte rond $z = 3$ (meer dan 10 miljard jaar geleden) en dat ze sindsdien flink is afgenomen, ongeveer met een factor 10 (zie Fig. 1.3). Wat precies de oorzaak is van deze afname, is nog niet helemaal duidelijk. Opnieuw kunnen er meerdere processen verantwoordelijk zijn. Wel kunnen we afleiden dat de periode van ongeveer 10 miljard jaar geleden tot nu een interessante tijdperk is in de geschiedenis van het heelal, waarin veel sterrenstelsels hun huidige vorm verkregen.

De uitgebreide hoeveelheid onderzoeksresultaten lijkt te suggereren dat we de vorming en evolutie van sterrenstelsels vrij goed begrijpen, maar dat is niet het geval. Hoewel we op elke roodverschuiving sterrenstelsels hebben gevonden, wil dat nog niet zeggen dat we begrijpen hoe deze stelsels in elkaar overgaan. We mogen niet veronderstellen dat stelsels op verschillende roodverschuivingen de verschillende evolutiestadia van eenzelfde soort stelsel vertegenwoordigen. De belangrijkste reden hiervoor is dat er verschillende selectiecriteria worden gebruikt om sterrenstelsels op verschillende roodverschuivingen te vinden. Het is niet mogelijk om het traject te volgen van een individueel sterrenstelsel. Daarom is er een raamwerk nodig, gebaseerd op theoretische modellen, waarbinnen de waargenomen resultaten kunnen worden geïnterpreteerd.

Het ontwerpen van sterrenstelsels

Een van de meest belangrijke ontwikkelingen in de sterrenkunde is het opstellen van een standaard kosmologiemodel. Dit model beschrijft in grote lijnen hoe het heelal zich van de oerknal tot nu heeft ontwikkeld. In het begin bestond er enkel een homogeen plasma, dat slechts kleine dichtheidsschommelingen vertoonde. Met de uitdijing van het heelal koelde dit plasma af en ontstonden er uit de kleine fluctuaties de eerste sterren en sterrenstelsels. We weten dit omdat we zelfs vandaag de dag een echo van de oerknal kunnen ontvangen in de vorm van een uniforme achtergrondstraling. Aan de hand van zeer nauwkeurige waarnemingen van deze kosmische achtergrondstraling zijn de kleine fluctuaties ontdekt. Zij vormen het uitgangspunt voor kosmologisch modellen die de evolutie van het heelal beschrijven.

Een standaardmodel

Sterrenkundigen geloven dat sterrenstelsels ontstaan zijn in halo's van donkere materie. De aard van deze donkere materie is een van de grootste raadsels in het heelal. Het is onzichtbaar, maar alomtegenwoordig en beslaat ongeveer vijfmaal zoveel massa als het totaal aan zichtbare materie, waaruit alle sterrenstelsels, sterren, planeten, en ook wijzelf zijn opgebouwd.

De vorming en evolutie van de donkere halo's kunnen worden voorspeld door middel van numerieke simulaties. Deze simulaties verschaffen kwantitatieve voorspellingen voor verschillende eigenschappen van de verdeling van de donkere materie als een functie van tijd; van kort na de oerknal tot nu. Het is moeilijker het gedrag van de zichtbare, of baryonische, materie te voorspellen. In het vroege heelal gaat de evolutie van donkere en zichtbare materie gelijk op, maar zodra de eerste sterren zich vormen, ontstaan er complicaties. Het gedrag van het gas is onzeker, aangezien er met stervorming allerhande fysische processen gepaard gaan die de initiële homogene verdeling van het gas verstoren.

Er is in de afgelopen jaren veel vooruitgang geboekt om stervorming vanuit puur theoretisch oogpunt beter te begrijpen. En hoewel er veel tijd in geïnvesteerd wordt, bevat het standaard analytisch model nog steeds geen goedwerkend recept voor stervorming.

Semi-analytische modellen

Een dergelijk recept is wel aanwezig bij zogenaamde semi-analytische modellen. Dit zijn modellen die uitgaan van het standaardmodel en dan een beschrijving van de stervorming toevoegen. Deze beschrijving is gebaseerd op waarnemingen of op gedetailleerde simulaties van individuele systemen. Deze aanpak is erg effectief aangezien hij minder computerkracht vergt en er op die manier dus verschillende soorten beschrijvingen getest kunnen worden. Het enige nadeel is dat er bij de bouw van een semi-analytisch model verschillende aannames moeten worden gedaan over processen die nog niet helemaal zijn begrepen. Hierdoor is het moeilijk te zeggen hoe nauwkeurig de voorspellingen zijn. Desondanks zijn ze erg nuttig voor het beschrijven van de evolutie van sterrenstelsels. Ze produceren namelijk resultaten als de gemiddelde groei, die direct met waarnemingen vergeleken kunnen worden.

Dit proefschrift

Met het oog op de onzekerheden die bestaan in de huidige modellen zijn waarnemingen nodig om voorwaarden te leveren waaraan de modellen moeten voldoen. De eerdergenoemde 'terugblikstudies' zijn hierbij zeer belangrijk, omdat hieruit kan worden afgeleid wanneer er voor het eerst sprake was van een 'rode reeks'. In dit proefschrift presenteren we nieuwe waarnemingen en voeren we een 'terugblikstudie' uit gebruikmakend van gegevens die reiken van het ultraviolette tot het infrarode deel van het spectrum. We bepalen de stervormingssnelheid van de verzameling sterrenstelsels die hieruit voortkomt en brengen de evolutie ervan in kaart. Tenslotte vergelijken we de resultaten met voorspellingen van een semi-analytisch model.

In **Hoofdstuk 2** presenteren we "Spitzer's IRAC and MUSYC Public Legacy of the E-CDFS" (SIMPLE), een verzameling data gebaseerd op nieu-

we waarnemingen van de Spitzer ruimte telescoop, een telescoop die gevoelig is voor infrarode straling en dus goed de oude sterren in kaart kan brengen. Deze data combineren we met andere golflengtegebieden, van het ultraviolette tot het zichtbare licht.

De uiteindelijke catalogus bevat meer dan 60.000 bronnen, waarvan het overgrote deel zeer zwak is en niet gebruikt kan worden voor bepalingen van de stervormingssnelheid. De manier waarop we bruikbare bronnen selecteren luistert nauw. In **Hoofdstuk 3** vergelijken we verschillende selectiemethoden. We gebruiken hiervoor een optische selectielimiet, een ultraviolette selectielimiet en een selectie op massa. Het blijkt dat een verzameling stelsels die geselecteerd is op lichtkracht verschillende welbekende relaties tussen stervormingssnelheid en massa niet kan reproduceren. Dit is het geval voor een optische selectielimiet, maar in veel sterkere mate ook voor ultraviolette selectie. De beste manier is een selectie op massa.

Hoofdstuk 4 beschrijft de evolutie van de stervormingssnelheid van een op massa geselecteerde verzameling stelsels. Deze blijkt af te nemen in de tijd, op een manier die hetzelfde is voor stelsels van verschillende massa's. De stervormingssnelheid is daarbij voor zware stelsels altijd lager dan voor lichtere stelsels. Tenslotte hebben we bepaald hoeveel van de meest zware stelsels op $z = 1.8$, de limiet van onze waarnemingen, passieve evolutie ondergaan. We vonden een fractie van 30%. Bijna een derde van de meest massieve stelsels heeft op het moment dat het heelal nog geen 4 miljard jaar oud is, het grootste gedeelte van zijn sterren al gevormd. Deze waarde kan een sterke randvoorwaarde zijn voor voorspellingen van bijvoorbeeld semi-analytische modellen.

In **Hoofdstuk 5** vergelijken we de waargenomen stervormingsgeschiedenis in het heelal met voorspellingen van een semi-analytisch model. Net als bij de waarnemingen lijkt de groeisnelheid in modellen niet van massa af te hangen. Wel vinden we dat de groeisnelheid in waarnemingen veel hoger is dan in modellen. We onderzoeken verschillende observationele onzekerheden en geen van de mogelijkheden kan het verschil afdoende verklaren. We concluderen dat de modellen aangepast moeten worden om de sterke groei die in het heelal wordt waargenomen te kunnen reproduceren.

CURRICULUM VITAE

O P 3 mei 1980 kwam ik ter wereld, in Delft. Mijn jeugd bracht ik door in Naaldwijk, omgeven door kassen en boeken. Zo lang ik me kan herinneren ben ik gegrepen door literatuur. Naast het feit dat een goed boek kan ontroeren en aangrijpen, voorziet het vooral in een ruimere kijk op het leven. Daarmee roept het ook vragen op. Harry Mulisch schreef een boek over sterrenkunde en na mijn eindexamen aan het Westland College in Naaldwijk te hebben voltooid, vertrok ik naar Leiden. Geïntrigeerd en nieuwsgierig om meer te leren over de sterren.

Tijdens mijn studie heb ik onderzoek gedaan naar de interne structuur van nabije sterrenstelsels in de onderzoeksgroep van Prof. de Zeeuw. Hiertoe heb ik een week waargenomen op Kitt Peak in Arizona. In de tussentijd gaf ik bijles en huiswerkbegeleiding aan middelbare scholieren en maakte ik deel uit van de artistieke commissie van Imperium, een amateurtheatergroep in Leiden. In september 2005 slaagde ik voor het doctoraalexamen. Diezelfde maand mocht ik als promovenda aan de slag aan het onderzoek dat beschreven staat in dit proefschrift.

Er lag een prachtige set met observaties klaar, verkregen met de toen kersverse telescoop *Spitzer*. Hiermee bestudeerde ik onder begeleiding van Prof. dr. M. Franx en Prof. dr. P. G. van Dokkum de evolutie van sterrenstelsels. Zeer leerzaam waren de werkbezoeken aan dr. I. Labbé in Pasadena (Carnegie Observatories) en prof. dr. P. G. van Dokkum in New Haven (Yale). Op verschillende conferenties kreeg ik de gelegenheid mijn resultaten te presenteren en ontmoette ik collega's uit het veld.

Tijdens mijn tijd op de sterrewacht was ik ook lid van de opleidingscommissie en maakte ik met veel plezier deel uit van de publiekscontactencommissie waarin we enthousiaste kinderen en eigenwijze oude mannen te woord stonden.

Nu is het onderzoek afgerond, het boek geschreven. Ik ben sinds kort begonnen als beleidsmedewerker Astronomie bij de Nederlandse Organisatie voor Wetenschappelijk Onderzoek. Daar zal ik aan de andere, faciliterende kant van het onderzoek staan en ik hoop dat ik in die hoedanigheid nog veel kan bijdragen aan de sterrenkunde.

Nawoord

Een proefschrift schrijven is niet mogelijk zonder veel te vragen van je omgeving, al dan niet bewust. Voor die steun hier mijn dank.

Allereerst een speciale vermelding voor de dames van Roomburg en de artistieke Imperianen. Bedankt voor het geduldig aanhoren van de wellicht ietwat lange (doch immer enthousiast gebrachte) verhalen over het heelal en al zijn facetten.

En dan de Sterrewacht. Een hele prettige werkplek, niet in het minst door de verzameling bijzondere personen. De altijd parate "computer guys", Aart, David, Erik, en Tycho, bedankt. Ik heb wat vreemde trucs uitgehaald, maar jullie wisten er altijd snel raad mee. De dames van het secretariaat, Anita, Liesbeth, bedankt voor jullie hulp waar dat nodig was, en in het bijzonder Kirsten en Jeanne, jullie waren een bron van sappige, maffe en ontroerende verhalen en wisten bovendien alle ins-and-outs van de Sterrewacht. De gezamenlijke lunches mis ik nu al.
Mijn groepsgenoten in en buiten de sterrewacht stonden altijd klaar om te helpen, daarbij werd een biertje af en toe gelukkig niet geschuwd. Arjen, Danilo, Gabe, Ivo, Kate, Mariska, Natascha, Ned, Rik, Ryan, Stijn, en Sune, een lange lijst van dierbare mensen. Bedankt.

Olja, jou noem ik ook. Je bent een van de liefste personen die ik ken en je weet een opzienbarende hoeveelheid feitjes. Geloof in jezelf, je bent fantastisch. Ryan, you're a remarkable person and you possess a calm that I'm (sometimes) a bit jealous of. Willem, op de valreep kwam je mijn kamertje binnenwandelen en dat was goed. Ik hoop dat we onze inzichtelijke en inspirerende gesprekken snel eens voort kunnen zetten. Mariska, ik ken niemand zoals jij. Ik ben ontzettend blij dat je mijn paranimf bent. Dat geldt ook voor Pedro, bijzondere vriend en creatief bolwerk, ik hoop dat we elkaar nog vaak gaan zien.

Kaar, ik ken je al zo lang en kan altijd bij je terecht. Zo leuk dat we in hetzelfde promotieschuitje zitten.

Ruud en Milou, bedankt voor jullie steun, niet-aflatende belangstelling, en het prachtige omslagontwerp. Pap, bedankt voor je nuchterheid, Martijn voor je intensieve en onvoorwaardelijke hulp met de omslag, Peter-Paul, voor het overnemen van het stokje. Jij bent nu de wetenschapper van de familie, maak het maar waar. Lieve Loes, je bent voor mij de perfecte zus, mijn steun in stress en wekelijks rustpunt, bedankt. Mama bedankt voor je vertrouwen en trots.

Bas, bedankt. Zonder jou was dit geen boek en was ik niet ik.